ABSTRACT

Title of Document:	MOISTURE FLUX ESTIMATES DERIVED FROM EOS AQUA DATA IN THE ARCTIC Linette Nicole Boisvert, Doctor of Philosophy, 2013
Dissertation directed by:	Prof. James Carton (the academic advisor), Department of Atmospheric and Oceanic Science, and Dr. Thorsten Markus, Head, Cryospheric Sciences Branch, NASA

The Arctic sea ice acts as a barrier between the ocean and atmosphere inhibiting the exchange of heat, momentum, and moisture. Recently, the ice pack has been decreasing in area and concentration. This diminished sea ice coverage could potentially allow for larger moisture fluxes that affect surface energy budgets, the occurrence of clouds, and the near-surface humidity and temperature. Currently, reanalyses are known to produce large errors and biases in the Arctic, warranting improved moisture flux algorithms and input data. Using the Monin-Obukhov similarity theory, with adjustments made to better suit the conditions of the Arctic, and observations from NASA's EOS Aqua satellite, specifically the AIRS and AMSR-E instruments, the daily moisture flux is calculated from 2003-2011. The moisture flux is studied for a series of North Water

polynya events between 2003-2009 to test the accuracy of the Aqua products and our algorithm. Using in situ data we validated moisture flux results, finding an error of 20.3%, improving the moisture flux accuracy compared to other climate models. The moisture flux for the entire Arctic was studied to look for inter-annual variations and was compared to changes in the sea ice. Instead of an expected increase in the moisture flux due to a declining sea ice pack, there has been a 15% decrease. On a regional scale and based on their average moisture flux, the Chukchi/Beaufort Seas, Laptev/E. Siberian Seas, Canadian Archipelago and Central Arctic are increasing, between 2.1 and 4.8 %/yr. Increases are due to the changes in the ice concentration, which allows for the surface temperatures to increase substantially in the fall and winter months when the amount of moisture exchanged is highest. The Kara/Barents Seas, E. Greenland Sea and Baffin Bay are decreasing, between 0.53 and 9.2 %/yr. These regions have areas of open water year round, and their exchanges of moisture are due mostly to smaller differences in surface and 2 m specific humidities. The contribution of the sea ice zone to the total moisture flux (from the open ocean and sea ice zone) has increased by 3.6% because the amount of open water within the sea ice zone has increased by 4.3%.

Moisture Flux Estimates Derived from EOS Aqua Data in the Arctic

Linette Nicole Boisvert

Dissertation submitted in to the Faculty of the Graduate School of the

University of Maryland, College Park in partial fulfillment

of the requirements for the degree of

Doctor of Philosophy

2013

Advisory Committee:

Professor James Carton, Chair

Dr. Thorsten Markus, Advisor

Dr. Sinead Farrell

Professor Rachel Pinker

Professor Konstantin Vinnikov

Professor Theodore Einstein, Dean's Representative

Preface

Dr. Charles Caramello

Dean of the Graduate School 2123 Lee Building

College Park, Maryland 20742

Dear Dr. Caramello,

Ms. Linette Boisvert's dissertation is presented to the dissertation committee at the Department of Atmospheric and Oceanic Science at the University of Maryland, College Park, and contains the following co-authored work:

Chapter 5 was published as *Boisvert, L. N., T. Markus, C. L. Parkinson, and T. Vihma (2012), Moisture fluxes derived from EOS Aqua satellite data for the North Water polynya over 2003-2009, J. Geophys. Res., 117, D06119, doi:10.1029/2001JD016949*.

Chapter 6 was published as *Boisvert, L. N., T. Markus, and T. Vihma (2013), Moisture flux changes and trends for the entire Arctic in 2003-2011 derived from EOS Aqua data, J. Geophys. Res., accepted.*

Inclusion of this work has the approval of Ms. Boisvert's dissertation advisor Dr. Thorsten Markus and her co-advisor and AOSC program chair Prof. James Carton.

Ms. Boisvert's examining committee has determined that the student made a substantial contribution to the work listed above.

Cordially,

Thorsten Markus

Research Advisor and Cryospheric Sciences Lab Chief

NASA Goddard Space Flight Center (GSFC)

8800 Greenbelt Road, Greenbelt, MD 20771

tel: 301-614-5882 fax: 301-614-5644

My thesis is dedicated to my father, Ron, my mother, Rita, and my fiancé, Chris.

Acknowledgments

My journey throughout graduate school has had its fair share of up and downs and has been a life changing and unforgettable experience. I believe that everything happens for a reason and that hard work and the support of many people have helped, inspired and encouraged me throughout my graduate studies. I can't thank everyone individually here, but I do appreciate all that they have done.

I would like to thank my advisor, Thorsten Markus, for seeing the potential in me and taking me under his wing in the fall of my second year in graduate school. He was always available for help, guidance and support whenever it was needed. He has taught me about the Arctic, which has always been my passion, and has been selfless in his efforts in helping me complete my thesis. Without him, I would not be where I am in my scientific career today or studying the Arctic and I immensely thank him for all that he has done.

I would also like to thank my academic advisor, Jim Carton, for his continued enthusiasm and support throughout my graduate career. His discussions of my research have helped me improve my presentation skills. Thanks also to my other committee members: Rachel Pinker, Konstantin Vinnikov, and Sinead Farrell for sacrificing their time in reading over and giving me feedback to improve my thesis. Their time serving on my committee is really appreciated.

I have collaborated with Timo Vihma on my two published academic papers thus far and I would like to thank him for all of his help in teaching me of the nuisances of the

moisture flux in the Arctic. His tireless efforts on providing feedback in my studies have strengthened this thesis. I hope that we can continue to collaborate in the future.

My fellow students, coworkers, and friends have all contributed in their own unique way to my experience throughout graduate school. I would like to thank Nathan Kurtz, my officemate, mentor and 'PhD big brother', for always willing to help me out with an IDL problem and to provide stress relief when discussing the fears and doubts that sometimes come with being a graduate student. I would also like to thank Claire Parkinson for her tireless efforts in editing my papers and posters for conferences. She has been an inspiration to me. I would also like to thank Jeff Miller, Alvaro Ivanoff and Nicolo DiGirolamo for their help teaching me how to use IDL and the satellite data that I used in my thesis and to be there to always answer a coding question.

I would like to thank my father and mother for shaping me into the person that I have become and always supporting me throughout my life. They have always stressed the importance and value of education. I have always idolized my father and wanted to pursue a PhD since I was 5, because my father has one, although the subject matter has changed. My father has always had time to help me with homework growing up and I really do appreciate that. My mother has always fueled my education via her amazing desserts.

Finally, I would like to thank my fiancé, Chris McPartland, for all of his continued love and support while I have been in graduate school. He has compelled me to complete my thesis so that we can begin the next chapter of our lives together.

Table of Contents

List of Tables

List of Figures

and Ice Data Center website (http://nsidc.org/asina/2010/100410.html). Image on right is the mean summer SST anomalies for the Chukchi and West Beaufort Seas. Shown are the 50 km binned in situ input anomalies (grey dots), the means of these anomalies (green dots), 95% confidence range of these means, and number of 50 km bins with in situ data in each decade (along bottom axis). Also shown is the summer mean satellite derived SSTs (yellow dots) adjusted by the mean difference over the data record (i.e., bias) of the in situ summer means minus the satellite means. Smoothed regional means (blue curves) are computed from the average in each summer of the green and yellow dots by an application of a 3-year running mean filter followed by 2 passes of a 5-year running mean filter. From *Steele et al.,* [2008].

Figure 6. Melt season length for the entire Arctic, Chukchi/Beaufort Seas, and Laptev/East Siberian Seas. The solid lines indicate the length of continuous melt (early freeze onset (EFO) – melt onset (MO)), and dashed lines indicate the first day of melt until the last day of melt (freeze onset (FO) – early melt onset (EMO)). The numbers show the trends in days per decade. Trends with a plus sign are significant at the 95% confidence level, and trends with two plus signs are significant at the 99% confidence level. From *Markus et al.,* [2009].

Figure 7. (top) Time series of Arctic sea ice extent anomaly with high and low ice years shown, and (bottom) the accompanying time series of autumn low cloud cover anomaly showing cloud anomalies during high and low ice years. From *Eastman and Warren,* [2010].

Figure 8. September clouds from 2006-2008. MODIS cloud fraction with 15 September sea ice extent contour. From *Kay and Gettelman,* [2009].

Figure 9. Images show comparisons of NCEP/NCAR and ECMWF Reanalysis upper-level winds to measurements by rawinsondes during the CEAREX and LeadEx Arctic field programs. Layers 1-5 are bounded by the following pressure levels: 300, 400, 500, 700, 850, and 1000 hPa. Image on the left is the mean wind magnitude from rawinsondes and bias in the NCEP/NCAR speed. Image on the right is the mean magnitude from rawinsondes and bias in the ECMWF speed. From *Francis* [2002].

Figure 10. a) Arctic and annual mean 700 hPa temperature bias in each reanalysis relative to radiosondes. The radiosonde data are averages from nine Arctic stations. The reanalysis temperature fields were first subsampled at the station locations and then average over all subsampled grid boxes. For each reanalysis, the mean bias was removed to highligh the time varying component of the bias. b) Decadal Arctic and annual mean temperature trends from radiosondes and each reanalysis. Trends are centered on the indicated year (e.g., the trend at 1995 is based on data from 1990-2000). The gray band denotes the 95% confidence intervals of the trends. From *Screen and Simmonds,* [2010].
Figure 11. From 29 single profiles calculated: (a) average temperature, (b) RMSE (root mean square error) of temperature, (c) average specific humidity, (d) RMSE of specific humidity, (e) average relative humidity, (f) RMSE of relative humidity, (g) average wind speed, (h) RMSE of wind speed. From *Jakobson et al.* [2012].

Figure 12. Arctic September sea ice extent is decreasing much faster than projected by computer models. The dotted line represents the average rate of melting indicated by the computer models, with the blue area indicating the spread of the models. The red line shows the actual rate of ice loss based on observations. Illustration by Steve Deyo, UCAR, based on research by NSIDC and NCAR (http://www.ucar.edu/news/releases/2007/seaice.shtml).

Figure 13. Average decadal SST trends for June, July, August, September and October separately and JJASO, 1982-2009. All trends at significant at the 95th percentile.

Figure 14. Decadal freeze onset, SSTs and ice concentration trends for 1982-2009 (top), 1982-1999 (middle) and 2000-2009 (bottom). All trends at significant at the 95th percentile.

Figure 15. Entire Arctic 1982-1999 and 2000-2009 weekly trends in a.) ice concentration, b.) sea surface temperature and c.) Average ice concentration and SSTs for 1982-1999 and 2000-2009.

Figure 16. 1982-1999 and 2000-2009 weekly trends in ice concentration, SST and average ice concentration for the Chukchi/Beaufort Seas (a,b,c), Laptev/E. Siberian Seas (d,e,f), Kara/Barents Seas (g,h,i) and the E. Greenland Sea (j,k,l).

Figure 17. Values of zT/z0 averaged in Re bins for the Munro, Kondo and Yamazawa, and Ishikawa and Kodama datasets. The error bars are one std dev; the number beside each data marker gives the number of individual values used to create the average. The line is the *Andreas* (1987) model. (From *Andreas*, 2002).

Figure 18. Validation tests of the *Launiainen and Vihma* [1990] model (Figures from *Launiainen and Vihma* [1990]).

a) Calculated sensible heat flux ($H/\rho C_p$) verses the one measured using the eddy correlation method (crosses from *Schmitt et at.* [1979] and circles from *Fujitani* [1981]
b) Calculated water vapor flux (E/ρ) verses the measured one (same as above)

Figure 19. Diagram of sensible heat (open ocean) and latent heat (coastal) polynya formation. Image from *Ocean Circulation, 2nd Edition* by Open University, Butterworth-Heinemann Publishers, page 219.

Figure 20. (top) A false color RGB image derived from 1-km resolution NOAA-18 AVHRR data shows a long narrow cloud plume streaming northwestward from the Bennett Island polynya on March 12, 2008. (bottom) A 250m resolution Terra MODIS visible image shows a closer view of the Bennett Island polynya and its cloud plume on March 12, 2008. Images from Cooperative Institute for Meteorological Satellite Studies website (http://cimss.ssec.wisc.edu/goes/blog/archives/622).

Figure 32. The 2m specific humidity (kg kg^{-1}) from AIRS (black line) and Tara drifting station (red line) from April 1 until September 20, 2007.

Figure 33. The total moisture flux for the entire Arctic for January, 2003 until September, 2011. The blue line is the moisture flux from the solid sea ice pack (15-100% ice concentration), the red line is the moisture flux from the ocean (0-15% ice concentration) and the black line is the moisture from both the sea ice pack and the ocean. Grey vertical lines separate the different years.

Figure 34. (Top) The 2m specific humidity and surface specific humidity (kg/kg) differences for the month of October for each year 2003-2010 for the entire Arctic. (Bottom) The 2m air temperature and surface temperature (K) differences for the month October for each year 2003-2010 for the entire Arctic. The grey is either the land or no data in both images.

Figure 35. The difference between the yearly moisture flux and the average moisture flux from 2003-2010. Positive anomalies are shown in pinks, negative in blues. The grey is either the land or no data.

Figure 36. Top: Average temperature differences for the surface and 2m, monthly from January 2003 until September 2011. Bottom: Average specific humidity differences for the surface and 2, monthly from January 2003 until September 2011. The black line is the

average difference for regions 4,5, & 6 in Figure 1. The red line is the average difference for regions 7, 8, 9, & 10 in Figure 1. The grey lines differentiate between years.

Figure 37. Left: Specific humidity (kg/kg) differences between the surface and 2m for January for 2003-2011. Right: Moisture flux anomalies (yearly minus the average moisture flux) from 2003-2011. Pinks are positive anomalies and blues are negative anomalies. Grey is either land or no data.

Figure 38. Average monthly SST anomalies for the East Greenland Sea from January, 2003 until September, 2011. Black line is the SST anomaly from AMSR-E SST product. Grey lines delineate between years.

Figure 39. a) ERA-Interim January 2010 evaporation rate (mm/day) anomaly for the northern hemisphere, b) ERA-Interim October 2010 evaporation rate (mm/day) anomaly for the northern hemisphere, c) ERA-Interim January-October 2010 evaporation rate (mm/day) for the northern hemisphere, d) ERA-Interim January 2010 1000mb specific humidity (g/g) anomaly for the northern hemisphere, e) ERA-Interim October 2010 1000mb specific humidity (g/g) anomaly for the northern hemisphere, f) ERA-Interim January-December 2010 1000mb specific humidity (g/g) anomaly for the northern hemisphere. All of these images were produced using WRIT at https://reanalyses.org/atmosphere/web-based-reanalysis-intercomparison-tools-writ.

2003-2011 average corresponds either to the average light, moderate or heavy ice accretion, not the total ice accretion.

Chapter 1: Introduction

1.1 General Introduction

Polar regions are experiencing particularly large changes compared to other regions on Earth due to global warming [*ACIA,* 2005]; and variations in the moisture flux from the ocean to the atmosphere may serve as a good indicator of climate changes, because the moisture flux is strongly affected by openings in the sea ice cover, polynyas and leads, which interact with both the atmosphere and ocean.

The Arctic climate is defined by little or no sunlight in the winter months and almost 24 hours of sunlight in the summer months [*ACIA*, 2005]. The largest component of the Arctic climate is the cryopshere, which is frozen water. The Arctic Ocean and it's peripheral seas are covered with frozen seawater known as sea ice year round. The sea ice area follows a seasonal cycle with the largest extent occurring in March and the smallest extent occurring in September. The 14 million km^2 Arctic Ocean and seas are nearly isolated. They are surrounded by Eurasian and North American landmasses, except for the in Bering Strait and in the North Atlantic regions [*ACIA,* 2005]. The Arctic is separated by region based (Figure 1).

Figure 1. Map of the Arctic Ocean and surrounding landmasses. The peripheral seas are in blue font and major cities and countries are in black font. Figure from http://www.lib.utexas.edu/maps/islands_oceans_poles/arctic_ref802647_1999.jpg.

In recent decades, the Arctic sea ice pack has undergone substantial changes. The ice pack has decreased in extent, at a rate of 4%/decade [*Parkinson and Cavalieri, 2008*] (Figure 2 & 3), thickness, declining 1.75 meters since 1980 (Figure 3) [*Kwok and Rothrock*, 2009] and concentration. The September minimum sea ice extent is now decreasing at a rate of 14%/decade.

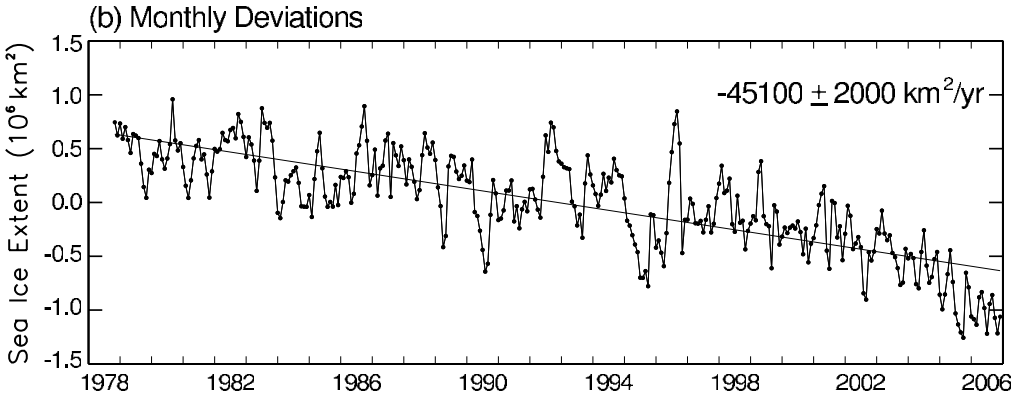

Figure 2. Monthly deviations for the sea ice extents calculated by taking the monthly value for the individual month and subtracting the average value for that month over the 28.2 year period, plus the line of linear least squares fit through the monthly deviations, along with its slope and estimated standard deviation. From *Parkinson and Cavalieri,* [2009].

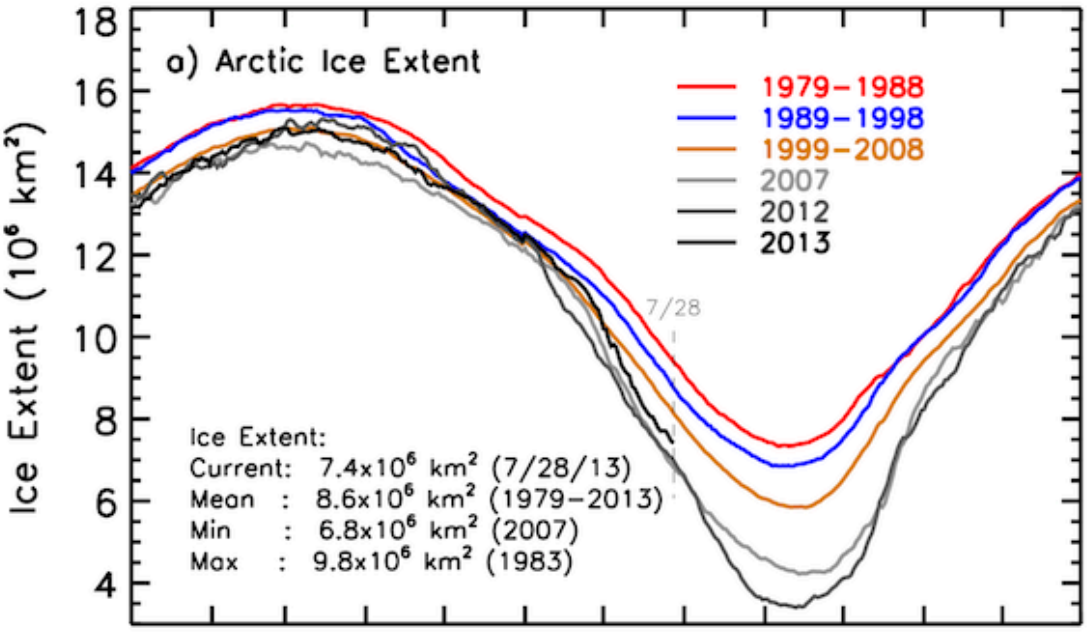

Jan Feb Mar Apr May Jun Jul Aug Sep Oct Nov Dec

Figure 3. Arctic sea ice extent in millions of square kilometers for years 2007, 2012 and 2013. The average sea ice extent for 1979-1988, 1989-1998, and 1999-2008 are also shown. Image from the Cryospheric Sciences Branch at NASA GSFC (www.cryosphere.gsfc.nasa.gov).

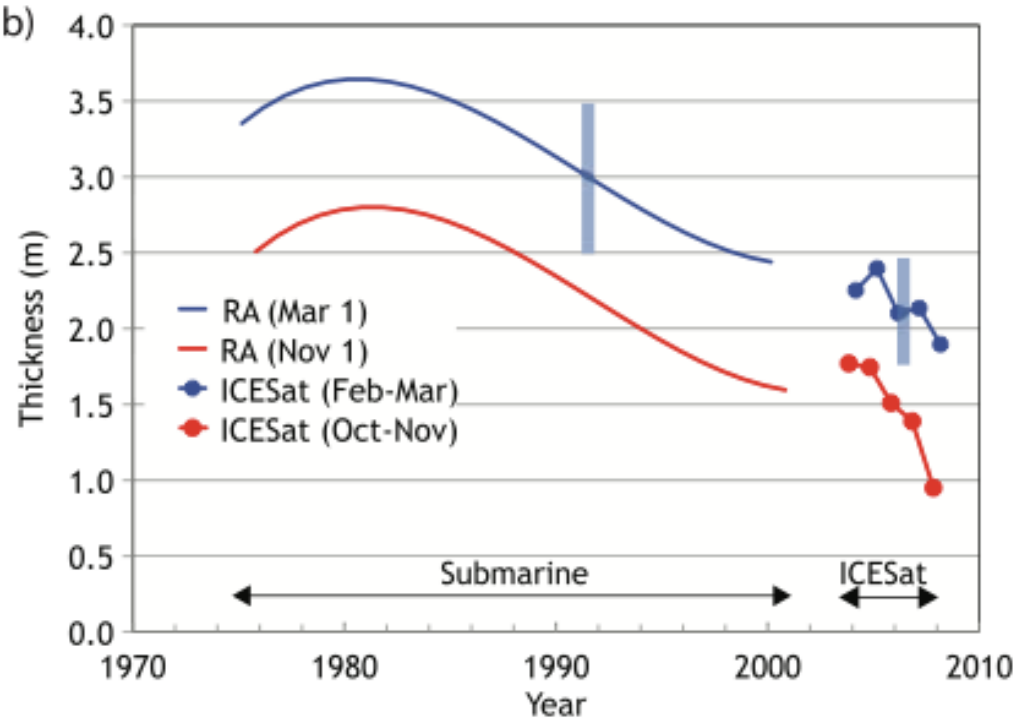

Figure 4. Interannual changes in winter and summer ice thickness from RPW08 and K09 submarine data centered on the ICESat Campaigns. Blue error bars show residuals in the regression and quality of ICESat data. From *Kwok and Rothrock,* [2009].

The ice pack has shifted from a predominantly multi-year ice pack, ice that survives the summer melt, to a predominantly first-year ice pack, one that melts in the summer (Figure 5) [*Nghiem et al., 2007*]. The Arctic Ocean has also shown warming since 2000, with 2007 having 5°C anomalies in sea surface temperatures (Figure 6) [*Steele et al.,* 2008]. Such large increases in SSTs during 2007 are believed to be caused by the

extreme minimum sea ice extent and decreased cloud cover that occurred in the summer of 2007 [*Steele et al.,* 2010, *Perovich et al*., 2008, *Kay et al.,* 2008].

The melt season length of the Arctic sea ice has increased, meaning that the ice begins melting earlier in the spring and begins freezing up later in the fall (Figure 7). Melt season is increasing for the entire Arctic by 6.4 days/decade, with some areas increasing by as much as 10 days/decade [*Markus et al., 2009*].

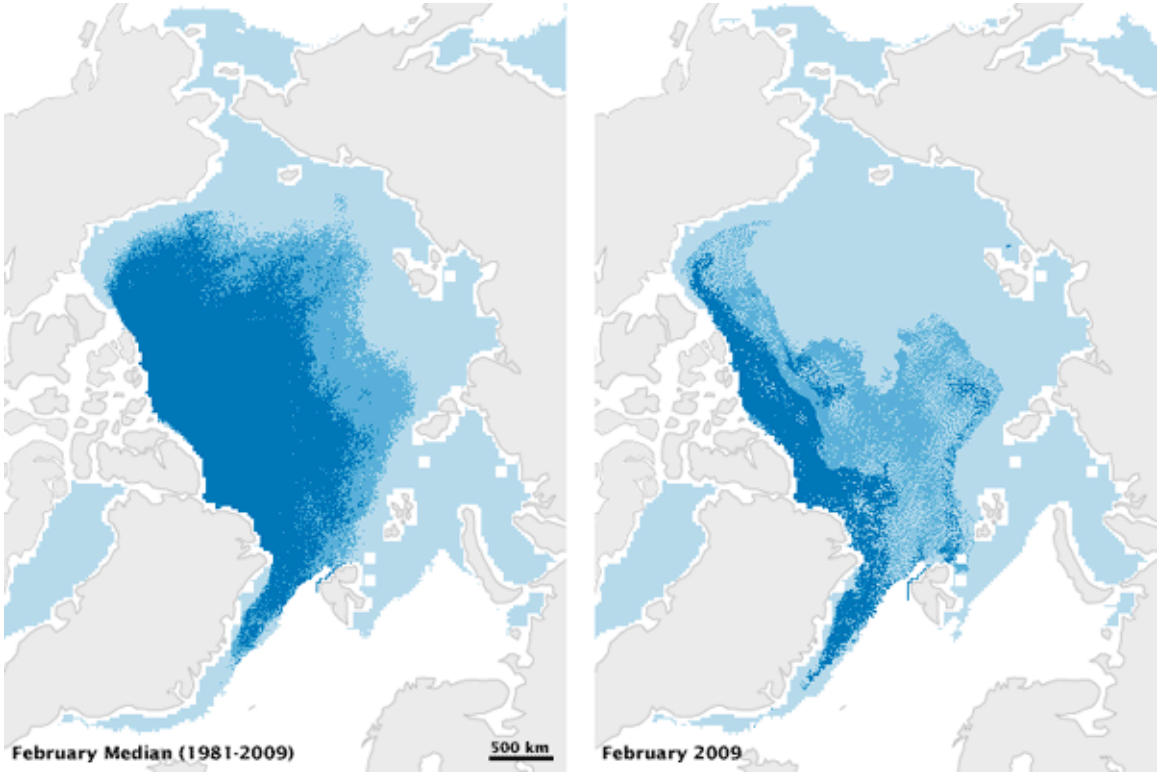

Figure 5. Arctic sea ice types and coverage. Image on left shows the median first year (light blue), one year ice (medium blue) and multi year ice (dark blue) for February 1981-2009. Image on right shows the first year, one year and multi year ice for February 2009. Image from National Snow and Ice Data Center (http://nsidc.org/arcticseaicenews/).

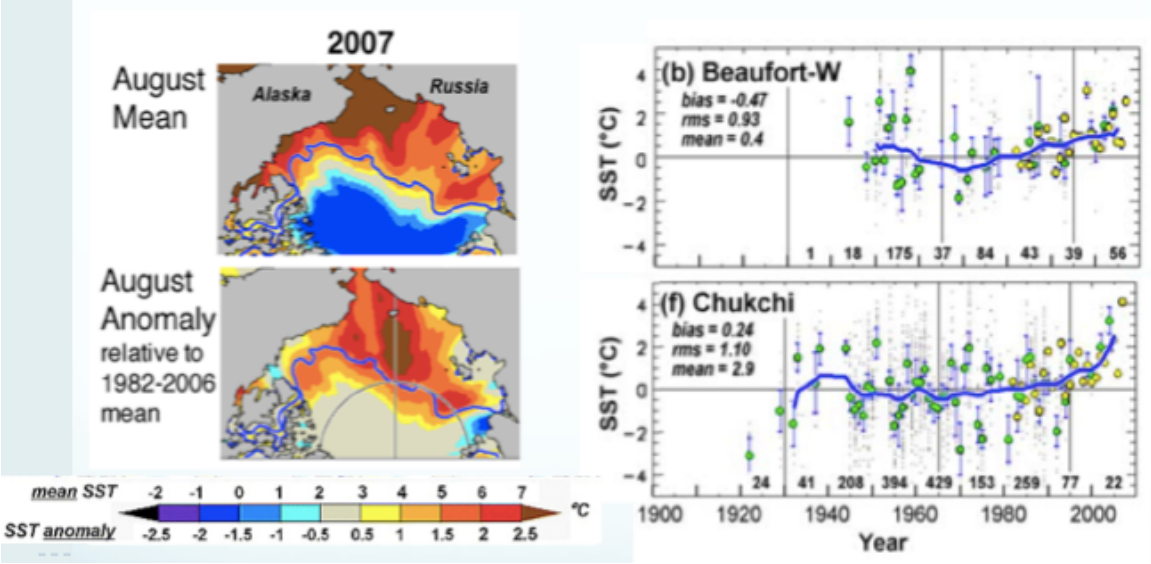

Figure 6. Image on left is the August 2007 mean SST for the Arctic (top) and the August Anomaly for 2007 relative to the August mean 1982-2006 (bottom). From National Snow and Ice Data Center website (http://nsidc.org/asina/2010/100410.html). Image on right is the mean summer SST anomalies for the Chukchi and West Beaufort Seas. Shown are the 50 km binned in situ input anomalies (grey dots), the means of these anomalies (green dots), 95% confidence range of these means, and number of 50 km bins with in situ data in each decade (along bottom axis). Also shown is the summer mean satellite derived SSTs (yellow dots) adjusted by the mean difference over the data record (i.e., bias) of the in situ summer means minus the satellite means. Smoothed regional means (blue curves) are computed from the average in each summer of the green and yellow dots by an application of a 3-year running mean filter followed by 2 passes of a 5-year running mean filter. From *Steele et al.,* [2008].

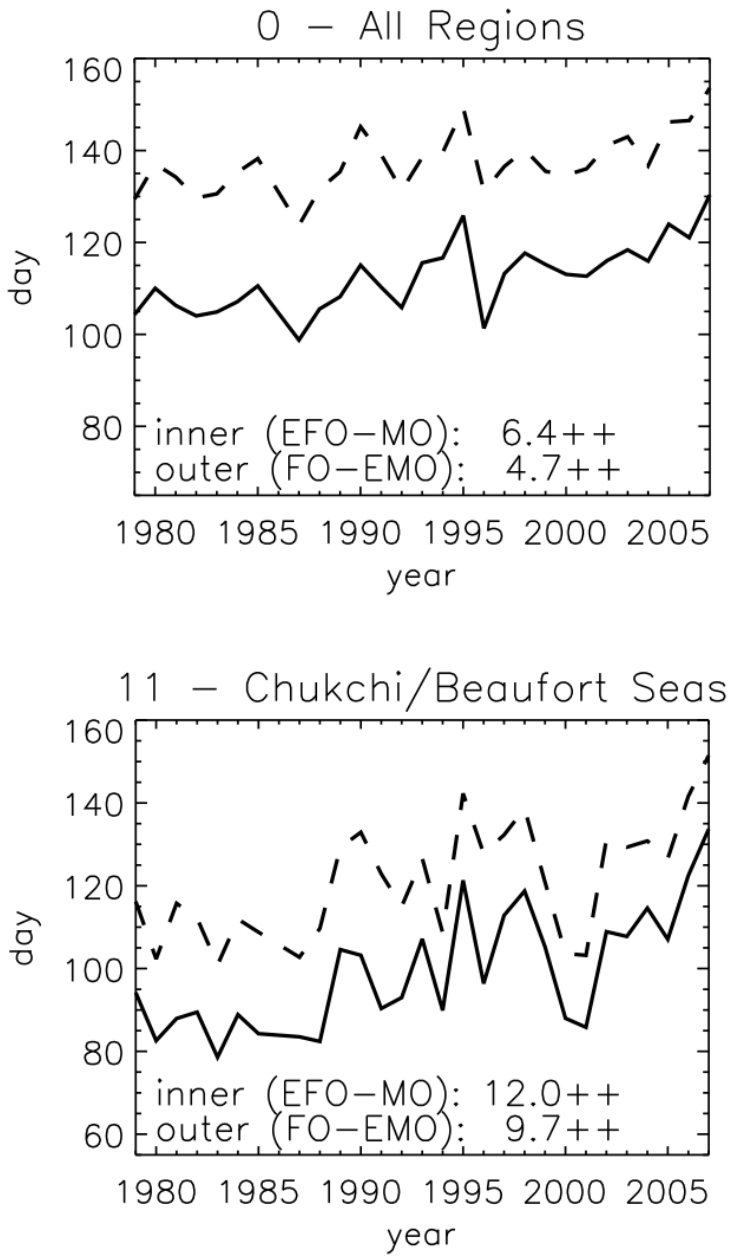

Figure 7. Melt season length for the entire Arctic and the Chukchi/Beaufort Seas. The solid lines indicate the length of continuous melt (early freeze onset (EFO) – melt onset (MO)), and dashed lines indicate the first day of melt until the last day of melt (freeze onset (FO) – early melt onset (EMO)). The numbers show the trends in days per decade. Trends with a plus sign are significant at the 95% confidence level, and trends with two plus signs are significant at the 99% confidence level. From *Markus et al.,* [2009].

All of these factors work together to contribute to the decline of the sea ice pack. This weakened sea ice pack is not as effective at insulating the ocean and atmosphere as this ice

pack in past years would be, allowing for more heat and moisture to be exchanged between the two. The increase of moisture to the atmosphere can alter the surface radiation budget by increasing the amount of clouds, which reflect the incoming solar radiation and also hinder the escape of the upwelling longwave radiation from the surface. Water vapor itself is a strong greenhouse gas and could also influence Arctic warming. *Dessler et al.* [2008] found that water vapor and its subsequent warming could double the warming caused by increases in CO_2.

This could create a positive feedback loop where larger areas of open water increase the moisture flux into the atmosphere, increase the amount of clouds, which add heat to the system, and cause the sea ice to melt, continuing the cycle. Increased cloud cover also increases reflection of solar radiation, and hence some negative feedback processes during the summer months could be operating as well.

1.2 Dissertation Outline

Chapter 2: Arctic Sea Ice and Observations

The sea ice-ocean-atmosphere climate system of the Arctic is described. Gives a broad overview of the current state of Arctic sea ice observations, reanalysis data, climate models and satellite and their limitations.

Chapter 3: Arctic sea surface temperatures 1982-2009

SST trends are compared between the 1982-1999 and 2000-2009 time periods in the entire Arctic and for multiple regions. Delays in the freeze onset are also estimated based on the SSTs.

Chapter 4: Arctic Ocean moisture flux

Introduces the moisture flux equation and provides a brief overview of what the moisture flux is and how it exchanges moisture between the surface and the lower atmosphere in the Arctic. This chapter describes in detail the data platforms and types used in the moisture flux studies done for the North Water polynya and the entire Arctic. Describes the Monin-Obukov Similarity Theory used to calculate the moisture flux and also our updated Monin-Obukhov Similarity Theory to improve the moisture flux estimates in the Arctic.

Chapter 5: Case Study: Moisture flux from the North Water Polynya

This chapter goes into great detail on polynyas and their many affects on the Arctic climate system. The North Water polynya is also discussed. Error estimation is explained and potential errors within the datasets are described. AIRS air temperature is compared the NPEO buoy temperatures for accuracy. Comparisons of the data sets are done with ECMWF ERA-Interim data as well as with other similar studies. Moisture flux results are presented in this chapter are from the North Water polynya study for the years 2003-2009. Different polynya events from each year are compared.

Chapter 6: Moisture flux for the entire Arctic

AIRS 1000 hPa relative humidity is validated with Tara drifting station observations for validation of the moisture flux for the Arctic. Moisture flux results are presented in this chapter are from the entire Arctic for the years 2003-2011. Monthly trends are described and moisture flux and changes in ice concentration are also discussed.

Chapter 7: Practical Application: Prediction of super structural icing for shipping

This chapter addresses a practical application for a few geophysical parameters of AIRS. The ice accretion method and equations are explained as well as changes in the potential for ice accretion with the changing Arctic climate system.

Chapter 8: Conclusions

Summaries of the North Water polynya, the entire Arctic and the Arctic sea surface temperature studies are presented here.

Chapter 9: Future Work

An explanation of future work involving the validation of AIRS data in the Arctic and future uses of the moisture flux are presented in this chapter.

Chapter 2: Arctic Sea Ice and Observations

2.1 The Arctic climate system

The Arctic climate system is a complex interaction between the Arctic Ocean, the atmosphere, and the sea ice. Studying these interactions and learning how they affect one another is crucial for accurately representing the Arctic system in climate models. Recently, the Arctic has experienced greater-than-global air and surface temperature warming in response to increased greenhouse gases, which is known as Arctic amplification [*Kay et al.,* 2012]. Being able to understand the Arctic climate system and how it reacts to global warming can give us a clearer picture of how other regions around the world might react to these adverse reactions to global warming in the future. Climate changes in the Arctic affect other regions around the world as well [*Alley,* 1985].

One interaction linking the Arctic sea ice and atmosphere is how changes in sea level pressure and wind patterns affect the sea ice. One of these patterns is the Arctic Oscillation (AO). The AO, in either its positive or negative phase, is used to classify opposing sea level pressure and zonal wind patterns in the Arctic, and thus sea ice motion [*Thompson and Wallace*, 1998]. In the positive phase, sea level pressure is lower over the Arctic and winds push sea ice away from the coasts of the Laptev/East Siberian Seas, and there is larger transport of sea ice out through the Fram Strait, creating thinner ice in the central Arctic [*Rigor et al.,* 2002]. Conversely, in its negative phase, pressure is high in the Arctic and temperatures are often warmer than normal. The AO can affect the ice thickness, concentration, the ice motion and the heat budget [*Rigor et al.*, 2002]. The AO

was strongly positive in winter in the early 1990's, it has been low and variable most recently. Another pattern is the Arctic Dipole (AD), which classifies changes in meridonal wind patterns in the Arctic. Its' positive phase is classified as having lower sea level pressure on the North American side of the Arctic [*Overland and Wang,* 2009]. The AD positive phase has become more dominant since 1997 and has contributed to smaller sea ice extents in the summer. It has also contributed to changes in large-scale atmospheric circulation patterns, which are supplied by heat stored in the ocean in autumn [*Overland and Wang,* 2009].

The Arctic sea ice also plays a crucial role in maintaining the global thermohaline circulation, which transports heat throughout the world's oceans. When sea ice forms, only fresh water freezes, leaving behind brine in the surface layer of the Arctic Ocean, increasing the salinity and also the density of the water [*Agaard et al.*, 1985]. This cold, dense water sinks to the ocean floor, leading to deepwater formation. This water is replaced by surface waters from lower latitudes, driving the thermohaline circulation. When sea ice melts, it freshens the surface layer, making it less dense, and inhibits sinking. Thus, large amounts of sea ice melting could cause the thermohaline circulation to slow down or even stop. Changing this ocean circulation will change the climate on a global level. There is still much uncertainty of how the sea ice could affect the thermohaline in the future with global warming [*Stouffer et al.*, 2006].

The most prominent positive feedback loop that encompasses the interactions between the Arctic sea ice, ocean and atmosphere is the ice-albedo feedback. The sea ice has an albedo of 0.9 compared to that of the ocean having an albedo of 0.06. Thus the sea ice absorbs less energy (about 10%) from the atmosphere and reflects most of it, compared

to the ocean, which absorbs (about 94%) most of the energy. During the summer months where there has been significant ice loss in recent decades, the amount of energy that the system absorbs is much greater. Thus the Arctic Ocean warms, causing more melting, more absorption and even more melting of the sea ice. This excess energy absorbed into the system also affects the surface energy balance, which can change the energy budget in the Arctic [*Comiso*, 2010].

Another complex interaction dealing with the ice-albedo feedback is between the downwelling shortwave solar radiation and the upwelling longwave radiation from the surface in the Arctic. This is further complicated by the presence of clouds, which reduce both incoming solar radiation and longwave radiation from leaving the surface.

Walsh and Chapman [1998], *Intrieri et al.* [2002] and *Curry and Ebert* [1992] found that Arctic clouds have a net warming effect for the entire year except for a short period in the summer, meaning that more clouds will actually cause the Arctic to warm further and accelerate the melting of the sea ice. Since water vapor is a greenhouse gas it is also an excellent absorber of longwave radiation; hence having a larger flux of moisture and thus a moister atmosphere could heat the atmosphere even more, further enhancing the ice melt.

Recent studies by *Palm et al.* [2010], *Eastman and Warren* [2010], and *Kay and Gettelman* [2009] have looked into the changing sea ice extent and thickness and how this has affected the amount of clouds over the Arctic (Figure 8 and 9). They found that there were increases in clouds in all months with the largest increases in the fall when there were large decreases in sea ice extent. This is when large differences in temperatures between the ocean surface and atmosphere enhanced the turbulent fluxes, which help to

produce low-level clouds [*Klein et al.,* 2009]. Since the heat capacity of water is much larger than the air, when the air temperatures begin to decrease in the fall the ocean temperatures take much longer to cool down. This along with warmer sea surface temperatures and larger open ocean areas, might have caused this increase in clouds in the fall. Low-level clouds, which increase the downwelling longwave radiation the most, saw the largest increase in the fall and this in turn keeps the lower atmosphere warmer in the winter months. Warmer winters do not allow for the ice pack to refreeze as much as it would with colder temperatures and thus creates a weaker ice pack in the following spring.

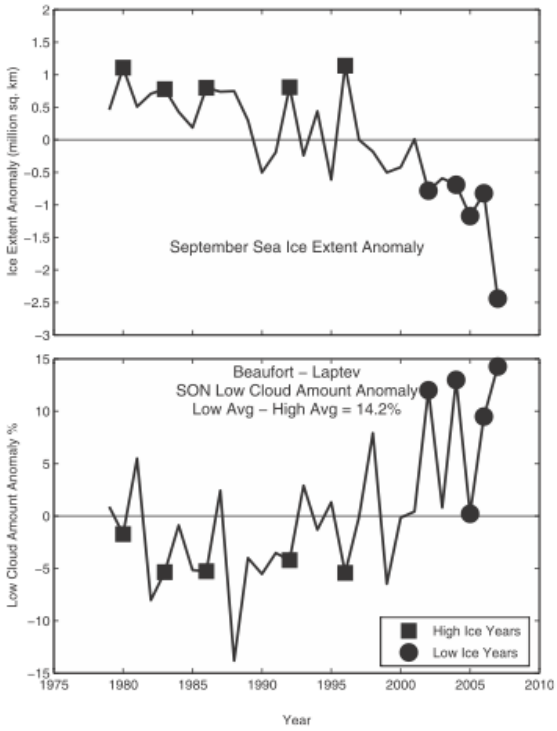

Figure 8. (top) Time series of Arctic sea ice extent anomaly (based on the average September sea ice extent 1978-2008) with high and low ice years shown, and (bottom) the accompanying time series of autumn low cloud cover anomaly showing cloud anomalies during high and low ice years. From *Eastman and Warren,* [2010].

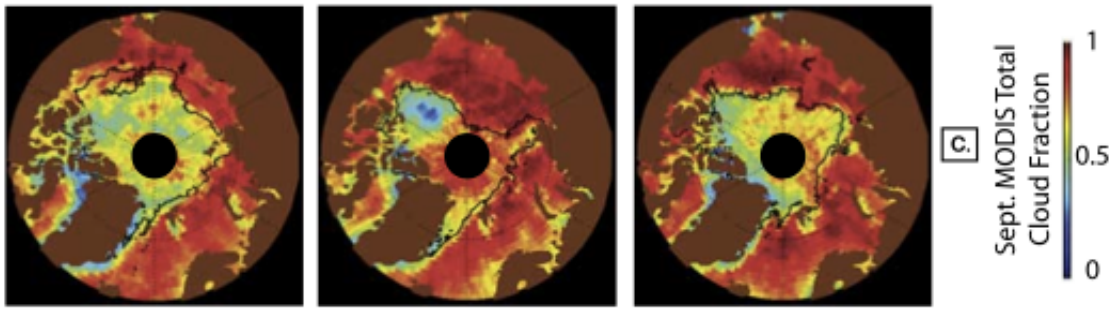

Figure 9. September clouds from 2006-2008. MODIS cloud fraction with 15 September sea ice extent contour. From *Kay and Gettelman,* [2009].

2.2 Data Types

In the Arctic, where in situ observations are sparse and reanalysis data can often be biased, satellite data provide a wealth of observations on extensive spatial and temporal scales. Yet there have been few studies done which have used this data to study surface moisture fluxes from the ice pack. Improving the parameters used to calculate the moisture flux and thus the flux estimates will help to strengthen the accuracy of climate models. They can also be used to improve the interpretation of the Arctic's exchanges of moisture from the surface and also in the generation of boundary layer clouds. Producing large-scale estimates of the moisture flux with satellite data would be valuable for assessing both the current state of the Arctic and the impact of the changing ice pack on the moisture fluxes.

There are various data types used to study the Arctic climate system, ranging from those sparse in location and frequency, but having the highest accuracy to those with high frequency spatially and temporally, but are prone to errors. Different data types are described in this section. Specific data used in calculation of the moisture flux are described in Chapter 4.2.

2.2.1 In Situ

The harsh environmental conditions of the Arctic in winter and its sometime inaccessible location have made the sea ice pack difficult to study. Meteorological observations over the ice pack have been taken via aircraft surveys, manned and automated observing stations, and onboard ships; but they are expensive to maintain and sparse in location and frequency [*Minnett and Key*, 2007]. When observations are taken they are often flawed due to the effects of meteorological conditions on the instruments. Freezing rain can affect wind measurements when instruments become encased in ice, extreme low temperatures can affect measurements of temperature and humidity, measurements from ships can be contaminated by the ship itself, and also human error can affect measurements [*Minnett and Key*, 2007]. Regardless, in situ observations have the smallest errors and are taken as "truth" when studying the Arctic.

2.2.2 Reanalysis data and Models

Reanalysis data are a good alternative to in situ data because they cover a wide range of spatial and temporal scales, but there are often inaccuracies with data in the Arctic. Reanalysis data rely on long-term and abundant observations to be reliable, but in the Arctic continuous long-term observations are sparse [*Bromwich et al.,* 2005]. This creates errors in the Arctic. *Francis* [2002] found biases between 25%-65% in the wind products from the NCEP-NCAR and ECMWF ERA-15 year reanalysis data compared with Arctic field campaign rawinsonde data (Figure 10). Temperature reanalysis data from ECMWF ERA-40 have also been shown to produce a warm bias in the Arctic mid to lower troposphere and should not be used in studies in the Arctic (Figure 11) [*Screen and Simmonds,* 2010].

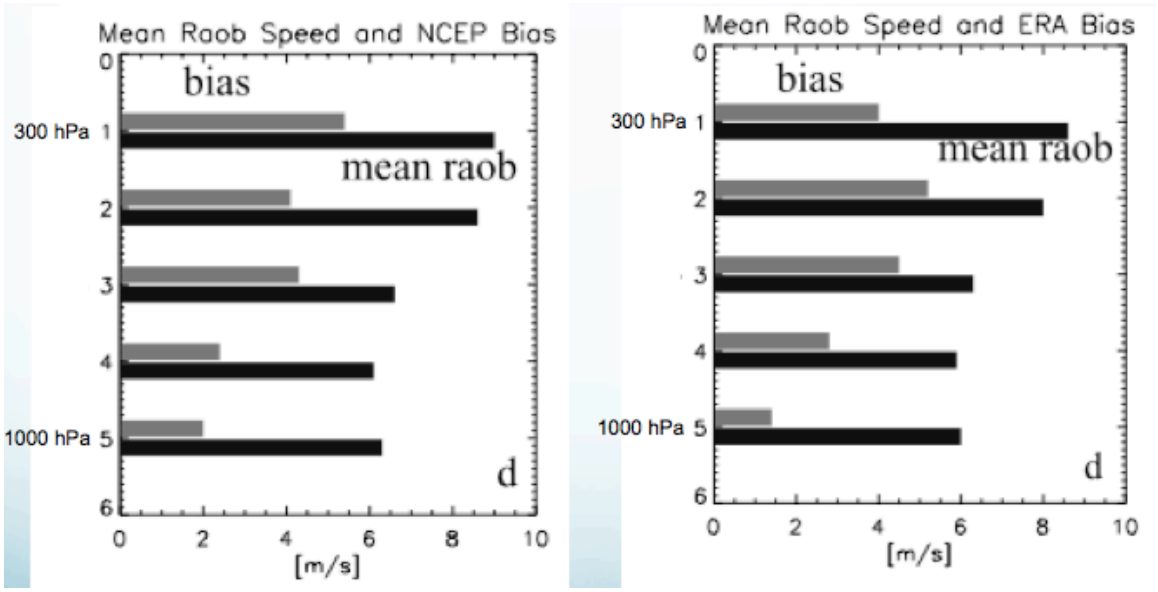

Figure 10. Images show comparisons of NCEP/NCAR and ECMWF Reanalysis upper-level winds to measurements by rawinsondes (raob) during the CEAREX and LeadEx Arctic field programs. Layers 1-5 are bounded by the following pressure levels: 300, 400,

500, 700, 850, and 1000 hPa. Image on the left is the mean wind magnitude from rawinsondes and bias in the NCEP/NCAR speed. Image on the right is the mean magnitude from rawinsondes and bias in the ECMWF speed. From *Francis* [2002].

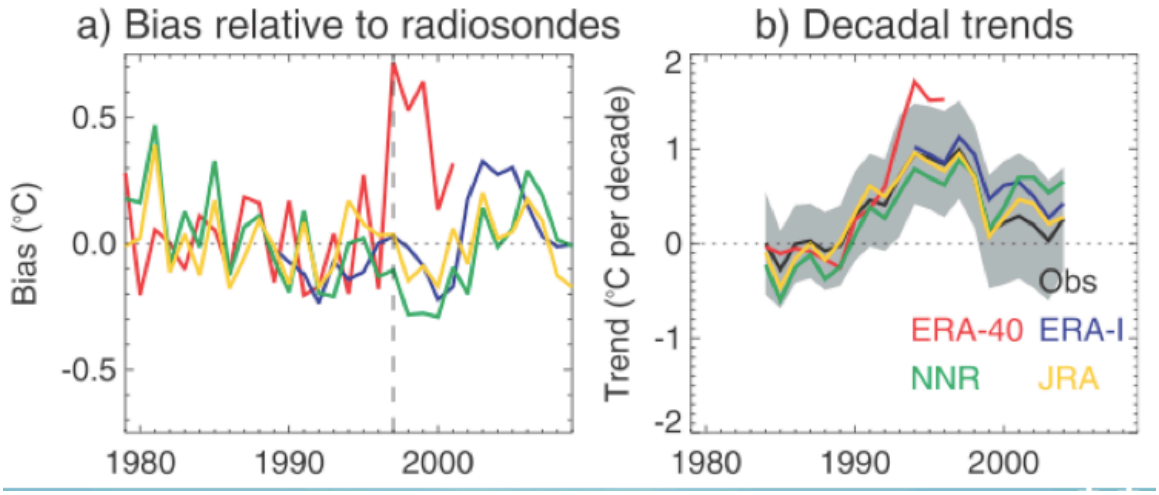

Figure 11. a) Arctic and annual mean 700 hPa temperature bias in each reanalysis relative to radiosondes. The radiosonde data are averages from nine Arctic stations. The reanalysis temperature fields were first subsampled at the station locations and then average over all subsampled grid boxes. For each reanalysis, the mean bias was removed to highligh the time varying component of the bias. b) Decadal Arctic and annual mean temperature trends from radiosondes and each reanalysis. Trends are centered on the indicated year (e.g., the trend at 1995 is based on data from 1990-2000). The gray band denotes the 95% confidence intervals of the trends. From *Screen and Simmonds,* [2010].

Moisture fluxes are already available from atmospheric model reanalyses, but recent studies have demonstrated that reanalyses suffer from serious errors in moisture variables. For example, *Cullather et al*. [2000] showed that in the NCEP/NCAR and NCEP/DOE reanalyses the annual net precipitation (precipitation minus evaporation) is about 60% lower than the water vapor flux convergence, although they should be equal. *Jakobson and Vihma* [2010] demonstrated that the ERA-40 reanalysis of the ECMWF and rawinsonde sounding data disagree on the vertical distribution of moisture transport to the Arctic. *Lüpkes et al.* [2010] showed that the ERA-Interim reanalysis has a large moist bias

in the lowermost 1 km over the Arctic Ocean. Comparing reanalysis data with the Tara drifting station in 2007, *Jakobson et al.* [2012] found that Era-Interim, JCDAS, NCEP-CFSR, NCEP-DOE and NASA-MERRA all had large errors in near surface air temperature, humidity and wind speed. The root mean square errors between all of the reanalyses ranged from 2.61-5.30 °C for air temperature, 0.14-0.40 g/kg for specific humidity, 15.3-16.8% for relative humidity and 1.80-2.91 m/s for wind speed when compared to tethered sounding data from the Tara drifting station (Figure 12). *Serreze et al.* [2009] also found biases in variables such as temperature, humidity, and wind speed are about the same or larger than recent climatological trends. Hence, there is a strong need to develop alternative methods to estimate the moisture fluxes at the atmosphere-ocean interface.

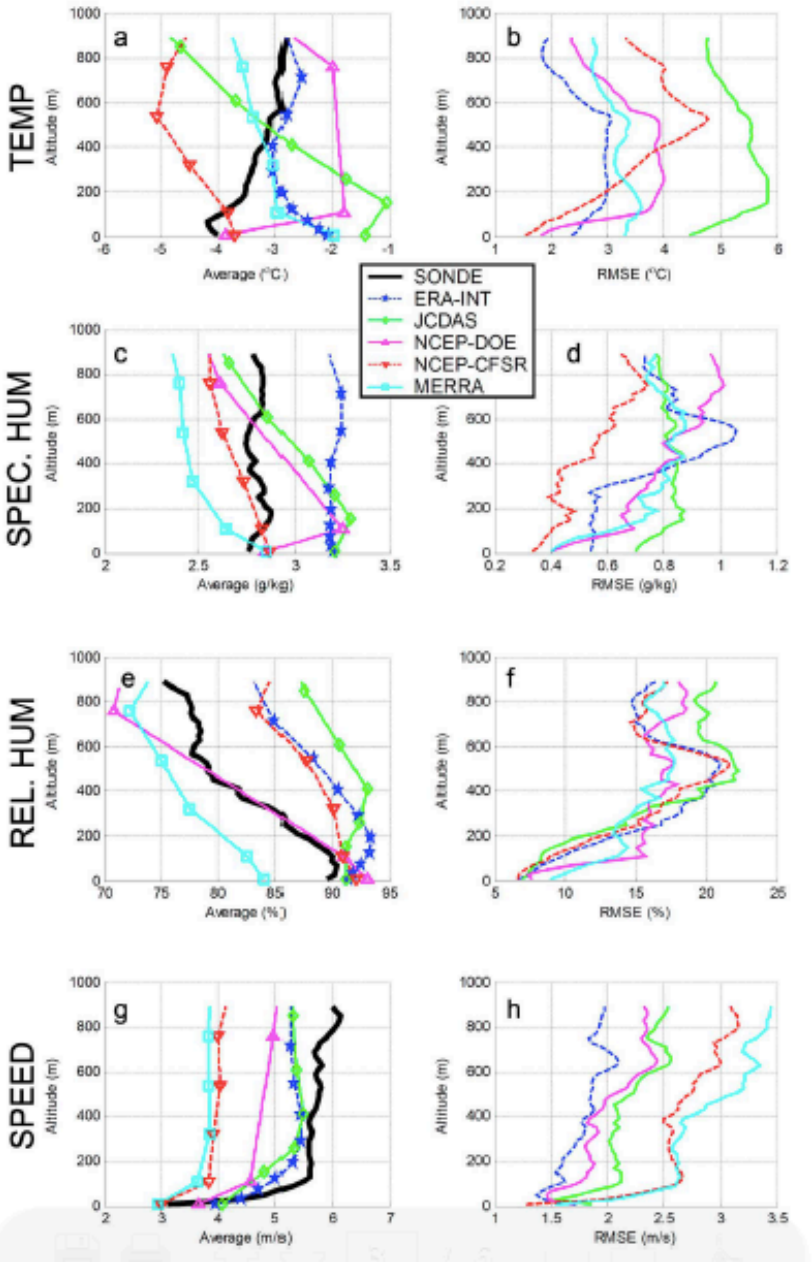

Figure 12. From 29 single profiles calculated: (a) average temperature, (b) RMSE (root mean square error) of temperature, (c) average specific humidity, (d) RMSE of specific humidity, (e) average relative humidity, (f) RMSE of relative humidity, (g) average wind speed, (h) RMSE of wind speed. From *Jakobson et al.* [2012].

The Arctic climate system poses many challenges in its representation in global climate models [*ACIA*, 2005]. The 2012 IPCC assessment shows that the largest

disagreements between models and actual climate change occur in the Polar Regions [*Stroeve et al., 2012*]. Climate models have a hard time representing the dynamics of the Arctic climate system, and because of this they are not able to accurately represent the rapid loss of sea ice extent in recent years (Figure 13). Global climate models show the largest disagreements from the present day climate of the Arctic, and this shows the weaknesses of our current state of knowledge of the dynamics and processes of the ice-ocean-air system [*Randall et al.,* 1997]. Atmospheric general circulation models have difficulty with turbulent fluxes of moisture, and thus representation of boundary layer clouds in the Arctic because the Arctic's atmospheric boundary layer differs from that of the mid-latitudes [*IPCC*, 2001]. Models use the Monin-Obukhov similarity theory to estimate the turbulent fluxes and while these work well for the mid-latitudes, they underestimate these fluxes in the Arctic. This is because they do not contain parameterizations that can accurately access very stable stratified conditions, which are often present over the sea ice [*Poulus and Burns,* 2003]. Improvements to these parameterizations to better describe the surface-atmosphere energy exchange would create more accurate models containing Arctic sea ice [*Dethloff et al.,* 2001].

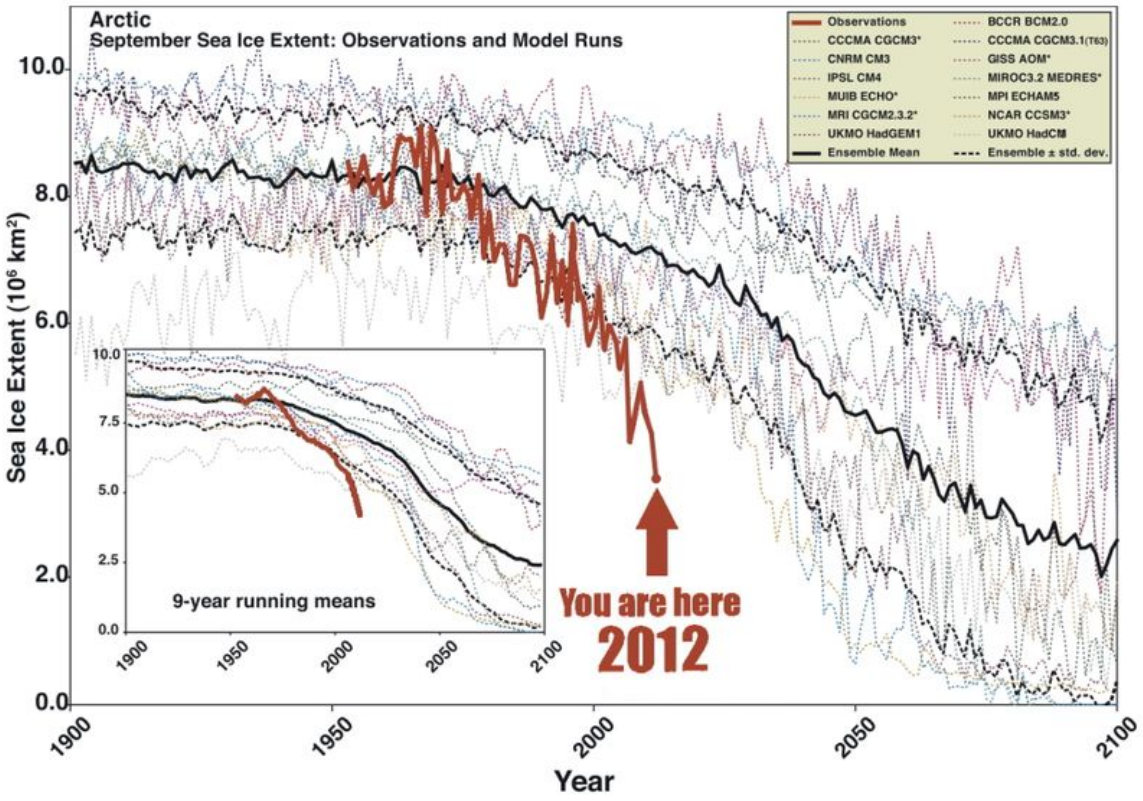

Figure 13. Arctic September sea ice extent (x 10^6 km^2) from observations (thick red line) and 13 IPCC AR4 climate models, together with the multi-model ensemble mean (solid black line) and standard deviation (dotted black line). Models with more than one ensemble member are indicated with an asterisk. Inset shows 9-year running means. From *Stroeve et al., 2007.*

2.2.3 Satellites

Today, multiple satellites orbit the Earth collecting a multitude of data on the surface of the earth and its atmosphere. Satellites are either geostationary, remaining above the same spot on the Earth, or polar orbiting, passing by the equator at the same time each day as the Earth rotates underneath. Polar orbiting satellites make full global

coverage every few days, with the Polar Regions receiving coverage multiple times a day [*Comiso,* 2010]. Satellites used to study the Arctic climate system mainly use visible, infrared and microwave frequencies depending on what geophysical feature of the surface or atmosphere that they are trying to detect [*Comiso,* 2010]. Sensors onboard these satellites are either passive or active. Passive sensors measure the radiation that is naturally emitted from a source; in the visible spectrum it is shortwave radiation, and in the infrared it is longwave radiation [*Comiso,* 2010]. Active sensors, on the other hand, generate a signal and transmit it to the target and record the signal after it has returned to the sensor, being altered by the target that it interacted with [*Comiso,* 2010].

While not all of the satellites and sensors are discussed in this section a brief overview is supplied in the following subsections.

2.2.3.1 Passive Remote Sensors

Visible and infrared channels are used concurrently in most satellite sensors in order to gain as much information about the Earth and the atmosphere as possible. The suite of Landsat satellites, starting with Landsat 1 was launched in 1972 and continued operating until 2003, carried a series of multispectral scanners in the visible and infrared spectrum. Each Landsat provided higher resolutions, which were needed for validation studies in the polar regions [*Comiso,* 2010]. Another suite of remote sensors that has provided long-term, continuous records used for studying interannual variability in the Arctic is the Advanced Very High Resolution Radiometer (AVHRR), which was first launched on the TIROS-N satellite in 1978 and is still in operation today.

Since the late 1970's there have been many more satellites carrying visible and infrared sensors developed and launched such as Terra in 1999 and Aqua in 2002. Both Terra and Aqua are polar orbiting satellites, but Terra crosses the equator in the morning whereas Aqua crosses in the afternoon. One sensor onboard both satellites is the Moderate Resolution Imaging Spectroradiometer (MODIS). It is used to measure the physical and biological characteristics of the Earth's surface and its atmosphere [*Comiso,* 2010]. The Multi-angle Imaging Spectro-Radiometer (MISR) is another sensor onboard Terra that has different viewing angles and has allowed for more accurate surface classifications of the snow and ice [*Comiso,* 2010]. Another key instrument on Aqua is the Atmospheric Infrared Sounder (AIRS), which is covered in more detail in section 4.2.1.

Passive microwave sensors allow for data collection in both daytime and nighttime and in all types of meteorological conditions unlike visible and infrared. Thus, passive microwave sensors have changed how we view the Arctic sea ice by providing daily, high resolution, long-term data used to create sea ice extent maps. This enabled studying the inter-annual variations of the sea ice pack and well as the effects of climate change. This data record began with the launch of the Scanning Multichannel Microwave Radiometer (SMMR) onboard the Nimbus-7 in 1978 [*Comiso,* 2010]. This sensor lasted until mid 1987 and was succeeded by the Special Scanning Microwave Imager (SSM/I) in 1987. This sensor has been onboard a series of Defense Meteorological Satellite Program (DMSP) satellites since 1987 and still provides valuable data.

Aqua also has microwave sensors onboard, allowing for the complete frequency spectrum of radiation to be captured over the Earth at the same time and along the same

satellite track. This microwave sensor is the Advanced Microwave Scanning Radiometer (AMSR-E), and it is covered in more detail in section 4.2.2.

2.2.3.2 Active Remote Sensors

There are four different types of sensors that use active remote sensing: high resolution imaging systems, scatterometers, radar altimeters, and laser altimeters. The only high resolution imaging system that works in the microwave spectrum is the Synthetic Aperture Radar (SAR) [*Comiso,* 2010]. Using its long wavelengths it can penetrate the snow and ice sheet providing information that is not available with other type of sensors. Some satellites that contain SARs are ENVISAT, ERS1/SAR and Radarsat/SAR.

Scatterometer operate the same way as radar except scans the surface along a 360° elliptical track [*Comiso,* 2010]. Information on wind speed and direction near the ocean surface can be obtained by looking at the backscatter. One example of this sensor is QuikSCAT.

Radar altimeters send out a signal and the backscatter from the signal is what is detected. The more uniform the surface is the more uniform the radiation spreads out and then is backscattered to the sensor. These altimeters are used to study the topography and thickness in the Arctic sea ice cover. An example of this type of sensor is the Cryosat2 satellite, which was launched in 2010.

Laser altimeters send out laser pluses to measure the topography of the surface. The Geoscience Laser Altimieter System (GLAS) is the first Lidar system to be used successfully onboard ICESat, which was launched in 2003 [*Comiso,* 2010]. Using two

laser beams at different wavelengths it was able to measure the topography of the sea ice as well as its thickness and also clouds. ICESat2 is set to launch in 2016.

Chapter 3: Arctic Sea Surface Temperatures 1982-2009

3.1 Background

The Arctic sea ice pack has undergone drastic changes since the dawn of the satellite era, and the ice-ocean relationship between the sea ice cover, the sea surface temperatures (SSTs) and the freeze onset is changing with the sea ice.

The Arctic Ocean is fairly isolated and shallow, having just two deep basins and only exchanging water between the Fram Strait, the Barents Sea, the Bering Strait and the Canadian Archipelago [*Grotefendt et al*., 1998].

Since 2000, the multi-year ice area has decreased at a faster rate than previous years and was 20% smaller than in 1982 [*Nghiem et al*., 2007]. Studying the ice-ocean system pre-2000 and post-2000 will allow us to better understand how the rate of the shrinking sea ice pack is changing the SSTs in the Arctic Ocean as well as the re-freeze of the ocean in the autumn.

3.2 Data

Daily SST data are taken from NOAA Optimum Interpolation ¼ Degree Sea Surface Temperature Analysis. This data set is produced from the Pathfinder Advanced Very High Resolution Radiometer (AVHRR) for the years 1982-2005, the Operational

AVHRR for the years 2006-2009 and in situ observations from ships and buoys (data from: http://www.ncdc.noaa.gov/oa/climate/research/sst/oi-daily-information.php). Satellite biases are adjusted with respect to the in-situ data [*Reynolds et al.,* 2007]. This optimum interpolation method significantly reduces the 0.6 K SST error from AVHRR alone.

Ice concentration data are produced from SMMR and SSM/I brightness temperatures using the Enhanced NASA Team (NT2) algorithm [*Markus and Cavalieri*, 2000] and is defined as the percentage of a pixel that is covered by sea ice. Ice concentration is available every other day from 1982 until July 7, 1987 and daily from July 9, 1987 for the rest of the record. The error on the location of the sea ice edge was found to be +/- 25 km^2 [*Heinrichs et al.,* 2006].

Yearly melt and freeze onset maps of the Arctic sea ice are created by daily averaged brightness temperatures from SMMR and SSM/I for the years 1979-2009 and are taken from *Markus et al.* [2009]. When snow is melting and wet it produces a different brightness temperature then the completely frozen snow, and this is also true for when ice melts exposing the sea surface. Melt and freeze onset are classified as a day of the year for each pixel when the brightness temperatures signals change drastically due to scattering.

3.3 Results

Since 1982, the June (J), July (J), August (A), September (S) and October (O) (JJASO) SSTs in the Arctic have been on the rise. The average increases have been 0.82 °C. The largest increases are seen in August and September, with some areas increasing around 3 °C over the time period (Figure 14). The largest increases are seen in the Chukchi/Beaufort Seas, the E. Siberian Sea, the Barents Sea, the E. Greenland Sea and Baffin Bay. Reasons for these increases in the Chukchi/Beaufort and E. Siberian Seas are from the reduced sea ice cover in the summer and autumn. More open water reduces the albedo, allowing for larger absorption of heat, raising the SSTs. The sea ice concentrations in the Chukchi/Beaufort and E. Siberian Seas have been decreasing at 9.5 %/decade and their subsequent SSTs have been increasing 0.5 °C/decade. The E. Greenland Sea, Barents Sea and Baffin Bay are influenced by warmer ocean waters from the Gulf Stream and North Atlantic Current that have propagated into the area during the SST record [*Chepurin and Carton*, 2012].

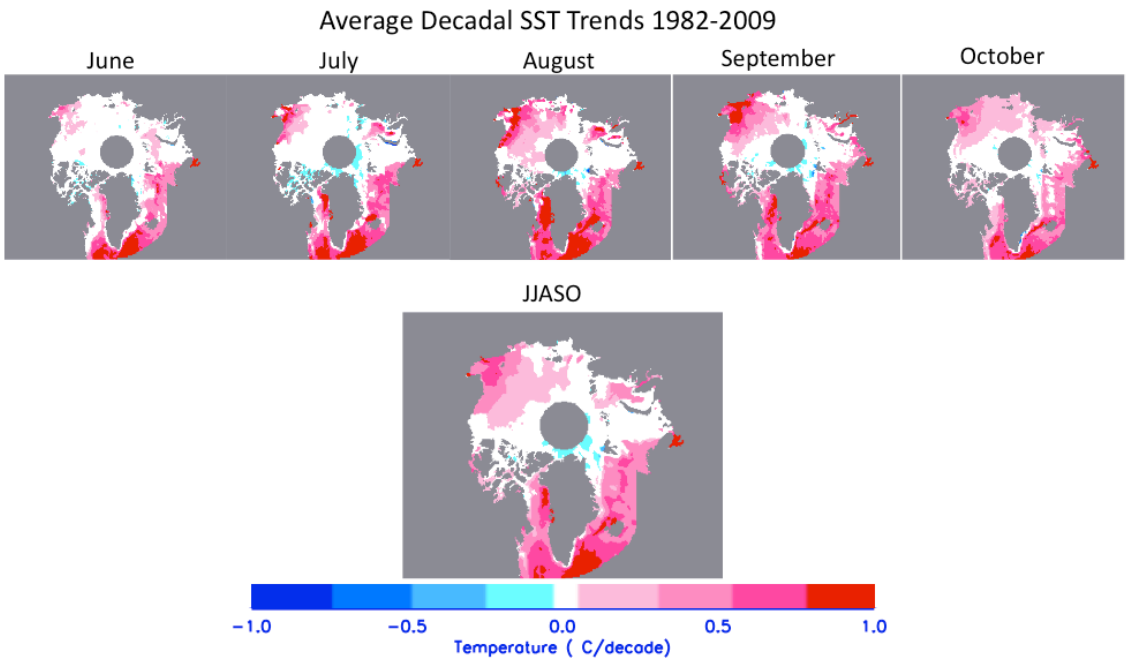

Figure 14. Average decadal SST trends for June, July, August, September and October separately and JJASO, 1982-2009. All trends are significant at the 95th percentile.

Figure 15 (top) shows the decadal trends of SSTs, freeze onset and ice concentration from 1982-2009 that are statistically significant at the 95th percentile. These images look very similar spatially. Areas in the Chukchi/Beaufort and Laptev/E. Siberian Seas that have seen decreases in ice concentration have increases in SSTs and also have large delays in freeze onset, between 10-20 days/decade. This same pattern is seen in the Kara Seas and also in Baffin Bay. Areas with warming SSTs appear to be causing a delay in the reformation of the sea ice because warmer SSTs require longer time to lose heat to the atmosphere and reach the freezing point for freezing to begin. Along the E. Greenland coast and southern Baffin Bay where ice no longer freezes in the fall months (dark blue areas of freeze onset in Figure 15) is where SST trends are specifically high.

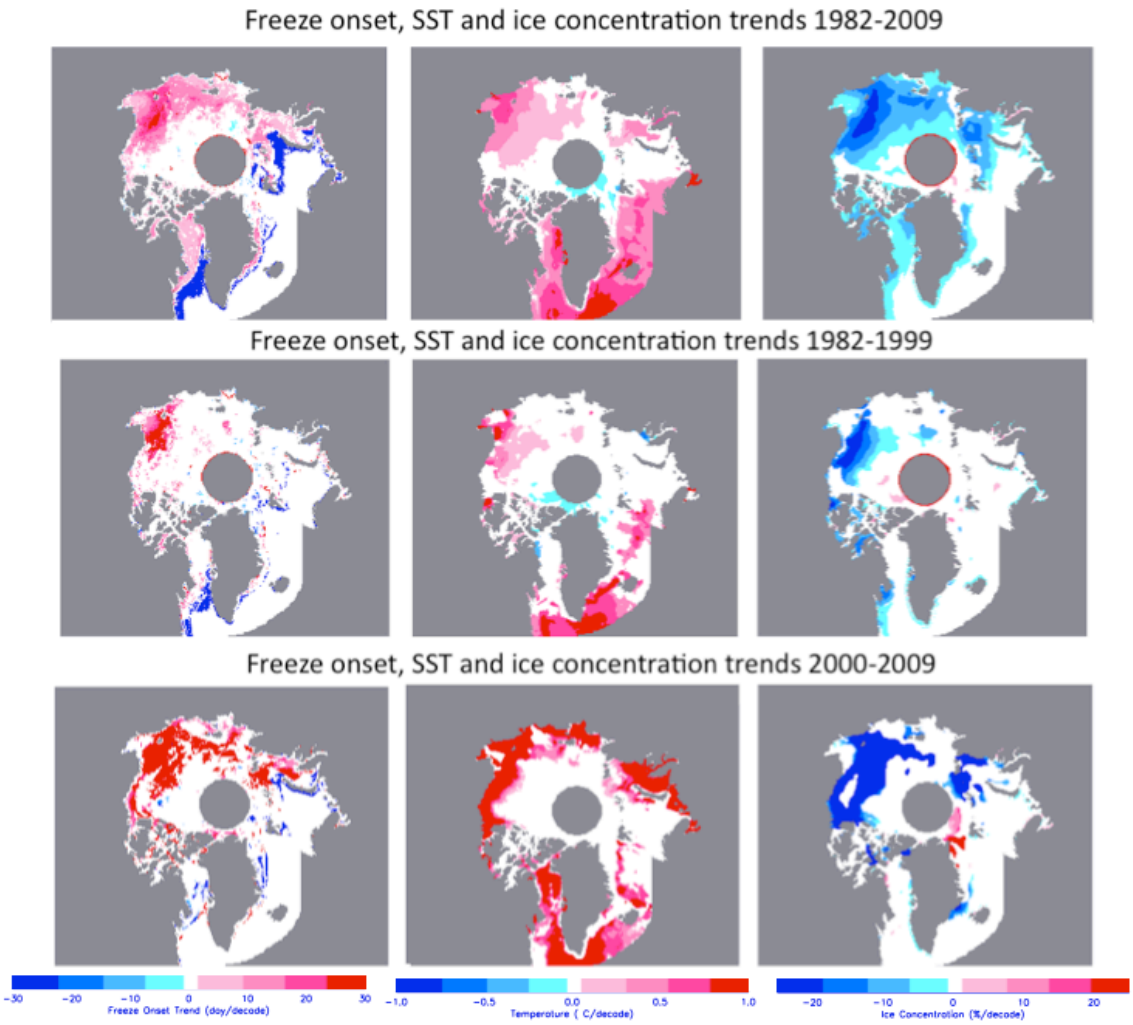

Figure 15. Decadal freeze onset, SSTs and ice concentration trends for 1982-2009 (top), 1982-1999 (middle) and 2000-2009 (bottom). All trends are significant at the 95th percentile.

The 28-year SST record was split into two time periods: 1982-1999 and 2000-2009, in order to study the SST changes with the changes in sea ice concentration. Since 2000, the sea ice concentration in the entire Arctic has decreased at 3.5 times the rate as before 2000, allowing us to look at changes in SSTs in a slow and rapid changing sea ice pack in the summer and autumn months.

3.3.1 Entire Arctic: 1982-1999 and 2000-2009

In this area, the SSTs are becoming warmer in JJASO, increasing 0.82 °C over the 28-year record. The majority of this increase occurred between 2000-2009, specifically in August and September (Figure 15). Figure 16 shows weekly trends of ice concentration and SSTs as well as their weekly averages for 1982-1999 and 2000-2009. The SSTs from 1982-1999 increased at about 0.02 °C/year each week in JJASO, and there were no large increases. On the contrary between 2000-2009, the trends in June remain close to that of the earlier time period, but then jump up dramatically during the rest of the season, becoming almost 0.10 °C/year in August. This is similar to the sea ice concentration over the same area. During the 1982-1999 period, the weekly sea ice concentration was decreasing at 0.26%/year and was constant over the season. The ice concentration from 2000-2009 decreased at 0.90 %/year, and the decrease of the ice concentration increases over the season, with the highest rates of loss in September and October. In June and July, larger decreases in ice concentration allow for increases in SSTs later in the summer. From Figure 16, we can see that the increasing weekly trends in SSTs in the later half of the record precede the large decreases in sea ice concentration. In this area it seems that the increases in the SSTs in August and September increase the rate of ice melt in September and October, decreasing the sea ice concentration. These increases in SSTs are also contributing to the delay in freeze onset in the fall in recent years (Figure 15 middle and bottom). Since 2000, the freeze onset date has been increasing 1.41 days/year, whereas before 2000 the freeze onset was delayed only 0.17 days/year.

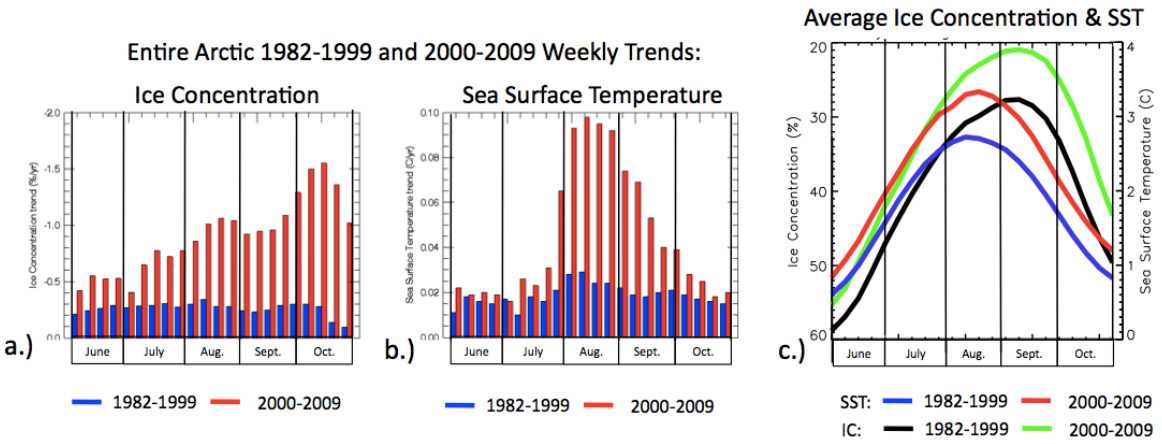

Figure 16. Entire Arctic 1982-1999 and 2000-2009 weekly trends in a.) ice concentration, b.) sea surface temperature and c.) Average ice concentration and SSTs for 1982-1999 and 2000-2009.

On a monthly basis, the trends in SSTs were about the same in June for both time periods, but then began to increase to 1.9, 3.5, 2.9 and 1.5 the rate for JASO. This is similar to the ice concentration, they are similar for the two time periods in June, but then becomes much lower between 2000-2009 in AS.

Figure 15 shows the decadal trends in freeze onset, SSTs and ice concentration in JJASO for 1982-1999 (middle) and 2000-2009 (bottom). Between 1982-1999, the only locations of statistically significant trends in freeze onset occur in the Chukchi/Beaufort Seas region, which is similar spatially to the SST and ice concentration trends. Increases in SSTs during this time period are what caused the delay in freeze onset. Between 2000-2009, the freeze onset is being delayed at least 30 days/decade in the Chukchi/Beaufort, Laptev/E. Siberian and Kara Seas regions. In these same areas the SSTs are increasing at least 1 °C/decade, showing us that the trends in both freeze onset and SSTs have accelerated in the past 10 years and that warmer SSTs are the cause for the delayed freeze

onset in the autumn. This more recent time period is causing the majority of the changes throughout 1982-2009.

3.3.2 Chukchi/Beaufort Seas

The Chukchi/Beaufort Seas region has seen one of the largest sea ice concentration losses in the Arctic, with ice concentrations decreasing on average 0.93 %/year in JJASO. Over the entire record, the SSTs have increased 0.025 °C/year on average, but looking at individual time periods shows a different picture (Figure 17 a,b,c). Between 1982-1999, when the weekly ice concentration decreased 0.89 %/year the weekly SSTs only increased 0.027 °C/year, and these trends throughout JJASO remained close to constant, increasing only slightly in August. Between 2000-2009, weekly sea ice concentrations decreased at 2.6 times the 1982-1999 rate, and weekly SSTs have increased at 2.9 times the rate. Again, like the case for the entire Arctic, the SSTs and their weekly trends in June are almost identical between 1982-1999 and 2000-2009. Then in July the SSTs in 2000-2009 begin to increase dramatically to 2.6, 3.4, 2.9 and 2.8 times the earlier rates in JASO and the SSTs became 0.5 °C warmer. The weekly SSTs in June are identical in both time periods and this could be because the melt onset date trends are not changing in the 1982-1999 and 2000-2009 time periods. The SSTs increase much more rapidly in JAS in 2000-2009 and this could be caused by the rapid reduction in sea ice concentration (Figure 15 bottom). Similarly, the reduction rates in sea ice concentration increased steadily in July and August and then drop off rapidly in September, mimicking the SST trends and then the reduction rates in sea ice concentrations increase again in October. SSTs also remain

0.28 °C warmer in October than in earlier years. These warmer SSTs could be increasing side and bottom melting of the ice and this is why the decreasing sea ice concentration trends are much higher. Higher SSTs in this area during 2000-2009 are causing the freeze onset to be delayed at 2.6 times the rate compared to 1982-1999.

3.3.3 Laptev/E. Siberian Seas

This region has seen drastic changes in SSTs between the 1982-1999 and 2000-2009 periods (Figure 17 d,e,f). Trends in weekly SSTs in JJASO have increased 7 times the amount in 2000-2009, causing the weekly ice concentration to decrease at 4 times the rate compared to 1982-1999. The weekly SSTs are increasing at the same rate in both time periods in June and July, but then in ASO increases in SSTs jump rapidly to 10.4, 7.7 and 8.3 times the rate as in 1982-1999, respectively. The weekly SST trends start off with significant increases in August, and then these trends drop off more slowly in September and October. This is opposite of the weekly decreasing sea ice concentration trends. These weekly trends start off decreasing slowly in July and become larger until mid October. It is as if the large increases in SSTs precede the large decreases in ice concentration, leading us to believe that these increases in SSTs play a role in the decrease in sea ice concentration later in the season. In the earlier time period, 1982-1999, the increasing weekly trends in SSTs and the decreasing weekly trends in ice concentration do not change throughout the JJASO months and are small in comparison to the later time period. This is why the freeze onset is delayed only 0.36 days/year compared to 2.7 days/year in 2000-2009.

3.3.4 Kara/Barents Seas

The Kara/Barents Seas are not completely ice covered in the winter months and the Barents Sea receives ocean currents from the North Atlantic current. Due to this its SSTs are much warmer than the Chukchi/Beaufort and Laptev/E. Siberian Seas. The weekly SST trends in JJASO in 1982-1999 have decreased 0.09 °C and in 2000-2009 they have increased 0.56 °C (Figure 17 g,h,i). In both time periods, the SSTs in June were increasing at the same rate, then the SSTs change to decreasing trends for the rest of the season between 1982-1999. In contrast, the SST trends in 2000-2009, start off small and then increase rapidly in ASO, but these weekly increases are not as large as in the Chukchi/Beaufort and Laptev/East Siberian Seas. The weekly sea ice concentrations in 1982-1999 start off decreasing around 0.25 %/year in June and then become smaller throughout the season, eventually increasing in the last two weeks of October. Weekly sea ice concentration trends in 2000-2009, on the other hand, are negative throughout JJASO and are largest in October, and smallest in August and September. Large ice concentration losses in June and July help to raise SSTs in August and September and in October SSTs are 0.48 °C warmer compared to 1982-1999. This would explain why the freeze onset was only delayed 2.2 days between 1982-1999 and 9.2 days between 2000-2009.

3.3.5 East Greenland Sea

In this region, the SSTs in 2000-2009 are much warmer than those in 1982-1999 even though the sea ice concentration is only slightly less. Even though SSTs are much warmer in the more recent time period they are only increasing at about half of the weekly rate as before in JJASO (Figure 17 j,k,l). The large increases in SSTs in the 1982-1999 period could be due to an increased warming of the subpolar gyre and a decrease in the North Atlantic Oscillation index, which moves winter storm tracks farther south and is highly anti-correlated with SSTs in the region [*Chepurin and Carton*, 2012]. On a monthly basis, trends in SSTs are only larger in 2000-2009 in June. SST trends are the same in July for both time periods and then the 2000-2009 trends become much less during the rest of the season. This is different from any other region because in the other regions, the SST trends were largest in 2000-2009. However in this 2000-2009 period, they start out positive and then drop off to negative weekly trends in October. This can explain why the freeze onset day is actually occurring 7.2 days earlier throughout 2000-2009. This is also a mirror image of how the weekly sea ice concentration trends look for 2000-2009. The weekly sea ice concentrations are only decreasing in June and then increase during the rest of the season. This is similar to the sea ice concentration trends in 1982-1999 except the magnitude is much smaller. The weekly SST trends in 1982-1999 are all positive and have largest trends in August and September.

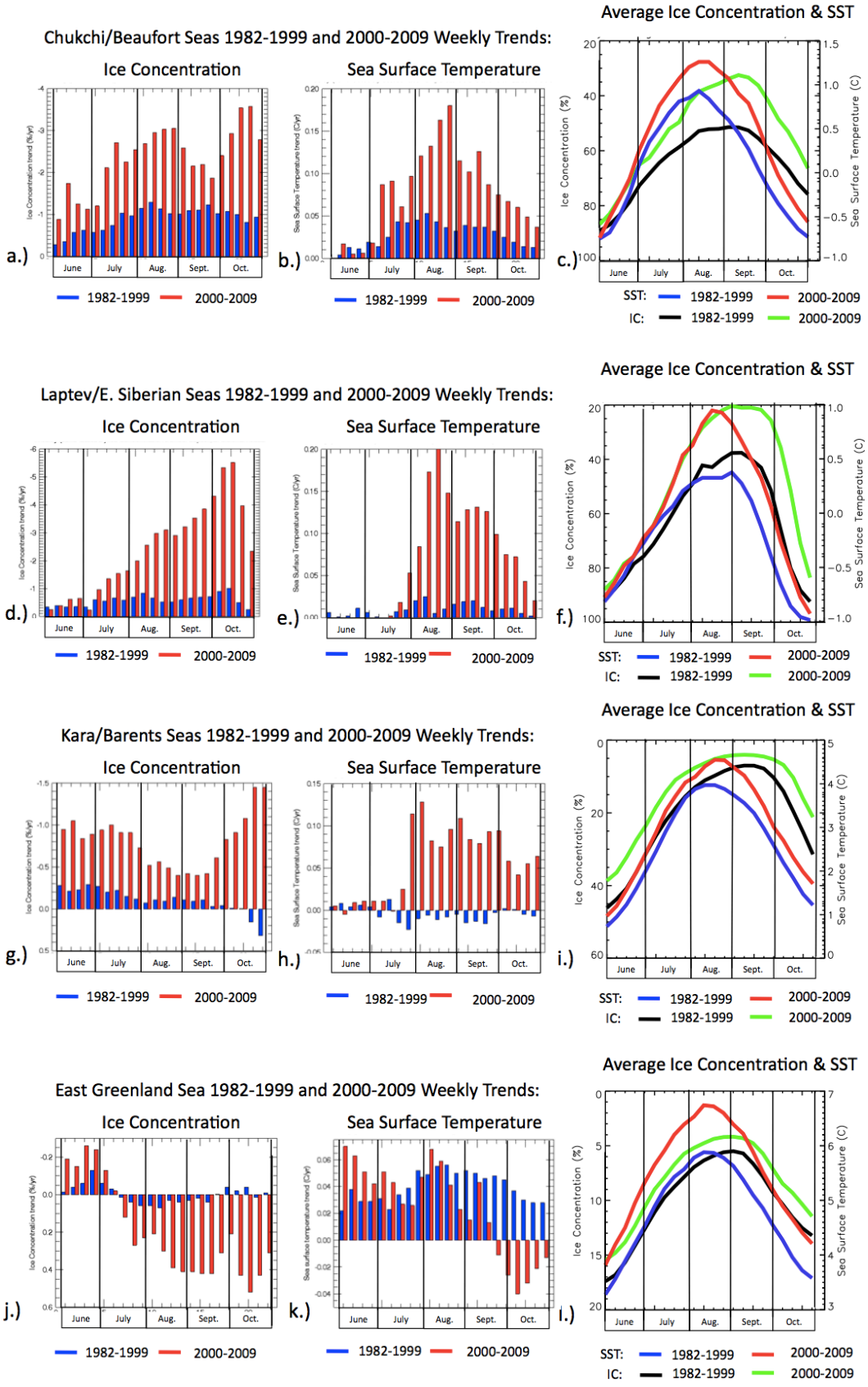
Chukchi/Beaufort Seas 1982-1999 and 2000-2009 Weekly Trends:
Ice Concentration
Sea Surface Temperature
Average Ice Concentration & SST
a.)
b.)
c.)
June
July
Aug.
Sept.
Oct.
1982-1999
2000-2009
Ice Concentration (%)
Sea Surface Temperature (C)
SST:
IC:
Laptev/E. Siberian Seas 1982-1999 and 2000-2009 Weekly Trends:
d.)
e.)
f.)
Kara/Barents Seas 1982-1999 and 2000-2009 Weekly Trends:
g.)
h.)
i.)
East Greenland Sea 1982-1999 and 2000-2009 Weekly Trends:
j.)
k.)
l.)

Figure 17. 1982-1999 and 2000-2009 weekly trends in ice concentration, SST and average ice concentration for the Chukchi/Beaufort Seas (a,b,c), Laptev/E. Siberian Seas (d,e,f), Kara/Barents Seas (g,h,i) and the E. Greenland Sea (j,k,l).

3.3.6 Sea Surface Temperatures and Freeze Onset

We wanted to determine if the excess heat at the ocean surface in 2000-2009 compared to 1982-1999 was enough to delay the freeze onset. Following equation 2 in *Steele et al.* [2008]

$$\Delta t = \frac{OHC}{\rho_{air} cp_{air} ch_{aw} \Delta T_{aw} W_{10m}} \quad (1)$$

and their assumptions: t is the time in seconds, the upper ocean heat content OHC MJ m^{-2}, the air density ρ_{air} = 1.3 kg m^{-3}, the air heat capacity $cp_{air} = 10^3$ J kg^{-1} °C^{-1}, the air water heat exchange coefficient $ch_{aw} = 10^{-3}$, the air-water temperature difference ΔT_{aw}= 5-10°C ,the 10m wind speed W_{10m}= 5-10 m s^{-1}, and that the ocean-ice advection is small. We were able to calculate the amount the freeze onset would be delayed and compare it to the actual delay.

We took the range in SSTs differences between 2000-2009 and 1982-1999 for all the locations and estimated their subsequent upper OHC, assuming that the summer mixed layer depth was 20m, following *Steele et al.* [2008]. Substituting into (1) we estimated the range over which the freeze onset would be delayed, took the average and then compared it to the average freeze onset differences between 2000-2009 and 1982-1999 (Table 1). Our estimated delay in freeze onset for the Chukchi/Beaufort, Laptev/E. Siberian and Kara/Barents Seas differed by 0.60 days on average. The E. Greenland Sea produced a

discrepancy of 8.69 days and this is because the majority of the area is open water year round and the North Atlantic Current does affect its SSTs. For the entire Arctic the estimated delay was off by 2.28 days, which was larger than expected due to the E. Greenland Sea. Since our estimated delay in freeze onset between 1982-1999 and 2000-2009 was very close to the actual delay, we find the excess heat stored in the ocean surface could be causing the delay of the freeze-up of the ice in the fall in 2000-2009.

Table 1. SST differences between 2000-2009 and 1982-1999, their subsequent upper OHC, the actual freeze onset differences, and the estimated freeze onset differences using equation 1.

1. Location	2. SST range (C)	3. OHC range (MJ/m2)	4. Δ Freeze Onset (days)	5. Estimated Δ Freeze onset (days)	6. Ave. estimated Freeze Onset (days)	7. Difference (Actual-Estimated) (days)
Entire Arctic	0.23-0.63	22.08-60.48	14.03	1.96-21.53	11.75	2.28
Chukchi/ Beaufort Seas	0.01-0.52	0.96-49.92	8.34	0.085-17.78	8.93	-0.59
Laptev/E. Siberian Seas	0.02-0.62	1.92-59.52	10.06	0.17-21.20	10.68	-0.62
Kara/ Barents Seas	0.24-0.66	23.04-63.36	11.73	2.05-22.56	12.31	-0.58
E. Greenland Seas	0.24-0.54	51.84-82.56	8.32	4.62-29.40	17.01	-8.69

3.4 Summary

The fact that SSTs in the Arctic are have been increasing since the early 1980's is well known, but what is interesting is that the majority of this warming has occurred since 2000. Since 2000, increases in SSTs have accelerated at 2.7 times the rate seen in 1982-1999. Also since 2000, the percentage of the ice-free area in JJASO has increased at 7 times the rate as in 1982-1999 and the delay of freeze onset is occurring at 8.3 times the rate as in 1982-1999. What could be causing this accelerated warming of SSTs in recent years is an increase in ice loss, which allows for more absorption of heat into the ocean surface, accelerating melting. SSTs were much warmer in the 2000-2009 period because the Arctic was on average 52% ice free in JJASO. This reduction of sea ice since 2000 could be caused by the negative phase of the Arctic dipole and the positive phase of the Arctic oscillation sea level pressure and wind pattern. During these phases, the winds force the sea ice from the Bering Strait towards the North Pole and also allow for large amounts of sea ice to be transported out through the Fram Strait [*Overland and Wang*, 2009]. Before 2000, this Arctic dipole was predominately positive allowing for larger sea ice coverage in the summer months [*Overland and Wang*, 2009]. This much larger area of open water since 2000 allowed for an increase of solar energy into the ocean surface [*Perovich et al.,* 2007]. These higher SSTs significantly delayed the freeze onset because it takes longer time for enough heat to be expelled into the atmosphere before freezing of seawater can occur. We demonstrated that this is occurring in all regions of the Arctic, using (1), except for the E. Greenland Sea, which has minimal ice coverage throughout the year and is also affected by other ocean currents.

In the Pacific sector, regions like the Chukchi/Beaufort and Laptev/E. Siberian Seas, melting of the ice early in the season is caused by increases in short and long wave radiation. The accelerated warming of SSTs is due to a diminished sea ice cover causing larger heating of the ocean surface from the atmosphere and higher SSTs later in the season increase side and bottom melting of the ice. These are similar results to those found by *Steele et al.* [2010], which were discussed in Chapter 1. The regions in the North Atlantic [the Kara/Barents and E. Greenland Seas], on the other hand are more affected by the surface currents of the Gulf Stream and the North Atlantic Current that have been warming, rather than a loss in sea ice cover.

Besides just delaying the freeze onset of the sea ice and making it more susceptible to melting in the spring, the increases in SSTs are significant because they can affect the surface sensible heat and evaporation rates, which both contribute to Arctic warming and could also slow down the thermohaline circulation. The red line in Figure 33 shows the moisture flux from the ocean between 2003-2009. Increases in moisture during this time period are evident in autumn because of warming SSTs during those years. Specifically, increases in moisture could increase the amount low level clouds in the Arctic, which have be found to warm the Arctic. Water vapor is also a green house gas, so having more moisture in the atmosphere enhances the warming of the Arctic and increases ice melting.

Chapter 4: Arctic Ocean Moisture Fluxes

4.1 Approach

Here, moisture flux is defined as the vertical flux of surface moisture due to atmospheric turbulent transport. It is a function of the difference in specific humidity between the surface and air as well as the factors affecting the intensity of turbulent exchange: wind speed, surface roughness, and thermal stratification [e.g., *Launiainen and Vihma*, 1994].

$$E = \rho C_E (q_s - q_a) V_{10m} \quad (2)$$

where ρ is the air density, C_E is the water vapor transfer coefficient, q_s is the saturation specific humidity at the ice/polynya surface, q_a is air specific humidity at 2 m, and V_{10m} is the wind speed at 10 m. q_a is calculated on the basis of air temperature and relative humidity. In the winter, there is little exchange of moisture between the surface and the atmosphere over the thick, insulating sea ice due to low relative humidity and the small differences between surface and air temperature [*Dare and Atkinson*, 1999]. Where thin or no ice is present, however, the large temperature difference between the water and atmosphere allows for large exchange of moisture. Moisture fluxes over open water (0.05 g/m^2s) are sometimes 25 times as large as fluxes over thick ice (0.002 g/m^2s) in the winter [*Launiainen and Vihma*, 1994] (Figure 18).

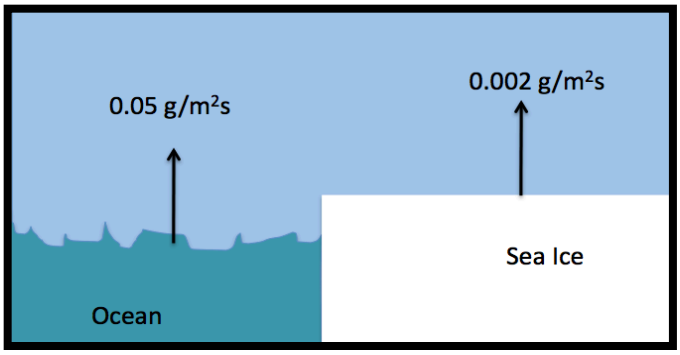

Figure 18. Typical magnitudes for the moisture flux for open water versus sea ice in the Arctic.

The flux of moisture from the ocean to the atmosphere is an important parameter when studying polynyas, because this moisture enhances fog, plume, and cloud formation above and downwind of the polynya [*Arbetter et al*., 2004]. This warm, moisture rich air from the polynya cools, condenses, and forms fog layers that can rise tens to hundreds of meters [*Smith et al.,* 1983; *Walter,* 1989].

There have been numerous studies done that have computed the surface fluxes of sensible and latent heat over the Arctic ice pack using in situ data from weather stations, field campaigns and reanalysis [*Maykut,* 1982; *Serreze et al.,* 2007]. Few have focused on the moisture flux and estimating it using primarily satellite data.

4.2 Data

We use sea ice concentration to study the evolution of the Arctic sea ice pack size and shape over time, and we use surface and air temperature, relative humidity, sea surface temperature, and wind speed to calculate the moisture flux.

We utilize data from sensors on board NASA's Earth Observing System (EOS) Aqua satellite to examine the North Water polynya and the entire Arctic's moisture fluxes. Aqua was launched on May 4, 2002, and continues to operate. Aqua carries six Earth-observing instruments that collect a wide variety of global data [*Parkinson,* 2003]. It has a near-polar low-Earth orbit with a period of 98.8 minutes and equatorial crossing times of 1:30 a.m. and 1:30 p.m. Specifically, we use data from the Japan Aerospace Exploration Agency (JAXA)'s Advanced Microwave Scanning Radiometer for EOS (AMSR-E) for ice concentration and sea surface temperature fields and data from NASA's Atmospheric Infrared Sounder (AIRS) for temperature, relative humidity and geopotential height fields.

4.2.1 AIRS

AIRS is a cross-track scanner collecting data with a 13.5 km spatial resolution in the horizontal and 1 km resolution in the vertical. It has 2378 infrared channels and four visible/near infrared channels, which obtain highly accurate temperature and humidity profiles and many other physical products dealing with the Earth and its atmosphere. From AIRS we use surface skin temperature measured in Kelvin, the air temperature at 1000 hPa measured in Kelvin, and relative humidity at 1000 hPa expressed as a percentage. We use the geopotential heights from AIRS in order to determine the actual heights of the 1000 hPa level. Both the temperature and relative humidity products are level quantities, which means that the values are reported at fixed pressure levels. This differs from layer quantities, which are reported on the fixed pressure levels, but represent the layer bounded

by the level on which they are reported and the next height level (in altitude). Thus the 1000 hPa temperatures and relative humidity are not vertical averages [*Fishbein et al.,* 2011]. The vertical resolution does not vary with elevation because the temperature and humidity profiles are obtained from a 100 level support product temperature or humidity profile using interpolation that is linear to the logarithm of the support pressure [http://disc.sci.gsfc.nasa.gov/AIRS/documentation/v5_docs]. These values are used in the calculation of the moisture flux and are Level 3 mean daily gridded products covering a 24-hour period for the ascending (equatorial crossing south to north at 1:30 p.m. local time) portion of the orbit [*Aumann et al.,* 2003]. In the Polar Regions, Aqua makes multiple passes over the study area each day, allowing for daily averages to be produced. These parameters are put onto a 1° x 1° grid covering the entire Earth.

4.2.2 AMSR-E

AMSR-E is a conically scanning global passive microwave radiometer that has 12 channels, with horizontal and vertical polarizations for each of its six frequencies, and a spatial resolution ranging from 5.4 to 56 km depending on frequency. On October 4, 2011 AMSR-E stopped functioning after over nine years of successful operations. Sea ice concentration is a Level 3 daily product and is produced using the Enhanced NASA Team (NT2) algorithm [*Markus and Cavalieri,* 2002]. The sea ice concentration is defined as the percentage of a pixel that is covered by sea ice, and the concentration values are mapped onto a 25 km by 25 km polar stereographic grid of the Arctic. Sea Surface Temperatures (SSTs) are classified as the temperature of the top layer of water approximately 1

millimeter thick. AMSR-E measures microwaves in both the horizontal and vertical directions and covers all of the channels of SMMR and SSM/I combined, with also having higher resolution. SSTs are derived from all 10-channel brightness temperatures using the SST algorithm developed by *Wentz and Meissner [2000]* and has a spatial resolution of 56 km. The SSTs are a daily level 3 product and are put on a 0.25° by 0.25° grid. These SSTs are measured in degrees Celsius and have a root mean square error of 0.58°C. SSTs are not produced near coastlines (~75km) or ice edges in order to reduce errors.

4.2.3 ECMWF

The AMSR-E wind speeds are not available over polynyas and hence are not useful for this study. As a result, 10-m wind speeds were obtained from the European Centre for Medium-Range Weather Forecasts (ECMWF) ERA-Interim reanalysis instead (http://data-portal.ecmwf.int/data/d/interim_daily/). The reanalysis combines a first-guess field (based on a 6-hour forecast) as well as in-situ and remote sensing data into an assimilated data set using the 4D-VAR method [*Dee et al*., 2011]. Wind speed data are provided at 6-hour time intervals with a 1.5° by 1.5° spatial resolution.

These data sets were all transposed onto a 25km by 25 km polar stereographic grid in order to simplify the calculations of the moisture flux. Calculations at 25 km resolution indeed require interpolation of Aqua and wind speed data. A horizontal resolution equal to that of the sea ice concentration data is however essential for the moisture flux

calculations, because the spatial variations of the moisture flux are mostly controlled by spatial variations of the surface temperature (which depends above all on the state of the surface: sea ice or open water). The air moisture and wind speed have weaker spatial gradients [*Tisler et al.,* 2008].

4.3 Methodology

4.3.1 Background and Description

The Monin-Obukhov similarity theory, describes a relationship that characterizes the vertical behavior of non-dimensionalized mean flow and the turbulence properties in the surface layer of the atmosphere [*Andreas,* 2002], is used to estimate the turbulent surface fluxes in the atmospheric boundary layer. Since *Monin and Obukhov* [1954], there have been multiple studies done to improve the parameterizations of the roughness lengths used in the calculations of the flux profile relationships [*Dyer and Bradley,* 1982; *Hogstrom,* 1988; *Garratt,* 1992; *Andreas,* 2002] and the stable and unstable stratification algorithms [*Holstag and De Bruin,* 1988; *Beljaars and Holtslag,* 1991; *Dyer and Hicks, 1970; Paulson,* 1970] to better suit the boundary layer. While these improvements have produced more accurate turbulent surface fluxes of the mid-latitudes, they have not significantly improved estimates in the Arctic because they are using nocturnal boundary layer data over land compared to boundary layer data over the sea ice.

The flux profiles depend on whether the boundary layer has a stable or unstable stratification. For unstable stratification the most widely used and accepted flux profile relationships were those proposed by *Businger* [1971] *and Dyer* [1970] [*Dyer & Hicks, 1970; Paulson, 1970; and Businger et al., 1971*]. For stable stratification the flux profile relationships were derived from studies of the nocturnal boundary layer over land, and those produced from *Holtslag and De Bruin* [1988] are most often used. Studies produced by *Forrer and Rotach* [1997], *Klipp and Mahrt* [2004] and *Cheng and Brutsaert* [2005] suggest that in very stable conditions, like those seen frequently over the Arctic sea ice, the flux profile relationships increase more slowly than those from *Holslag and De Bruin* [1988]. There were extensive in situ measurements made over the Arctic sea ice during the Surface Heat Budget of the Arctic Ocean Project (SHEBA) campaign in 1997-1998 and *Grachev et al.* [2007] used these to create a highly accurate flux profile algorithm for stable conditions over the ice. This algorithm better fits the very stable boundary layer conditions in the Arctic and we will use this in our calculations.

Accurate roughness lengths for the wind speed, humidity and temperature profiles over the ice are required to estimate the transfer coefficients used in the equation to calculate the moisture flux [*Andreas et al.,* 2010a]. The roughness lengths are the theoretical height where the logarithmic wind, temperature or humidity profile equals zero and it is a measure of the roughness of the surface. These have often been difficult to estimate and there are large inaccuracies especially over the sea ice. *Andreas et al.* [2010a,b] used roughness lengths measured from the SHEBA campaign to create an algorithm for the roughness length over the Arctic in the winter when the ice is covered with compact, dry snow and in the summer when the ice cover comprises wet snow, melt

ponds and leads. As these are the most accurate estimates made for the Arctic ice in different seasons these roughness lengths will be used in our model.

Since the input parameters from AIRS of the 1000 hPa level vary with height and are not at a standard 2 meter observational height, which is most often used in other bulk aerodynamic flux studies, we have adopted the method of *Launiainen and Vihma* [1990]. This bulk aerodynamic method utilizes the Monin-Obukhov similarity theory and includes an iterative calculation. The iterative calculation method [*Launiainen and Vihma*, 1990] allows for the use of the air temperature and relative humidity at 1000 hPa from AIRS to estimate their corresponding 2m values for use in the calculation of the moisture flux at 2m.

Taking into account the stability and roughness effects on the vertical profiles, the air temperature, relative humidity and wind speed are all stratified onto a reference height, in this case 2m, where the calculations are made. Both the traditional method of *Launiainen and Vihma* [1990] is described below along with our improved choices for the model parameterizations.

4.3.2 The Monin-Obukhov Similarity Theory

The Monin-Obukhov theory gives the non-dimensional profile gradients of wind speed (V), specific humidity (q) and temperature (θ),

$$\frac{\partial V}{\partial z}\frac{kz}{u_*} = \Phi_M(z/L) \qquad (3)$$

$$\frac{\partial q}{\partial z}\frac{z}{q_*} = \Phi_E(z/L) \tag{4}$$

$$\frac{\partial \theta}{\partial z}\frac{z}{\theta_*} = \Phi_H(z/L) \tag{5}$$

where z is the observation height of either humidity, temperature or wind speed, q_*, u_* and θ_*. These are the scaling parameters of velocity, humidity and temperature, respectively.

$$u_* = \left(\frac{\tau}{\rho}\right)^{1/2} \tag{6}$$

$$q_* = -\frac{E}{\rho k u_*} \tag{7}$$

$$\theta_* = -\frac{H}{\rho C_p k u_*} \tag{8}$$

In equations (6-8) ρ is the air density, which depends on the temperature, C_p is the specific heat capacity of air, and the turbulent fluxes of momentum (τ), moisture (E) and sensible heat (H).

Φ_M, Φ_E and Φ_H are the universal functions, which depend on the ratio of z and the Obukhov length (L), and quantify the effects of the surface layer stratification on the profile gradients [*Launiainen and Vihma,* 1990]. The universal functions are integrated with respect to ζ = z/L between the surface and the observation height to give the familiar bulk aerodynamic equations of momentum (9), sensible heat (10) and moisture (11).

$$\tau = \rho u_*^2$$
$$= \rho k^2 \left[\ln\left(\frac{z}{z_0}\right) - \Psi_M(\zeta) + \Psi_M(\zeta_0) \right]^{-2} V_z^2 \quad (9)$$
$$= \rho C_{Dz} V_z^2$$

$$H = \rho C_p k u_* \left[\ln\left(\frac{z}{z_T}\right) - \Psi_H(\zeta) + \Psi_H(\zeta_T) \right]^{-1} (\theta_s - \theta_z)$$
$$= \rho C_p k^2 \left[\ln\left(\frac{z}{z_0}\right) - \Psi_M(\zeta) + \Psi_M(\zeta_0) \right]^{-1} \left[\ln\left(\frac{z}{z_T}\right) - \Psi_H(\zeta) + \Psi_H(\zeta_T) \right]^{-1} (\theta_s - \theta_z) V_z \quad (10)$$
$$= \rho C_p C_{Hz} (\theta_s - \theta_z) V_z$$

$$E = \rho k u_* \left[\ln\left(\frac{z}{z_q}\right) - \Psi_E(\zeta) + \Psi_E(\zeta_{qT}) \right]^{-1} (q_s - q_z)$$
$$= \rho k^2 \left[\ln\left(\frac{z}{z_0}\right) - \Psi_M(\zeta) + \Psi_M(\zeta_0) \right]^{-1} \left[\ln\left(\frac{z}{z_q}\right) - \Psi_M(\zeta) + \Psi_M(\zeta_q) \right]^{-1} (q_s - q_z) V_z \quad (11)$$
$$= \rho C_{Ez} (q_s - q_z) V_z$$

where ζ_0, ζ_T and ζ_q are stability parameters for the observational heights of wind, temperature, and humidity and the integrated universal functions are expressed as Ψ_M, Ψ_H and Ψ_E.

For the stable case $\zeta > 0$, the integrated form for the universal functions is [*Holtslag and de Bruin*, 1988],

$$\Psi_M = \Psi_H = \Psi_E = -0.7\zeta - 0.75\left(\zeta - \frac{5}{0.35}\right)e^{(-0.35\zeta)} - \frac{3.75}{0.35} \quad (12)$$

Andreas [2002] compared different universal functions from several different studies and found that (12) produced the best results in a stable boundary layer.

For the unstable case $\zeta < 0$, the integrated form for the universal functions are [*Paulson*, 1970, *Businger et al.,* 1971 and *Dyer*, 1974],

$$\Psi_M = 2\ln\left(\frac{1+(1-19.3\zeta)^{1/4}}{2}\right) + \ln\left(\frac{1+(1-19.3\zeta)^{1/2}}{2}\right) - 2\arctan((1-19.3\zeta)^{1/4} + \frac{\pi}{2} \quad (13)$$

$$\Psi_E = \Psi_H = 2\ln\left(\frac{1+(1-12\zeta)^{1/2}}{2}\right) \quad (14)$$

These have been proven to provide reasonable estimates for unstable cases [*Andreas*, 2002].

The bulk transfer coefficients C_D, C_H and C_E are expressed as

$$\begin{aligned} C_{Dz} &= C_D(z, z_0, \Psi_M(z/L)) \\ &= \frac{k^2}{[\ln(z/z_0) - \Psi_M(z/L)]^2} \end{aligned} \quad (15)$$

$$\begin{aligned} C_{Hz} &= C_H(z, z_0, z_T, \Psi_M(z/L), \Psi_H(z/L)) \\ &= \frac{k^2}{[\ln(z/z_0) - \Psi_M(z/L)][\ln(z/z_T) - \Psi_H(z/L)]} \end{aligned} \quad (16)$$

$$\begin{aligned} C_{Ez} &= C_E(z, z_0, z_q, \Psi_M(z/L), \Psi_E(z/L)) \\ &= \frac{k^2}{[\ln(z/z_0) - \Psi_M(z/L)][\ln(z/z_q) - \Psi_E(z/L)]} \end{aligned} \quad (17)$$

where z is the measuring height, z_0, z_T, and z_q are the roughness lengths for the wind speed, temperature and water vapor. These bulk transfer coefficients are defined by the roughness lengths in neutral stratification, and by both the roughness lengths and the stability corrections in stable and unstable conditions [*Launiainen and Vihma,* 1994].

L, the Obukhov length, is a parameter characterizing the dynamic, thermal and buoyant processes of the surface layer [*Obukhov*, 1971]. It gives the height at which the turbulence is dominated by buoyant forces rather than wind shear. This way the boundary layer stability is also taken into account in the calculations by using L.

$$L = \frac{-u_*^3 T_0 \rho C_p}{gkH\left(1 + 0.61 T_0 C_p \frac{E}{H}\right)} \qquad \begin{cases} L > 0 & stable \\ L = 0 & neutral \\ L < 0 & unstable \end{cases} \tag{18}$$

In 18, u_* is the friction velocity, T_0 is the mean absolute temperature of the surface layer, ρ is the air density which depends on the temperature, C_p is the specific heat capacity of air, g is the acceleration due to gravity, k is the von Karman constant, E is the moisture flux and H is the sensible heat flux.

The surface roughness length, z_0, is based on an interaction between the wind and wave field. If the surface is water then the roughness length, z_0, depends on C_D [*Large,* 1980], which is dependent on the wind speed. $z_{T,q}$ depends on both the C_D and C_E.

$$\ln(z_0) = \ln(z) - kC_D^{-1/2} \tag{19}$$

where C_D is dependent on the wind at 10 meters: $C_D \times 10^3 = 0.61 + 0.063 V_z$ and C_E depends on C_D: $C_E = 0.63 C_D + 0.32 \times 10^{-3}$

$$\ln(z_T) = \ln(z_q) = \ln(z) - k C_D^{-1/2} C_E^{-1} \quad (20)$$

If the surface is snow/ice then the roughness length (z_0) is calculated by 21, where C_D depends on the snow/ice surface roughness (ξ),

$$C_D \times 10^{-3} = 1.10 + 0.072\xi \quad (21)$$

The Reynolds number (Re) [*Andreas*, 1987] is used to calculate $z_{T,q}$ based on a polynomial that depends on the magnitude of Re for the coefficients and Re itself. Re gives an estimate for how far the roughness elements come above the molecular sublayer [*Andreas et al.,* 2010b]. When Re is small, viscous forces dominate and the flow is smooth and constant. When Re is large, inertial forces dominate and the flow is turbulent and chaotic.

$$\mathrm{Re} = \frac{z_0 u_*}{v} = \frac{z_0 C_D^{1/2} V_z}{v} \quad (22)$$

where v is the kinematic viscosity of air.

$$\ln(z_T) = \ln(z_q) = \ln(z_0) + b_0(\mathrm{Re}) + b_1(\mathrm{Re})\ln(\mathrm{Re}) + b_2(\mathrm{Re})(\ln(\mathrm{Re}))^2 \quad (23)$$

Table 2. Values of the coefficients to use in (23) for estimating the scalar roughness lengths in the three aerodynamic regimes.

Re	b_0	b_1	b_2
Re 0.135 (Smooth)	1.43	0	0
0.135 < Re 2.5 (Transition)	0.25	-0.589	0
2.5 < Re 1000 (Rough)	0.356	-0.538	-0.181

When the flow is classified as smooth, molecular effects control the exchange of both momentum and scalars; when the flow is rough, pressure forces control this exchange [*Andreas, 2002*]. The roughness lengths over snow/ice have been proven very difficult to quantify, but (23) from *Andreas* [1987] have shown success in representing z/z_0 measurements (Figure 19) [*Andreas,* 2002].

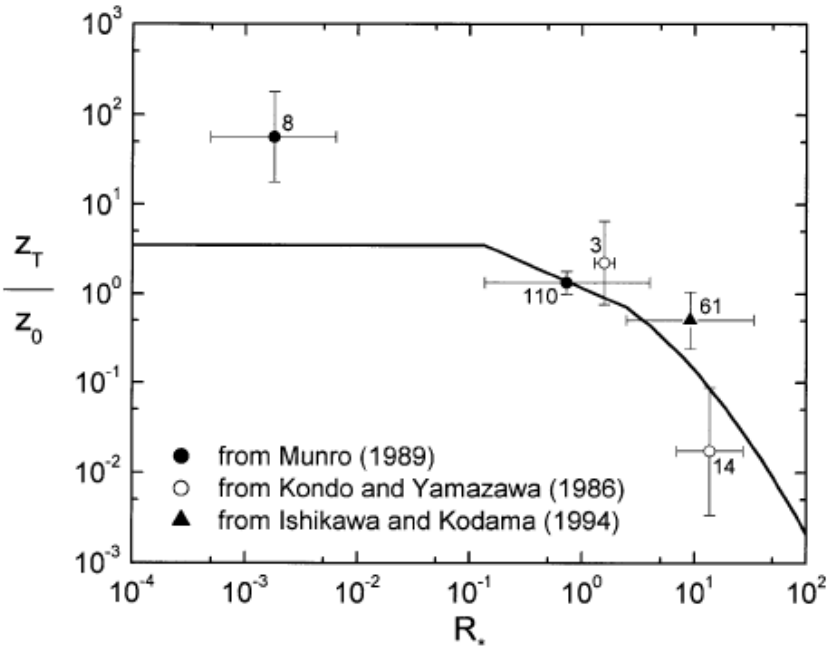

Figure 19. Values of zT/z0 averaged in Re bins for the Munro, Kondo and Yamazawa, and Ishikawa and Kodama datasets. The error bars are one std dev; the number beside each data marker gives the number of individual values used to create the average. The line is the *Andreas* (1987) model. (From *Andreas*, 2002).

After the roughness lengths are estimated, V, q and θ are corrected to the calculation level accounting for the stratification effects.

$$V(z) = f\left[V(z_{10}), z_0, u_*, \Psi_M(z/L), \Psi_M(z_{10}/L)\right] = \frac{u_*}{k}\left[\ln\left(\frac{z}{z_0}\right) - \Psi_M\left(\frac{z}{L}\right) + \Psi_M\left(\frac{z_0}{L}\right)\right] \quad (24)$$

$$\theta(s) - \theta(z) = f\left[\theta(s), \theta(z_{GH}), z_T, \theta_*, \Psi_H(z/L), \Psi_H(z_{GH}/L)\right] = \frac{\theta_*}{k}\left[\ln\left(\frac{z}{z_T}\right) - \Psi_H\left(\frac{z}{L}\right) + \Psi_H\left(\frac{z_T}{L}\right)\right] \quad (25)$$

$$q(s) - q(z) = f\left[q(s), q(z_{GH}), z_q, q_*, \Psi_E(z/L), \Psi_E(z_{GH}/L)\right] = \frac{q_*}{k}\left[\ln\left(\frac{z}{z_q}\right) - \Psi_E\left(\frac{z}{L}\right) + \Psi_E\left(\frac{z_q}{L}\right)\right] \quad (26)$$

The bulk transfer coefficients (15-17), the turbulent fluxes (9-11) and the Obukov length (18) are also calculated. In the first integration, the universal functions are set to zero for the neutral case. The iterative method checks for convergence of L, ensuring that the results are stable. This occurs when successive values of |ζ| are less than 0.1. If this occurs then the calculated turbulent fluxes are taken to be correct; if not then new universal functions (3-5) are calculated, and V, q and θ are corrected to the calculation level. The bulk transfer coefficients, the turbulent fluxes and the Obukhov length are

calculated again. The method is found not to converge if after 25 iterations no stable results are found.

Launiainen and Vihma [1990] have tested their method with in situ data using the eddy correlation method from *Schmitt et at.* [1979] and *Fujitani* [1981] and found that their estimates of heat and moisture flux agreed reasonably well (Figure 20).

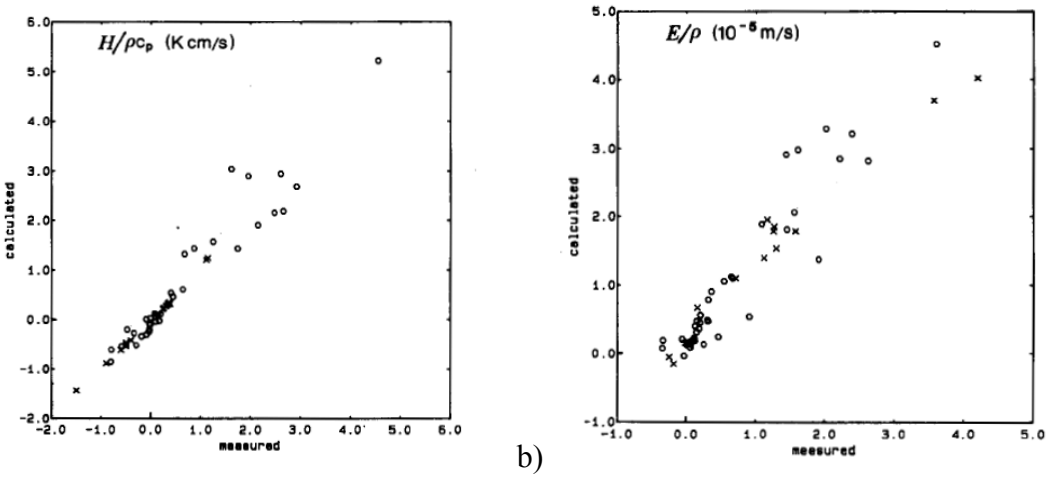

a) b)

Figure 20. Validation tests of the *Launiainen and Vihma* [1990] model (Figures from *Launiainen and Vihma* [1990]).

c) Calculated sensible heat flux ($H/\rho C_p$) verses the one measured using the eddy correlation method (crosses from *Schmitt et at.* [1979] and circles from *Fujitani* [1981]
d) Calculated water vapor flux (E/ρ) verses the measured one (same as above)

4.3.3 The Monin-Obukhov Similarity Theory (updated)

Changes were made to the Monin-Obukhov Similarity Theory in order to improve estimates of the moisture flux in the Arctic. Our updated version of the *Launiainen and Vihma* [1990] model contain different parameterizations for the stable boundary layer case of the integrated universal functions (12-14) and they are taken from *Grachev et al.* [2007].

$$\Psi_M = -\frac{3a_M}{b_M}(x-1) + \frac{a_M B_M}{2b_M}\left[2\ln\left(\frac{x+B_M}{1+B_M}\right) - \ln\left(\frac{x^2 - xB_M + B_M^2}{1 - B_M + B_M^2}\right) + 2\sqrt{3}\left(\arctan\left(\frac{2z - B_M}{\sqrt{3}B_M}\right) - \arctan\left(\frac{2 - B_M}{\sqrt{3}B_M}\right)\right)\right] \tag{27}$$

where $x = (1+\zeta)^{1/3}$, $B_M = \left(\frac{1-b_M}{b_M}\right)^{1/3} > 0$, $a_M = 5$ and $b_M = 5/6.5$, and

$$\Psi_H = \Psi_E = -\frac{b_E}{2}\ln(1 + c_E\zeta + \zeta^2) + \left(-\frac{a_E}{B_E} + \frac{b_E c_E}{2B_E}\right) \times \left(\ln\left(\frac{2\zeta + c_E - B_E}{2\zeta + c_E + B_E}\right) - \ln\left(\frac{c_E - B_E}{c_E + B_E}\right)\right) \tag{28}$$

where $B_E = \sqrt{c_E^2 - 4} = \sqrt{5}$, $a_E = 5$, $b_E = 5$, and $c_E = 3$. These are only valid if $\mathrm{Ri_B} < \mathrm{Ri_{Bcrit}} \approx 0.2$, where $\mathrm{Ri_B}$ (29) is the bulk Richardson number that is calculated from (24-26).

$$Ri_B = -\left(\frac{gz}{\theta_v}\right)\left(\frac{\Delta\theta + 0.61\theta_v\Delta q}{V_z^2}\right) \tag{29}$$

Andreas [2005] requires different polynomial coefficients for z_T and z_q because the molecular diffusivity of heat in air is less than the molecular diffusivity of water vapor in air. Thus these new coefficients in Tables 3 & 4 should be used.

Table 3. Polynomial coefficients for calculating z_T

Re	$\mathbf{b_0}$	$\mathbf{b_1}$	$\mathbf{b_2}$
Re ≤ 0.135 (Smooth)	1.25	0	0
0.135 < Re ≤ 2.5 (Transition)	0.149	-0.550	0
2.5 < Re ≤ 1000 (Rough)	0.317	-0.565	-0.183

Table 4. Polynomial coefficients for calculating z_q

Re	$\mathbf{b_0}$	$\mathbf{b_1}$	$\mathbf{b_2}$
Re ≤ 0.135 (Smooth)	1.610	0	0
0.135 < Re ≤ 2.5 (Transition)	0.351	-0.628	0
2.5 < Re ≤ 1000 (Rough)	0.396	-0.512	-0.180

In the summer, the sea ice is covered with melt ponds and leads that enhance the turbulent momentum transfer at the surface [*Andreas et al.,* 2010a]. The edges of the marginal ice create vertical surfaces that the winds come into contact with. Thus C_D, which is used to calculate the initial z_0, differs from (19). *Andreas et al.* [2010a] found C_D to be a function of the ice concentration (ci).

$$C_D \times 10^{-3} = 1.5 + 2.233ci - 2.333ci^2 \tag{30}$$

This is a parabolic function because when there are no vertical surfaces (100% ice concentration) C_D is small. C_D increases to a maximum when there is a medium amount of melt ponds, leads and ice edges creating multiple vertical surfaces. As the ice concentration approaches zero, the water features in the ice are so closely packed that

some of the vertical surfaces are shielded and C_D decreases again [*Andreas et al.,* 2010a]. When calculating E, *Andreas et al.* [2010a] use a combination of E from the ice surface and the ocean surface using the ice concentration.

$$E = \rho C_{Ez} S_r [(ciq_{s,i} + (1 - ci)q_{s,w}) - q_z] \tag{31}$$

Where the effective wind speed (S_r) includes a parameter for gustiness. In stable conditions.

$$S_r = V_z + 0.5 \sec h(V_z) \tag{32}$$

For unstable conditions, S_r includes a term for turbulent exchange that is enhanced when conditions are unstable

$$S_r = (V_z^2 + \beta_g^2 w_*^2)^{1/2} \tag{33}$$

In 32 and 33, $w_* = u_* \left(-\frac{600}{kL} \right)^{1/3}$, is the convective velocity scale and $\beta_g = 1.25$ [*Fairall et al.,* 1996]. By using the effective wind speed we prevent the transfer coefficients from approaching infinity when the wind speed approaches zero [*Andreas et al,* 2010b].

In the winter, the sea ice pack is compact and covered with snow and thus requires a different parameterization than in the summer. *Andreas et al.,* [2010b] found, using in situ data taken from the SHEBA campaign, that over the wintertime ice z_0, should be calculated from

$$z_0 = 0.135 \frac{v}{u_*} + 2.30 \times 10^{-4} \tanh^3(13 u_*) \tag{34}$$

The first term accounts for the smooth flow and the second term accounts for the rough flow over the ice/snow. The roughness length plateaus with increasing u_* [*Andreas et al.,* 2010b]. z_0 was calculated from the SHEBA data over the Arctic ice in the winter, thus

being more accurate than our previous parameterizations. The moisture flux is calculated via (31).

Chapter 5: Case Study: Moisture flux from the North Water Polynya

5.1 Background

5.1.1 General Characteristics

Polynyas provide ideal locations where the moisture flux can be estimated for accuracy. Polynyas are small-scale areas of the Arctic ice pack where effects of the moisture flux are seen over both ice and water. A polynya is a persistent opening or reduced cover in sea ice that occurs in locations or at climatological times when ice is otherwise normally present. Polynyas are present in both the Arctic and Antarctic, and some recur in the same location at roughly the same time each year [*Stringer and Groves*, 1991]. Polynyas can range in size from hundreds to thousands of square kilometers [*Smith et al*., 1990]. Polynyas form via two different mechanisms and are classified as such: sensible heat and latent heat (Figure 19) [*Smith et al.*, 1990]. Sensible heat polynyas most often occur within the sea ice pack and form when cold dense water sinks and is replaced by warmer water, which melts the sea ice. Sensible heat from the warm ocean water is what is used to melt the sea ice and create the polynya. Latent heat polynynas, on the other hand, almost always form along coasts. Winds push the sea ice away from the coast and

new ice is continually forming in place. The newly formed ice from the seawater releases latent heat because a change of state occurred, but there is no change in temperature.

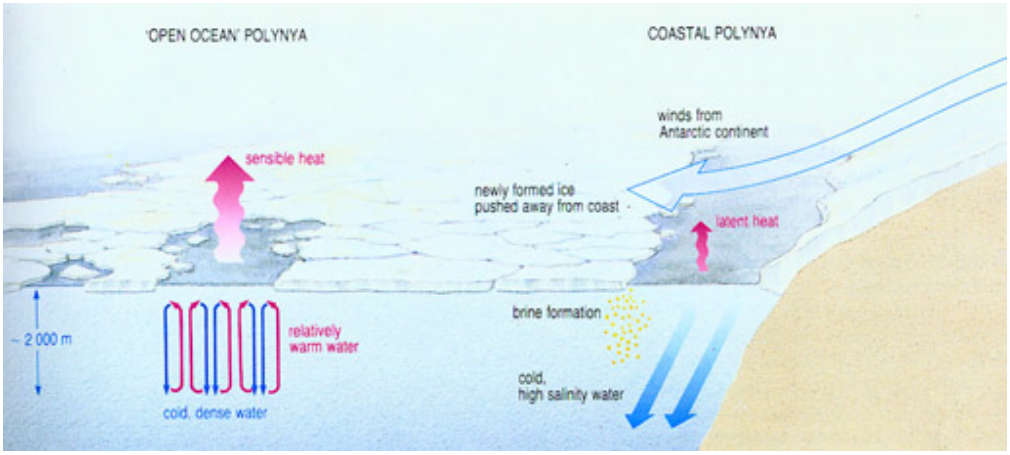

Figure 19. Diagram of sensible heat (open ocean) and latent heat (coastal) polynya formation. Image from *Ocean Circulation, 2nd Edition* by Open University, Butterworth-Heinemann Publishers, page 219.

Even though their size is relatively small in comparison to the sea ice area, polynyas have a large impact on the Arctic climate system in a number of ways. Polynyas affect the surrounding atmosphere, the heat budget, the radiation budget, the ocean salinity and circulation, and biological activity. Sea ice cover is a very good insulator between the ocean and atmosphere, allowing little exchange of energy and because of this it acts as a stable boundary layer inhibiting the transport of heat and moisture into the atmosphere [*Walter*, 1989; *Massom et al*., 1998]. When a polynya forms, the relatively warm, humid ocean surface is exposed to the overlying cold, dry air and these temperature differences, sometimes as much as 20 K, create an unstable boundary layer that allows for large exchanges of heat and moisture between the two [*Minnett & Key*, 2007]. Large temperature differences between the ocean and atmosphere can also increase the surface

heat flux. The heat flux from polynyas (100-300 W/m^2) is often two times the magnitude of the heat flux over ice (15-20 W/m^2), and can affect the heat budget by 20-30% [*Smith et al.*, 1990; *Maykut*, 1978]. Sensible and latent heat fluxes have been calculated for polynyas in numerous studies [*Badgely, 1966; Pease, 1987; Andreas, 1979; den Hartog, 1983; Launiainen and Vihma, 1994; and Maykut, 1982*]. The excess heat and moisture loss cools the ocean and heats up the surrounding boundary layer above and downwind of the polynya and can modify mesoscale atmospheric motions [*Renfrew*, 2002; *Dethleff,* 1994]. Such large exchange of moisture leaves the ocean surface, quickly cools and condenses, and if the boundary layer is unstable, creates plume clouds (Figure 20), which can be transported downstream via winds [*Minnett and Key*, 2007]. These plumes have also been known to precipitate and can affect the local climate. Plume clouds do not always form downwind of a polynya because there must be enough moist potential energy available at the surface for these clouds to become buoyant, but most often a steam fog forms over the polynya when the air masses come into contact [*Pinto and Curry*, 1995]. *Mailhot et al.* [2002] studied plume cloud formation over a polynya using both aircraft observations and the Canadian Compressible Community Model. In one of their sensitivity studies, they found that when they did not allow for the exchange of moisture between the ocean and atmosphere and thus prevented the enhanced moisture flux from the polynya, the relative humidity did not increase to saturation and clouds did not form. Thus, they concluded that the moisture flux from polynyas plays a crucial role in creating clouds.

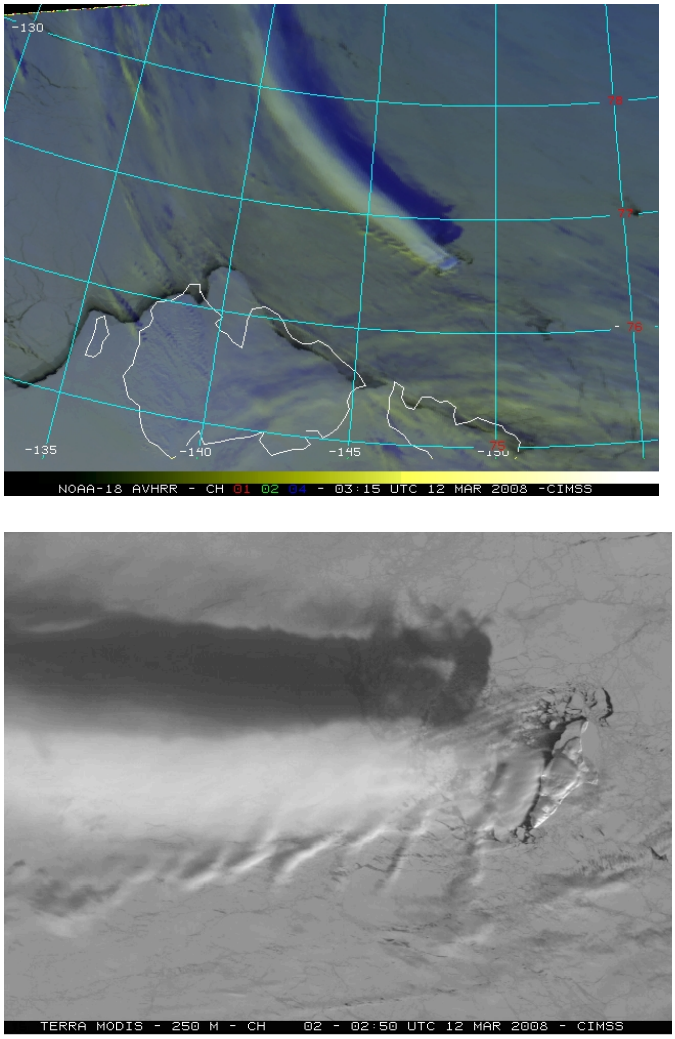

Figure 20. (top) A false color RGB image derived from 1-km resolution NOAA-18 AVHRR data shows a long narrow cloud plume streaming northwestward from the Bennett Island polynya on March 12, 2008. (bottom) A 250m resolution Terra MODIS visible image shows a closer view of the Bennett Island polynya and its cloud plume on March 12, 2008. Images from Cooperative Institute for Meteorological Satellite Studies website (http://cimss.ssec.wisc.edu/goes/blog/archives/622).

Polynyas also have an effect on the radiation budget because of their much lower albedo than sea ice or snow. Open water absorbs more incoming radiation than sea ice, causing more melting, more open water, and more absorbed radiation [*Andreas and Ackley*, 1982]. Polynya induced clouds and plumes can modify the surface radiation budget downwind, increasing the downwelling longwave radiation thus reducing the

cooling of the surface by as much as 44% [*Pinto and Curry*, 1995; *Pinto et al*., 1995]. These increases could cause a positive radiative feedback, which could enhance ice melt near polynyas, enhancing the moisture flux, and clouds, which cause greater ice melt [*Minnett & Key*, 2007]. Moisture flux, and thus convection, from polynyas can impact the regional climate with changes in atmospheric and surface energy budgets [*Schnell et al*., 1989].

Polynyas can also affect ocean salinity and circulation. Within latent heat polynyas, the freezing of new ice causes brine rejection into the surrounding waters. This excess salinity increases the density of the water, causing it to sink and to be replaced by less dense, less saline waters [*Markus et al.*, 1998]. This is one of the ways that Antarctic Bottom Water is created and one of the driving factors keeping the world's ocean circulation in motion. Finally, polynyas are also important for Arctic wildlife. These openings in the ice provide places for mammals and migratory birds to hunt, breed, and to inhabit [*Stirling*, 1980].

5.1.2 The North Water Polynya

The North Water polynya, which is the Northern Hemisphere's largest recurring polynya, forms in northern Baffin Bay in an area called the Smith Sound, located between Ellesmere Island on the west and Greenland on the east [*Topham*, 1983]. This is a predominantly latent heat polynya, which forms in response to an ice dam in Smith Sound that blocks ice from moving into Baffin Bay [*Ito and Muller*, 1977]. This ice is continuously forced southward by persistent northerly winds that channel through the

steep-sided valleys in the sound [*Ito*, 1985] and by southward ocean currents flowing sometimes at a rate as high as 600 km^3 day^{-1} [*Ito,* 1982]. The North Water polynya is also a sensible heat polynya where oceanic upwelling results in ice melt and thinner ice [*Morales Mequeda et al.,* 2004]. This polynya has ice concentrations of 60-80% in the winter months, with the ice being young, thin and thin/medium first-year ice [*Barber et al.,* 2001a; *Gloersen et al.,* 1992]. These features, along with synoptic conditions, cause the North Water polynya to open and close in a rhythmic fashion for all but the summer months when the region is ice-free [*Morales Maqueda et al.,* 2004]. The southern extent, and thus the overall size of this polynya, changes with each event due to variable weather conditions [*Stirling*, 1980]. *Barber et al.* [2001b] examined the North Water polynya for the period 1979-1996 and found that the frequency of the polynya events increased over that period with the continued reduction in the central Arctic ice coverage. The North Water polynya is an ideal location to study the moisture flux because there has been evidence of large turbulent exchanges at least an order of magnitude larger than the exchange over the sea ice [*Maykut,* 1978] and there is often a downwind fetch that can exceed 100 km [*Smith et al.*, 1990].

5.2 Calculation of the Moisture Flux over the North Water Polynya 2003-2009

We begin with a small-scale, pilot study in preparation for large-scale flux calculations over the entire Arctic region. The small-scale study calculates moisture fluxes from the North Water polynya and checks the accuracy of the satellite data.

The moisture flux is calculated at the North Water polynya for a series of events during the 2003-2009 period (Figure 21) using the input parameters classified in Table 5. We calculate the moisture fluxes over the North Water polynya using the *Launiainen and Vihma* [1990] model.

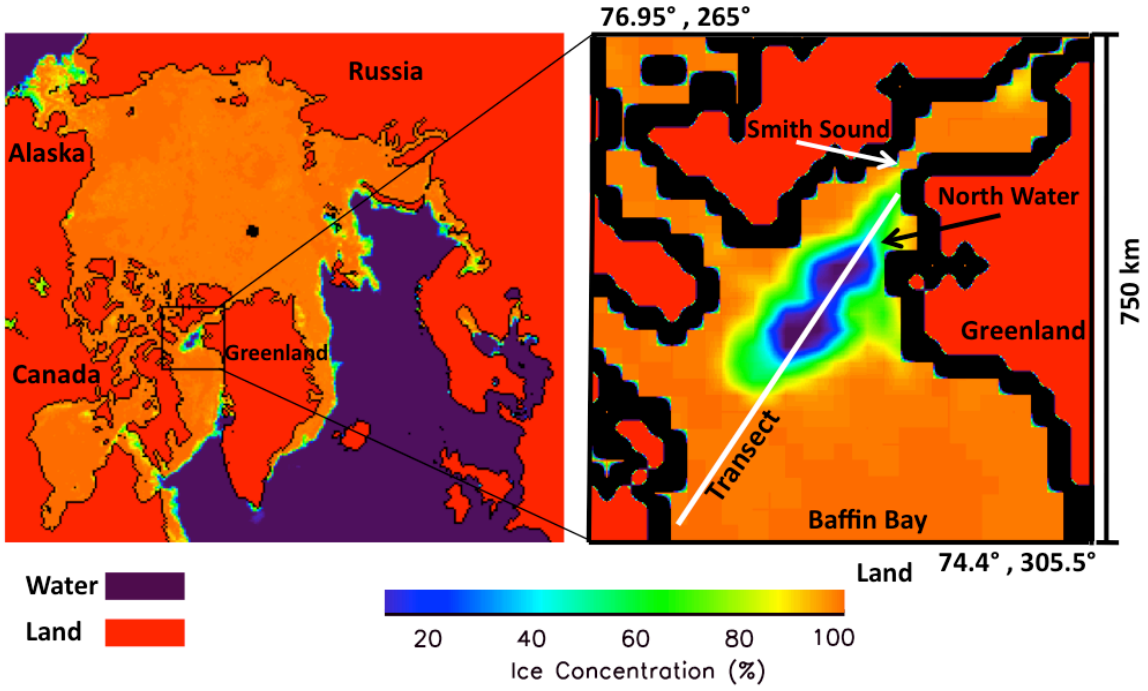

Figure 21. Maps of the Arctic region (left) and the North Water polynya study area (right). Red signifies land, the white line is the transect line used in this study, and all other colors correspond to ice concentration (%). The figure on the right shows an area of 562,500 km^2.

Table 5. Classifications of input data

Input Parameters	**Symbol**	**Source**	**Level**
Surface Skin Temperature (C)	Ts	AIRS	Surface
Air Temperature (C)	Ta	AIRS	1000 hPa
Relative Humidity (%)	RH	AIRS	1000 hPa
Geopotential Height (m)	GH	AIRS	1000 hPa
Wind Speed (m/s)	V	ECMWF	10 m
Sea Surface Temperature (C)	SST	AMSR-E	Surface
Ice Concentration (%)	Ci	AMSR-E	Surface
Snow/ice surface roughness (cm)	ξ = 20 cm for MY ice ξ = 10 cm for FY ice	Kwok et al., 2004	Surface

This calculation is carried out by first converting the surface temperature (T_s) or sea surface temperature (SST), depending on whether the surface is water or ice, and converting air (T_a) temperatures to the potential temperatures θ_s and θ_a, and the average temperature θ_{mn}.

$$\theta_s = T_s + 273.15 + 0.01(0) \tag{36}$$

$$\theta_a = T_a + 273.15 + 0.01(GH) \tag{37}$$

$$\theta_{mn} = \frac{\theta_s + \theta_a}{2} \tag{38}$$

Then ρ is calculated, which varies with θ_{mn}.

$$\rho = 349/\theta_{mn} \tag{39}$$

The specific humidities at the 1000 hPa level (q_z) and at the surface (q_s) are calculated from e_a and e_s.

$$q = \frac{0.622e}{1013 - 0.378e} \tag{40}$$

where e_a is computed from the saturation pressure at θ_a and the relative humidity at 1000 hPa (RH).

$$e_a = \varepsilon(\theta_a) \times RH/100 \quad (41)$$

The saturation pressure e_s is calculated for θ_s.

$$e_s = \varepsilon(\theta_s). \quad (42)$$

Here ε is the saturation pressure of water vapor.

$$\varepsilon = e^{\left(\frac{-6763.6}{\theta} - 4.9283\ln(\theta) + 54.23\right)} \quad \text{for } \theta > 273.15 \quad (43)$$

$$\varepsilon = e^{\left(\frac{6141}{\theta} + 24.3\right)} \quad \text{for } \theta < 273.15 \quad (44)$$

The same steps are taken to calculate the moisture flux that are described in section 4.3.2.

5.3 Error Estimates for the North Water Polynya

Errors in the moisture flux calculations arise from uncertainties in the input parameters, specifically the surface temperature, air temperature, relative humidity, wind speed and geopotential height. We incorporate typical uncertainties for each of the input parameters in Table 5. The surface and air temperature data sets from AIRS include error estimates [*Susskind and Blaisdell,* 2010], which we applied to calculate the average moisture flux errors for each polynya event. The AIRS error estimates are based on 16 different internal convergence tests, the values of which are multiplied by a matrix that

differs for non-frozen ocean and land/ice cases. The coefficients for these matrices were created using AIRS retrievals and ECMWF 3-hour forecasts on September 24, 2004 [*Susskind and Blaisdell,* 2010]. The relative humidity data set from AIRS did not include any error estimate, but the relative humidity data have been shown to have a 20% error [*Tobin et al.,* 2006, *Gettelman et al.,* 2006]. The relative humidity uncertainty estimates are representative of this region. *Tobin et al*. [2006] used humidity profiles taken from three Atmospheric Radiation Measurement (ARM) program sites that Aqua overflew. One of these sites was in North Slope of Barrow, Alaska; although the site is not on the sea ice, it is along the coast of the Arctic Ocean. The average geopotential height error is calculated from the AIRS data. Estimating uncertainties for the ECMWF wind speed has proven challenging because errors have not been accurately determined at this time for the Arctic. Following *Lupkes et al.* [2010] we assume an estimated uncertainty of 0.6 m/s for wind speeds for this study. SSTs from AMSR-E have an error of 0.58°C (*Wentz and Meissner,* 2000). When SST data are not available (near coastlines or ice edges), SSTs are set to -1.8°C and have an error of 0.2°C. The accuracy of the water vapor transfer coefficient C_E over the open sea is probably no better than ±20% [*Cronin et al*., 2006]. AIRS temperature and humidity profiles are created from different wavelengths. The temperature profile uses channels in the CO_2 Q branch, which occurs at 667 cm^{-1} because it is sensitive to temperature variations at altitudes up to 1 hPa pressure level. 147 channels in this branch are used in the first estimation of the temperature profile. The humidity profile is created using channels on the peaks of some of the strongest absorption features in the 6.7 μm water vapor band. The temperature profile is then updated using 7 out of the 66 channels that the humidity profile uses to produce more accurate estimates.

Hence AIRS temperature and humidity are almost independent of each other. We assumed that the variables were uncorrelated and this allows us to make an error estimate.

$$\sigma_E^2 = \sum \sigma_x^2 \left(\frac{\partial E}{\partial x} \right)^2 \tag{45}$$

where the derivative of the moisture flux with respect to each variable (dE/dx) is computed, squared and multiplied by the square of the error attributed to that variable. These are summed up for each variable, and the square root of the sum is the error estimate for the moisture flux. The largest uncertainties will arise from the uncertainty in the air temperature, with smaller contributions to the uncertainty due to the relative humidity, the geopotential height, the surface temperature, and the wind speed.

Another large source of error will come from the surface temperature of the ice. The sensors have a hard time distinguishing between the clouds and the ice surface because they are both very cold, whereas other surfaces such as the tropical ocean would be much warmer than the cloud top, so that the sensor could tell the two apart. The algorithm or cloud detection tests might not detect clouds over the ice and will give back an erroneous ice surface temperature, which is really the cloud top temperature. Ice surface temperature will have larger errors than over other surfaces at lower latitudes. This error would most likely affect the accuracy of the surface specific humidity over the ice, which is calculated via the surface temperature. Another source of error could arise from the coarse vertical resolution of the AIRS instrument. The geopotential heights of the 1000 hPa surface can at time be almost 100 meters and this could produce errors in our calculations.

The error estimates were calculated via equation 45 for the input parameters and the errors and results are shown in Table 6.

Table 6. Sensitivity of the ocean-atmosphere moisture flux to different input uncertainties.

Variable (x)	**$d\rho/dx$**	**σ_x**	**$\sigma_x\, d\rho/dx$**
T_a (K)	2.77×10^{-3}	3.81	1.06×10^{-2}
T_s (K) (65%) *	2.77×10^{-3}	3.80	1.05×10^{-2}
SST (K) (35%) *	2.77×10^{-3}	0.2	5.54×10^{-4}
GH (m)	2.77×10^{-5}	4.45	1.23×10^{-4}
Variable (x)	**dq_s/dx**	**σ_x**	**$\sigma_x\, dq_s/dx$**
T_s (K) (65%)	1.97×10^{-3}	3.80	7.49×10^{-3}
SST (K) (35%)	1.97×10^{-3}	0.2	3.94×10^{-4}
Variable (x)	**dq_a/dx**	**σ_x**	**$\sigma_x\, dq_a/dx$**
T_a (K)	1.75×10^{-3}	3.81	6.67×10^{-3}
RH (%)	2.42×10^{-2}	0.2	4.84×10^{-3}

Variable (x)	**dE/dx**	**σ_x**	**$\sigma_x\, dE/dx$**
P (kg m^{-3})	1.76×10^{-5}	1.17	2.06×10^{-5}
C_E	2.07×10^{-2}	1.6×10^{-3}	8.28×10^{-6}
U (m s^{-1})	5.64×10^{-6}	0.6	3.38×10^{-6}
q_s (g kg^{-1})	6.28×10^{-3}	0.52	3.27×10^{-3}
q_a (g kg^{-1})	6.28×10^{-3}	0.71	4.46×10^{-3}
σ_E (g m^{-2} s^{-1})	5.56×10^{-3}		
<E> (g m^{-2} s^{-1})	2.30×10^{-2}		

* The surface temperature errors the average ice concentration to utilize the errors of both the surface temperature from AIRS and the SSTs.

Using this method, the uncertainty of the moisture flux, averaged over all polynya events, was calculated to be 5.56×10^{-3} g m^{-2} s^{-1}. Compared to the average moisture flux of 2.30×10^{-2} g m^{-2} s^{-1}, this amounts to a relative error of 25%. This is a small error compared to the range of moisture fluxes between the polynya events.

5.4 Comparisons of the North Water Polynya study with similar studies and ECMWF

We compared our results with other moisture flux estimates using in situ data during the 2003-2009 time period. This is done for the North Water Polynya with the results of *Raddatz et al.* [2010].

There were no field campaigns during the 2003-2009 study period for the North Water polynya, but during January – June 2008 there was a field campaign and study done of Canada's Cape Bathurst flaw-lead/polynya region. *Raddatz et al.* [2010] used hourly microwave radiometric profiles of absolute humidity and temperature taken aboard an icebreaker to study the atmospheric boundary layer. They used these observations to calculate the moisture flux from the surface in the winter, which they classified as January 1 – March 31. During this period they calculated moisture fluxes ranging from 3.01×10^{-4} g m^{-2} s^{-1} to 3.60×10^{-3} g m^{-2} s^{-1}. We used AIRS data from January 1 – March 31 for this region to calculate the moisture flux using the same method described previously and we obtained values of 1.46×10^{-7} g m^{-2} s^{-1} to 3.66×10^{-3} $gm^{-2}s^{-1}$. Their measurements were made at a single point over the polynya, whereas ours were computed on a 25 by 25 km grid, which occasionally also included sea ice. This explains our much smaller minimum moisture flux. The fact that our calculated maximum values fit so well with those from *Raddatz et al.* [2010] is very encouraging.

We further compared our results with those from the 0.73° by 0.73° ECMWF ERA-Interim full resolution reanalysis data sets for the January 2003 event (http://data-

portal.ecmwf.int/data/d/interim_full_daily/). AIRS humidity data over the open ocean, including polynyas, if large enough to be resolved by the model grid, have been assimilated to ERA-Interim only since April 2003, but only under clear-sky conditions [*Dee et al.,* 2011]. Further, the effect on the analysis is small: the down-weighting of the AIRS data is coupled with the fact that the ERA-Interim humidity analysis is highly constrained by other satellite observing systems [*McNally et al.,* 2006]. The specific humidity for AIRS was compared with the specific humidity from ERA-Interim (Figure 22). These were calculated from AIRS relative humidity and air temperature and from ERA-Interim dew point and air temperatures. The specific humidity of AIRS was larger than that of ERA-Interim on most of the days. Specifically, on days 2-6 Figure 22 shows clearly identifiable differences even quite far from the North Water polynya. On days 3-6 the absolute difference is up to 1 g kg^{-1} over the polynya region, which corresponds to a relative difference of about 100%. The average specific humidity over the polynya for AIRS was 0.56 g kg^{-1} and for ERA-Interim was 0.47 g kg^{-1} over the 11-day period.

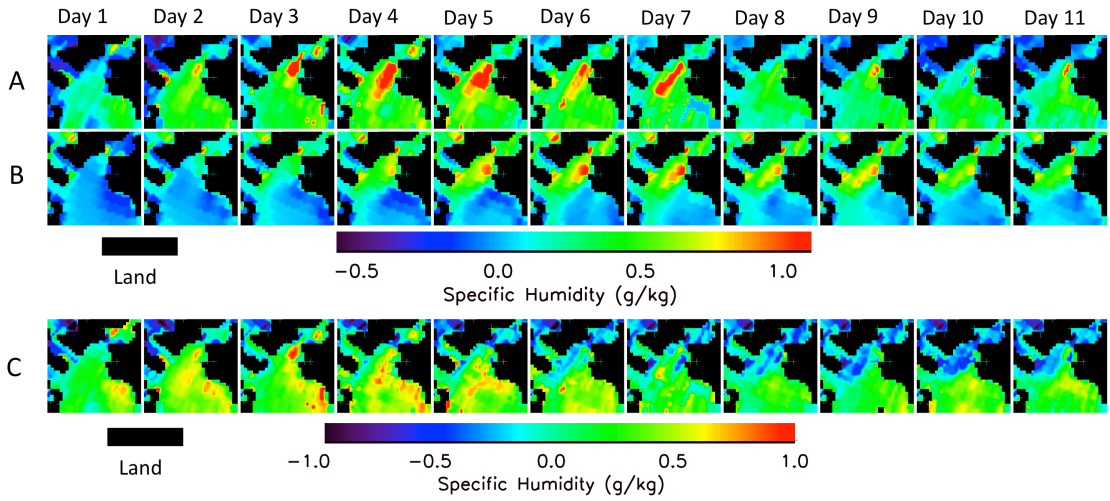

Figure 22. Comparison of AIRS and full resolution ECMWF specific humidity (g kg^{-1}) for

the 2003 polynya event (1/9/2003 – 1/19/2003). A) AIRS specific humidity, B) ECMWF specific humidity, C) Difference between AIRS specific humidity and ECMWF specific humidity. Land is black.

The ice concentration from AMSR-E was compared with that of ERA-Interim for the 2003 polynya (Figure 23). Due to its coarse resolution (1.5° x 1.5°), the ERA-Interim sea ice concentration is less accurate than that of AMSR-E (25km x 25km). The ERA-Interim ice concentrations are lower in the vicinity of the North Water polynya on days 4-6, but it appears that this area of lower ice concentration does not fluctuate throughout the event, having an average of 62% ice concentration. The AMSR-E ice concentration for the polynya ranges from 56-77%. This can be seen in Figure 21c where there are large ice concentration differences. The ice concentration is very similar over the thick ice pack, but there are many discrepancies over the polynya. For ERA-Interim, the ice concentration starts out too low, before the polynya is even open, and then does not reduce its size in day 8-9 when the polynya is actually much smaller. The polynya produced by ERA-Interim ice concentration data is much larger than what is produced by AMSR-E, which can create problems in computing the moisture flux.

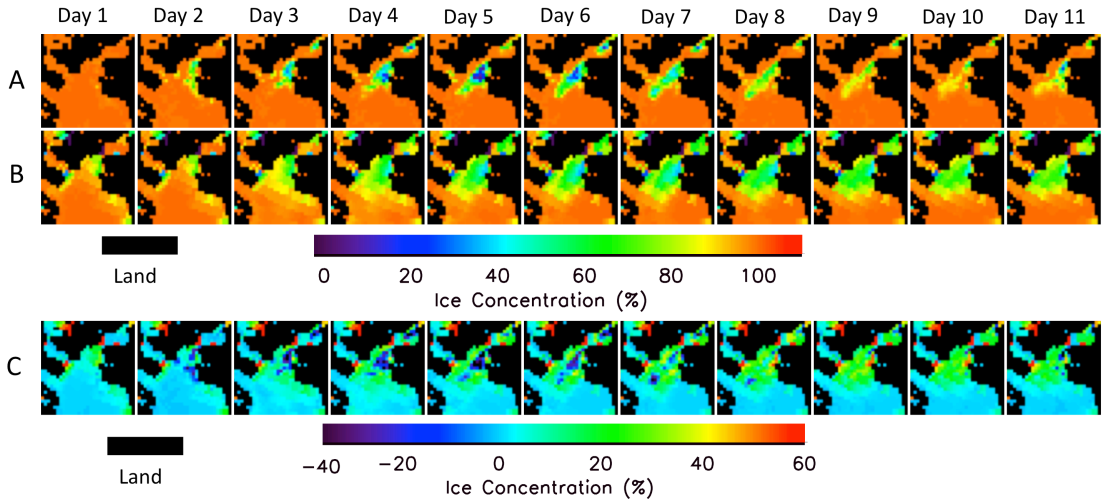

Figure 23**.** Comparison of AMSR-E and full resolution ECMWF ice concentration (%) for the2003 polynya event. A) AMSR-E ice concentration, B) ECMWF ice concentration, C) Difference between AMSR-E and ECMWF ice concentrations. Land is black.

The ERA-Interim data for air temperature, surface temperature, dew point temperature, wind speed and ice concentration are used along with the method described in the text to calculate the moisture flux. Due to the large inaccuracies with the ERA-Interim ice concentration for the North Water polynya, result in moisture flux estimates with some errors. This can be seen in Figure 24 where AIRS and ECMWF moisture fluxes are compared for the 2003 polynya. The moisture flux of AIRS follows the normal pattern of the North Water polynya, in which size and moisture fluctuates throughout the event. The moisture flux for ECMWF starts out small, but from day 4 onward the area with a large flux remains constant and too large; also the maximum values are occasionally too large. The specific humidity was less for ERA-Interim and the erroneous ice concentration causes the moisture flux over the polynya to be an average of 4.90 x 10^{-3} g m^{-2} s^{-1} smaller than that for AIRS. AIRS had an average moisture flux over the polynya that was 16%

larger than ERA-Interim, which had an average of 2.52 x 10^{-2} g m^{-2} s^{-1}. When comparing the moisture flux over the entire study region, ERA-Interim does in fact have a larger moisture flux, but this is due to the ice concentration. The moisture flux appears to be more reliable from AIRS because of the more accurate ice concentrations. This supports the idea that the AIRS instrument can accurately capture even smaller features in the Arctic sea ice pack.

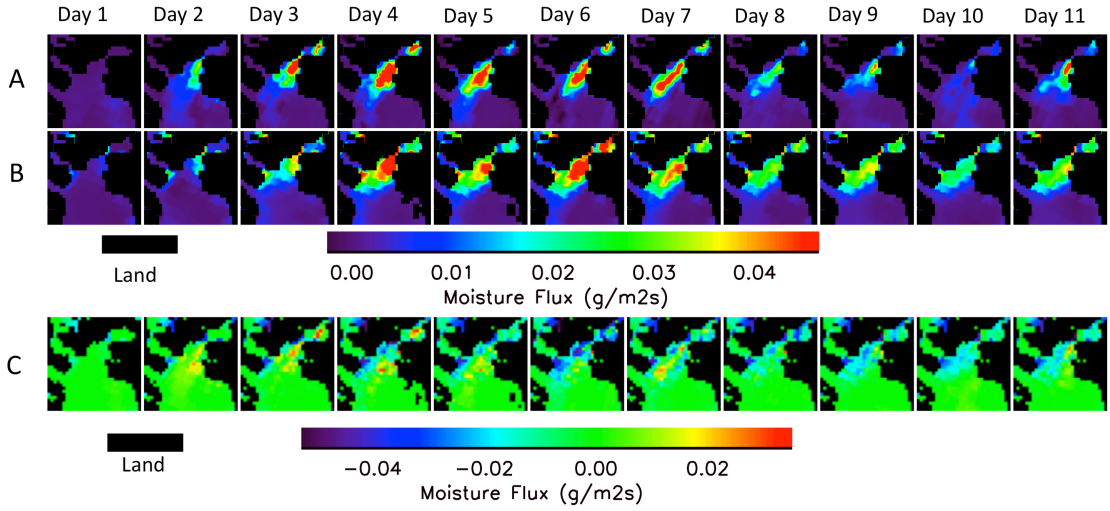

Figure 24. Comparison of AIRS moisture fluxes with full resolution ECMWF moisture fluxes for the 2003 North Water polynya event. A.) Calculated AIRS moisture flux (g m^{-2} s^{-1}), B.) Calculated ECMWF moisture flux (g m^{-2} s^{-1}), C.) Difference between the AIRS and the ECMWF moisture flux (g m^{-2} s^{-1}). Black is land.

Finally, the AIRS moisture flux was compared with the full resolution moisture flux product that is produced by ERA-Interim for the 2003 polynya event (Figure 25). In this figure, the ERA-Interim moisture flux follows the pattern of AIRS more closely than what we produced using the variables from ERA-Interim, but the polynya area is often too large and the magnitude of the moisture flux over the polynya is too small in the ERA-

Interim product. The average area of the polynya produced by ERA-Interim is 70% larger than that produced by AMSR-E, owing to the larger moisture flux over the entire study region. The average moisture flux over the polynya produced by ERA-Interim is 1.46 x 10^{-2} g m^{-2} s^{-1}, which is 51% smaller than our AIRS moisture flux over the polynya. The ERA-Interim magnitude is not large enough over the polynya, but over the solid ice pack the moisture fluxes are nearly identical. Possible reasons for these differences are due to the relatively poor quality of ERA-Interim ice concentration over the polynya and differing moisture flux algorithms. However when the average moisture flux over the entire study area is compared, the ERA-Interim moisture flux product is 11% larger in magnitude than that for AIRS. The average moisture flux over the entire region for ERA-Interim is 4.92 x 10^{-3} g m^{-2} s^{-2} and for AIRS is 4.48 x 10^{-3} g m^{-2} s^{-1}. The reason for this is that the ERA-Interim ice concentration for the polynya is larger in area, creating a larger area of elevated moisture flux.

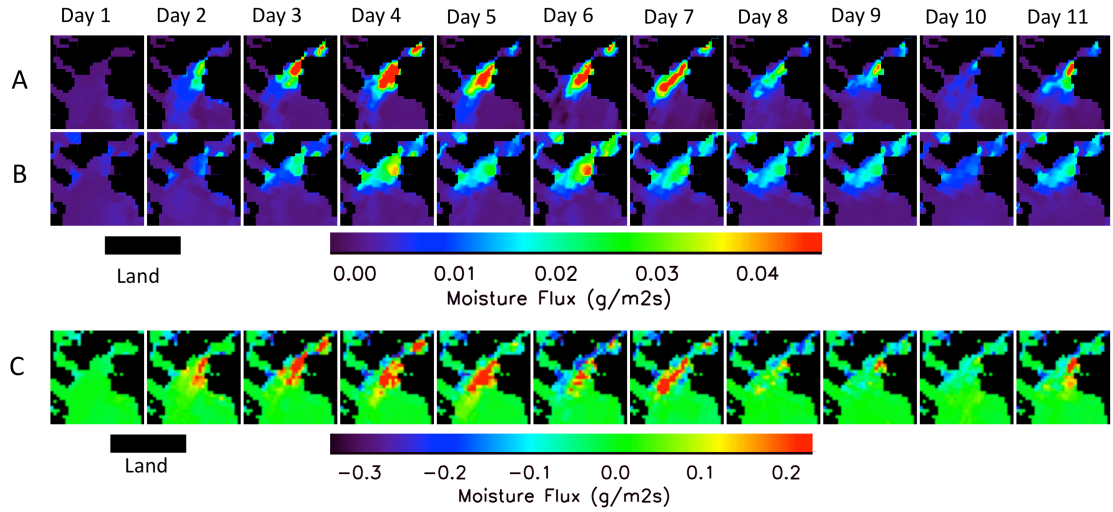

Figure 25. Comparison of AIRS moisture fluxes with full resolution ECMWF moisture fluxes for the 2003 North Water polynya event. A.) Calculated AIRS moisture flux (g m^{-2}

s^{-1}) using the Monin-Obukhov similarity theory, B.) ECMWF moisture flux (g m^{-2} s^{-1}), C.) Difference between the AIRS and the ECMWF moisture flux (g m^{-2} s^{-1}). Black is land.

To further validate our moisture flux estimates we compared our results to other studies of polynyas and leads in the Arctic and Antarctic. The moisture flux from each individual polynya event depends on the unique meteorological conditions at the specific time and location, but we expect some general consistency among the observations. Moisture fluxes from 13 studies are listed in Table 7. These 13 studies span the Arctic and Antarctic, leads and polynyas, in situ and model data, and cover years from the 1970's to the 1990's. Values of the moisture fluxes for our study fall within the values from the other studies listed in the table. The 2004 polynya had a very similar computed moisture flux to those from the Weddell Sea [*Launianen and Vihma*, 1994] and the Mertz Island Glacier [*Roberts et al.,* 2001], with 2.74 x 10^{-2} g s^{-1} compared to 2.72 x 10^{-2} g s^{-1}. The Northeast Water Polynya in the *Willmott et al.* [1997] study had an area of 4,200 km^2, which most closely resembled the 2005 North Water Polynya of 5,555 km^2. The comparisons for the magnitude of the moisture fluxes were 4.86 x 10^7 g s^{-1} and 8.04 x 10^7 g s^{-1}, with the Northeast Water Polynya having a significantly smaller moisture flux because measurements were made in April and May where turbulent fluxes are much smaller than in the winter months. *Renfrew et al.* [2002] studied coastal polynyas in the Weddell Sea, having an area of 13,000 km^2, which is roughly the same size as the 2006, 2008 and 2009 North Water Polynyas. Even though the coastal Weddell Sea polynyas are slightly smaller in size it shows good agreement with our results having 2.60 x 10^8 g s^{-1} compared to our estimates of 4.25 x 10^8 g s^{-1}, 2.14 x 10^8 g s^{-1}, and 2.38 x 10^8 g s^{-1}. The 2003 North Water Polynya is the most comparable to the Mertz Glacier Polynya [*Roberts*

et al., 2001] in size and the fact that both polynyas occurred during the winter months. The 2003 North Water polynya had an area of 26,500 km^2 with a moisture flux of 7.97 x 10^8 g s^{-1} and the Mertz Glacier Polynya had an area of 23,000 km^2 with a moisture flux of 6.26 x 10^8 g s^{-1}. The Mertz Glacier Polynya was only 86% of the size of the 2003 polynya, and lost roughly 78% of the amount of moisture as the 2003 North Water polynya, showing that our estimates are reasonable. The fact that all of our calculated moisture fluxes agree with other moisture fluxes measured or calculated using in situ and moisture flux calculations.

Table 7. Comparisons of Moisture Fluxes x 10^{-3} (g m^{-2} s^{-1})

Study	**Region, Time of Year, Year**	**Data Type/Spatial Size**	**Length or Area**	**Moisture Flux x 10^{-3} (g m^{-2} s^{-1})**
This study: Boisvert et al., 2012	North Water, Jan/Feb, 2003-2009	AIRS, ECMWF 25km2	17,338 km2 (average) 5,555-33,350 km2	2.30 (average) 1.45– 3.19
Andreas et al., 1979	Leads, Arctic, March/April, 1974	AIDJEX Lead Experiment In situ/point measurement	20 km	2.09
Den Hartog et al., 1983	Dundas Island, Arctic, March, 1980	In situ/point measurement	0.3-0.7 km	2.04
Gultepe et al., 2003	Polynya, Beaufort Sea, April, 1998	FIRE ACE Experiment, In situ/point measurements, flights over 68-71.5N° lat x 133-139° lon	17-65 km	1.60
Kurtz % Bromwich, 1985	Antarctica, Winter, 1985	In situ/point measurement	1,300 km^2	2.72
Launianen & Vihma, 1994	Weddell Sea, Antarctic,	5 buoys drifting from 50-75°S	10^6 km^2	3.19

	1990-1992	lat x 0-60°W lon		
Pease, 1987	Bering Sea, Arctic, Feb. 1982, 83, 85	Airplane flyover, model	10-20 km	3.13
Pinto et al., 1995	Wide Arctic Lead	1-D model, 100m	0.1 km	2.12
Pinto et al., 1999	Arctic Leads, November, 1997	In situ, SHEBA, 80 km	N/A	2.00
Pinto et al., 2003	Lead, Beaufort Sea, Late April – Early May, 1998	In situ, SHEBA, 5 km	0.4 km	1.20
Renfew et al., 2002	Weddell Sea Polynya, Antarctic, 1992-1998	SSM/I, in situ, NCEP/NCAR, models, 6.25 km^2	13,000 km^2	2.00
Roberts et al., 2001	Mertz Glacier Polynya, Antarctica, August, 1999	In situ from airborne flights, 30 km	23,000 km^2	2.72
Schnell et al., 1989	Lead, Central Arctic	Model	0.05-20 km	1.56 – 2.08
Willmott et al., 1997	Northeast Water Polynya, Arctic, April & May, 1991	Monthly mean climatology, 79.5°N, 12.5°W	4,200 km^2	1.16

5.5 Results

Since the North Water Polynya fluctuates throughout January and February, we chose the largest polynya each year, 2003-2009, and selected an 11-day period for each

polynya event, starting with a day in which the polynya was either not present or had an ice concentration larger than 85%. In each case, the 11-day period ended with the polynya in the process of closing up or having an ice concentration larger than 85% (Table 8 and Figure 26). The moisture flux was calculated for each day during the polynya event using the method described by *Launiainen and Vihma* [1990] in *Boisvert et al.* [2012].

Table 8. North Water Polynya events

Year	2003	2004	2005	2006	2007	2008	2009	All Years
Polynya Dates	1/9-1/19	1/9-1/19	1/9-1/19	2/8-2/18	2/5-2/15	1/18-1/28	1/20-1/30	
Mean Moisture Flux x 10^{-3} (entire box) (g m^{-2} s^{-1})	4.75	3.13	0.58	2.89	4.75	2.20	1.50	2.78
Mean Moisture fux, polynya x 10^{-2} (g $m^{-2}s^{-1}$)	3.01	2.74	1.45	3.19	2.38	1.59	1.74	2.30
Mean of Max Moisture Flux x 10^{-2} (g m^{-2} s^{-1})	4.91	4.81	1.90	4.49	4.44	2.64	2.91	3.73
Mean Polynya Size (km^2)	26500	15170	5555	13625	33350	13465	13693	17338
Correlation between polynya size & mean moisture flux (R)	0.71	0.79	0.48	0.54	0.79	0.71	0.41	
Mean Ice Concentration of polynya (%)	66.24	63.37	71.45	63.55	61.34	69.73	63.37	65.58
Correlation between ice concentration & mean moisture flux (R)	-0.89	-0.86	-0.50	-0.93	-0.74	-0.88	-0.79	

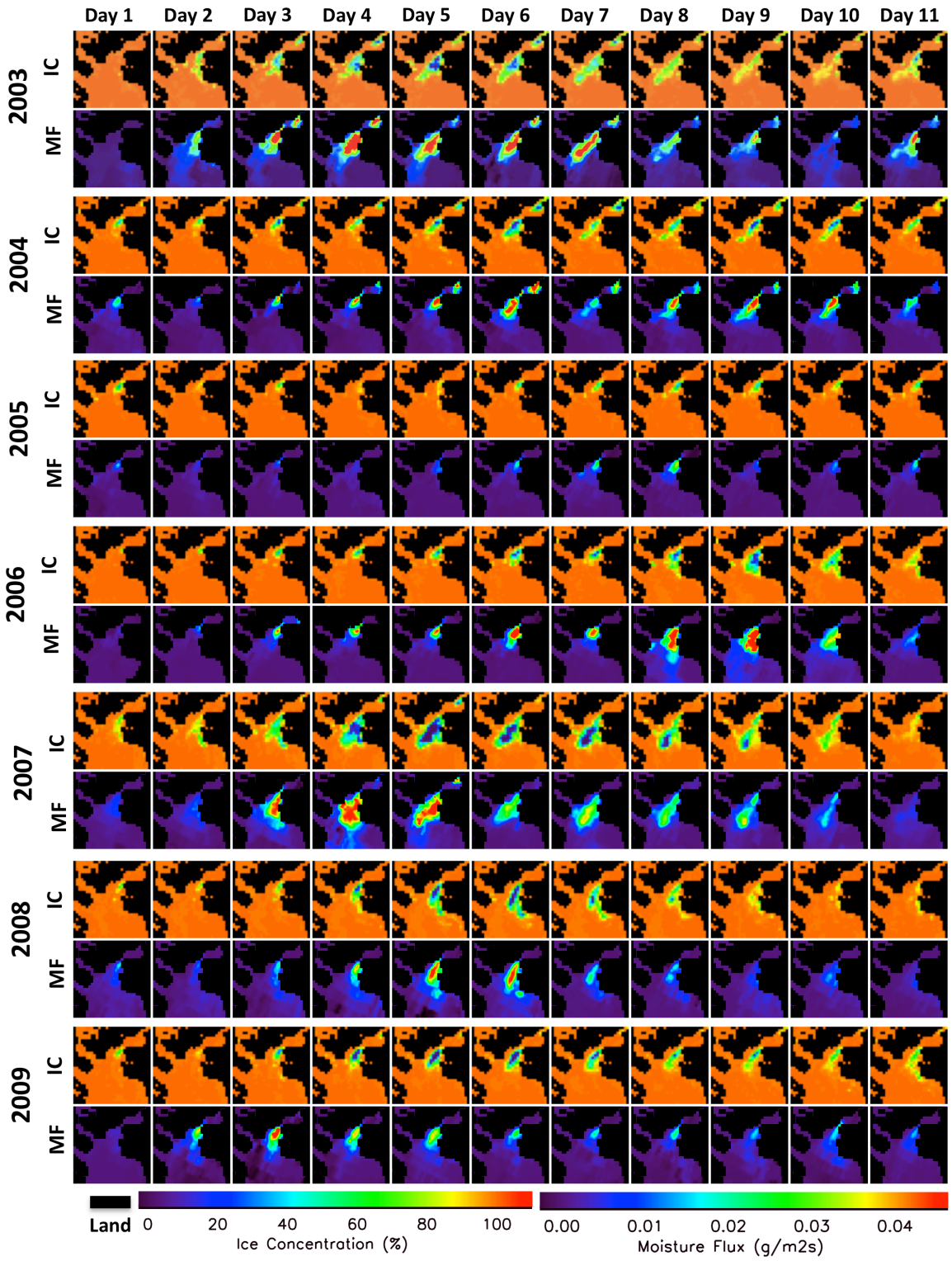

Figure 26. Maps of daily ice concentration [IC] (%) (top row) and moisture flux [MF] (kg/m^{2}day) (bottom row) for each polynya event. All maps cover the same region as the polynya map of Figure 1. Black is land.

As expected, the calculated moisture fluxes over the solid ice pack were much lower than over the polynya (Figure 26). For example, the moisture flux over the solid ice before the 2003 polynya event was 4.63 x 10^{-4} g m^{-2} s^{-1} as opposed to 3.01 x 10^{-2} g m^{-2} s^{-1} over the polynya, which is almost seventy times larger. During the polynya event, the moisture from the polynya is transported over the ice via winds. Once the polynya has closed up, the moisture over the ice remains noticeably larger than before the polynya event. Thus the polynya altered the amount of moisture over the ice pack.

During the 2003 polynya event, which in many respects appears typical, the moisture flux starts out low (day 1) due to the solid ice pack; then once the polynya opens, the moisture flux begins to increase (days 2-3) (Figure 26). When the polynya reaches its largest size, the moisture flux is at its maximum and the moisture is transported via north winds into the Baffin Bay (day 4). These effects are seen for the next few days, with the maximum moisture flux area becoming smaller (days 5-7). As the polynya begins to close up, the moisture flux decreases over the entire region and the moisture flux from the polynya itself is reduced (days 8-11). Although each polynya event is unique, this sequence is roughly the same in each case. The amount of moisture transferred from the polynya to the atmosphere depends strongly on the ice concentration during the event; the less ice coverage, the larger the moisture flux for all years except 2005. The moisture flux is also dependent on the area of the polynya, which is defined as the enclosed area with ice concentration less than 85%. In most cases, the larger the size of the polynya the larger, the flux of moisture. However, the 2007 North Water polynya had the largest area at 33,350 km^2, but did not have the largest moisture flux, with 7.95 x 10^8 g s^{-1}. The 2003 polynya had an area only 80% of that in 2007, but the moisture flux was 2.30 x10^6 g s^{-1}

greater than in 2007 (Table 8). The moisture flux depends on the ice concentration as well as on the area, and on the air temperature and moisture and the wind speed. There is also the issue of how the North Water Polynya is formed. Normally, it forms via northerly winds that channel through the Smith Sound, southward ocean currents, and oceanic upwelling. The winds and currents force the ice away from the ice bridge and upwelling helps to sustain lower ice concentrations [*Morales Mequeda et al.,* 2004]. Variations in these factors, for example an increase in the winds and a decrease in the upwelling, could create a smaller polynya with a larger moisture flux, like that seen in 2006.

For each polynya event a transect from the northeast to the southwest through the polynya was studied to understand how the moisture flux progressed over time (Figure 27). The transect, the white line in Figure 21, begins from Greenland in the northeast and ends near Baffin Island in the southwest. The polynya begins to form and opens up right along the coast in this particular case. This transect was chosen because it passes through the longest fetch of the polynya. On February 9, 2006, the polynya was not present and the moisture flux was very low and uniform, only amounting to 5.56×10^{-3} g m^{-1} s^{-1} as integrated over the entire transect (Figure 27). Once the ice pack began to break up on February 10th and 11th there was a dramatic increase in the amount of moisture exchanged (1.14×10^{-1} and 9.53×10^{-2} g m^{-1} s^{-1} integrated over the entire transect), and the moisture flux was increased over the ice pack. On February 15-16, the polynya was at its largest area and the integrated moisture flux over the entire transect reached 6.29×10^{-1} g m^{-1} s^{-1}. During these days there was a larger flux of moisture over the sea ice. From February 10 to February 16 the peak of the moisture flux curve moved along the transect from the northeast to the southwest towards the thick ice pack. The polynya closed up

rapidly over the course of a day, and by February 17 and 18 the moisture flux had decreased significantly, down to 7.66 x 10^{-2} g m^{-1} s^{-1} integrated over the transect. Before the polynya opened up there was relatively no flux of moisture between the surface and the atmosphere due to the insulating sea ice, but once the polynya opened up, a large exchange of moisture from the ocean to the atmosphere occurred (Figure 27).

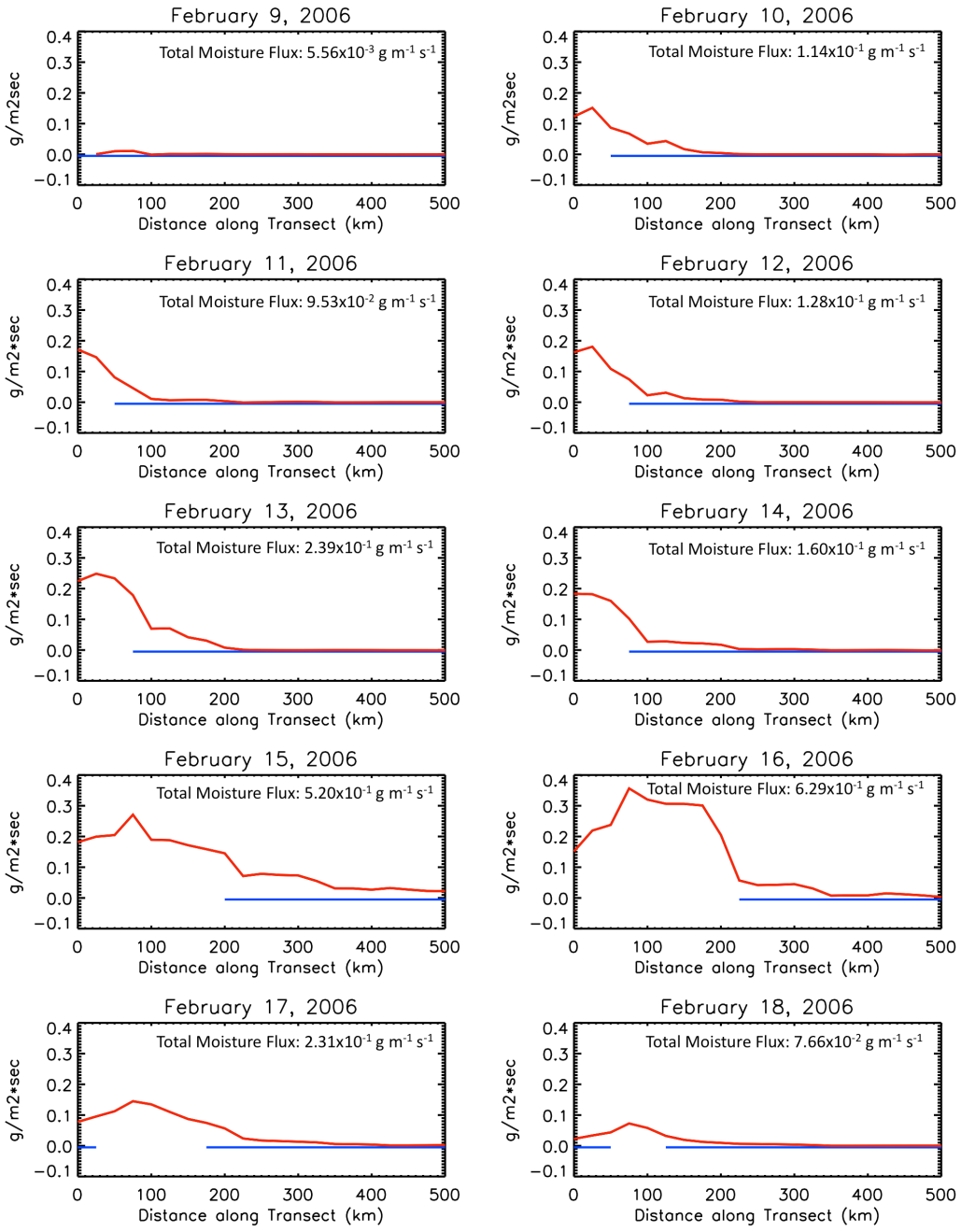

Figure 27. Transects of the moisture flux (kg/m^{2}day) for the 2006 polynya event (black curve). Red line signifies moisture flux; blue line signifies ice of $\geq$ 85% concentration, no line signifies the polynya.

Although only one example is shown here, each polynya event behaves qualitatively similarly to the 2006 event, although with different flux magnitudes. The total moisture flux from the polynya, integrated over the transect and the duration of the polynya event, ranged from a low value of 4.60×10^{-1} g m^{-1} in 2005 (light blue line in Figure 28) to a high value of 3.01 g m^{-1} in 2007 (orange line in Figure 28). The reasons for these differences include differences in the wind speed and air specific humidity as well as in the size and duration of the polynya event. For the entire polynya, the moisture flux was the greatest out of all the years in 2006 and the smallest in 2005.

The integrated moisture flux over the transect had a qualitatively similar pattern for each polynya event (Figure 28). At the beginning of each event, the integrated moisture flux along the transect is low, averaging 4.46×10^{-2} g m^{-1} s^{-1}. The integrated moisture flux over the transect increases as the polynya opens, with its maximum value averaging 4.26×10^{-1} g m^{-1} s^{-1} over the different polynya events. After reaching its maximum, the integrated moisture flux over the transect either drops off gradually or sharply, depending on the year, until the last day of the event, when the average integrated moisture flux decreases to 8.37×10^{-2} g m^{-1} s^{-1}. Differences arise from year to year depending on how long the moisture flux remains elevated. For instance, in 2003 (black line in Figure 28), the integrated moisture flux remained high from day 1 to day 5, whereas in 2008 (red line in Figure 28) it only remained elevated on days 3-5. The polynya in 2006 behaved differently from the other years because it reached its maximum at day 8 and then dropped off gradually, whereas in the other years the maximum occurred around day 4 and the drop off was more gradual.

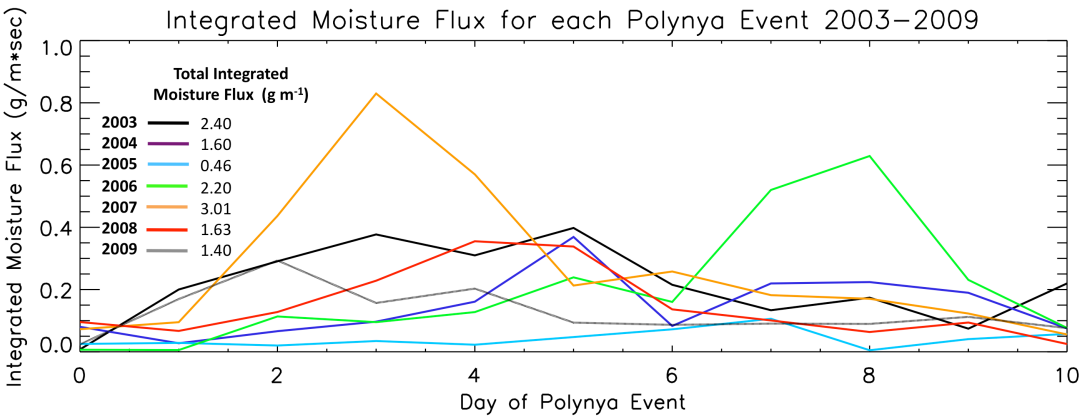

Figure 28. Total integrated moisture flux along the transect for each of the years in this study.

5.6 Summary

For the first time, the moisture flux has been calculated for the North Water Polynya using instruments onboard the Aqua satellite. One polynya event was chosen for each year 2003-2009, allowing us to examine differences in moisture fluxes between individual events and to have multiple events to include in our error estimates. The moisture flux was calculated using the bulk aerodynamic formulas of *Launiainen and Vihma* [1990]. AIRS and AMSR-E have the ability to detect small-scale features as well as their atmospheric effects, so that they can also be used to study polynyas over large spatial and temporal scales. Using this approach, the moisture flux produced by the polynyas can be studied in detail. Although the examined polynya events differ, the

moisture flux behaves in a similar fashion in each of them, beginning with low values, increasing to its maximum when the polynya reaches its largest area, and decreasing as the polynya closes back up. The moisture flux over the most compact ice is often five times smaller before the polynya opens than after it closes, as a result of the moisture that enters the atmosphere during the polynya's presence.

The uncertainties of our moisture flux estimates are calculated to be only 25%, which is quite encouraging. Comparing our moisture flux calculations with those of *Raddatz et al.* [2010], we had very similar results with a difference of 5.79×10^{-5} g m^{-2} s^{-1} on the upper bound and a difference of 3.01×10^{-4} g m^{-2} s^{-1} on the lower bound during the time period. The AIRS moisture flux is an improvement to the ERA-Interim moisture flux because of the improved accuracy of temperature and humidity profiles from AIRS and the higher resolution of AMSR-E ice concentration, which allows for larger and more accurate moisture flux estimates to be made over the polynya. Comparing our moisture flux estimates to those reported in studies on other polynyas, we find that our fluxes fall within one standard deviation of the average of the other studies.

In the next chapter we will expand our moisture flux calculations to the entire Arctic, in order to observe larger-scale effects of changing sea ice and atmospheric conditions on moisture fluxes over the period of Aqua satellite observations.

Chapter 6: Moisture flux over the entire Arctic

6.1 Background

Recent studies show increases in the amount of water vapor in the Arctic troposphere, though time periods, data and methods vary [*Dee et al.,* 2011; *Screen and Simmonds*, 2010; *Rinke et al*., 2009; *Serreze et al*., 2012], and it is not clear if these increases are due to an increase in the evaporation in the Arctic or an increase in the atmospheric transport of moisture from lower latitudes to the Arctic. Increases in the air relative humidity can warm up the lower atmosphere via the release of condensation heat in cloud formation, and an increase in the air specific humidity causes warming because water vapor is a greenhouse gas. Thus, excess moisture can increase ice ablation and will cause the ice pack to be more vulnerable in the following years.

As in the previous chapter, the moisture flux is defined as the vertical flux of water vapor due to atmospheric turbulent transport [*Boisvert et al.,* 2012]. It is affected by the difference between the saturation specific humidity corresponding to the surface temperature of the ocean or sea ice and the air specific humidity close to the surface, as well as by three factors affecting the intensity of the turbulent exchange: wind speed, surface roughness and thermal stratification [*Launiainen and Vihma,* 1994].

Large-scale moisture fluxes are available in various atmospheric model reanalysis, but these are known to have discrepancies in the moisture variables [*Cullather et al.,* 2000; *Jakobson and Vihma,* 2010; *Lüpkes et al.,* 2010; *Jakobson et al*., 2012]. Using

satellite data on air moisture in order to calculate the moisture flux would allow an alternative approach for large-scale moisture flux estimates over the Arctic.

We have taken full advantage of such data from Aqua to calculate and study recent changes in the moisture flux over the entire Arctic from 2003-2011. Since our method has proven accurate, having 20% uncertainties in our estimates and has been validated via comparisons with Tara data (see 5.3 and 5.4), and demonstrates that the satellite data has the resolution and accuracy needed to compute the moisture flux, we have expanded our study to the entire Arctic. The study area for the entire Arctic is show in Figure 29. The same approach to calculate the moisture flux over the North Water polynya will be taken to calculate the moisture flux over the entire Arctic except that we will use our updated method described in 4.2.3. We calculate the moisture flux for each day over the 2003-2011 period.

We will use the melt and freeze onset datasets from *Markus et al.* [2009] to distinguish between summer and winter for each pixel. The summer parameterizations will be used from the first day that the melt onset begins until the first day that the freeze onset begins. The winter parameterizations will be used for all of the other days. In order to apply the snow/ice surface roughness needed to calculate the C_D, the ice concentration is used to determine which pixels contain first-year or multi-year ice.

Once this has been completed then we can look at the moisture flux over the entire Arctic on a yearly, seasonal and monthly basis to look for variability and changes that have occurred over all and between the years in the study. The seasons will be split up into Winter (January, February and March), Spring (April, May and June), Summer (July, August and September) and Fall (October, November and December). The moisture flux

will also be evaluated for regions 4-10 pictured in Figure 29 to study changes on a regional level.

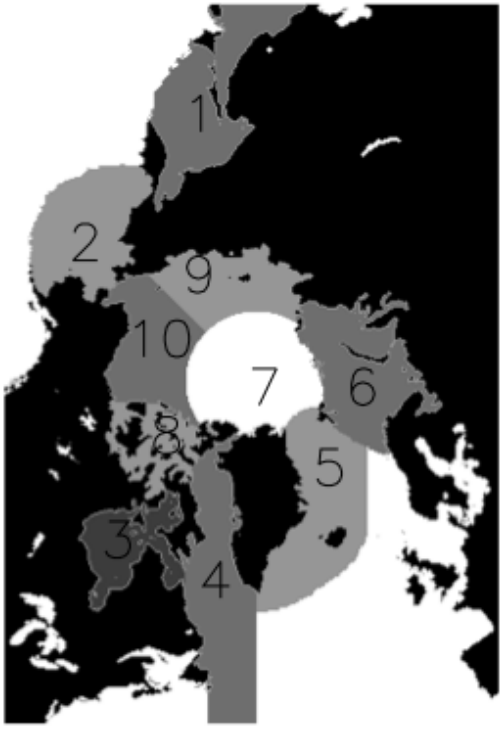

Figure 29. Illustration of the Arctic and its different regions. [*Markus et al.,* 2009] 1)Sea of Okhotsk, 2)Bering Sea, 3)Hudson Bay, 4)Baffin Bay, 5)East Greenland Sea, 6)Kara/Barents Seas, 7)Central Arctic, 8)Canadian Archipelago, 9)Laptev/East Siberian Seas, 10)Chukchi/Beaufort Seas

6.2 Validation of the moisture flux for the entire Arctic

Using the surface temperature from the Tara drifting station, we were able to access the accuracy of AIRS surface temperature in the Arctic to improve our moisture flux error estimates. The surface temperature from AIRS was taken for each 625 km^2 pixel that corresponded to the daily latitude and longitude of the Tara drifting station from April

1, 2007 until September 20, 2007 (Figure 30). The surface temperature from AIRS had a warm bias of 1.06 °C owing to Tara reporting 0 °C from day 160 (June 9, 2007) until day 230 (August 18, 2007). Since Tara was on an icefloe it measured the temperature of the ice in the summer months, where as AIRS measured the surface temperature over 625 km^2, which had open water during these summer months. Regardless, the root square mean uncertainty was found to be 2.70 °C and the temperatures from Tara and AIRS were highly correlated with $R^2 = 0.81$ (Figure 31). There was no overall bias in the estimates, but there is much larger variability in the Aqua satellite data compared to the in situ data.

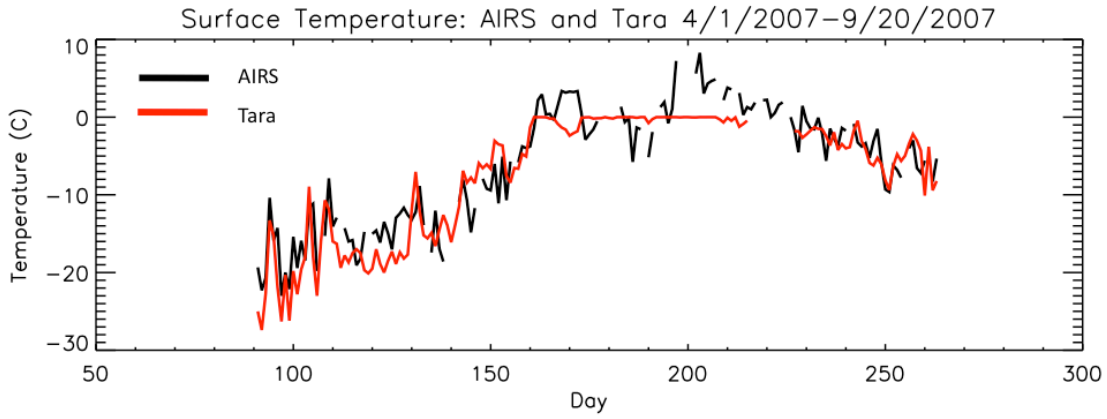

Figure 30. Surface temperature from AIRS and the Tara drifting station from April 1, 2007 until September 20, 2007. AIRS is the black line and Tara is the red line.

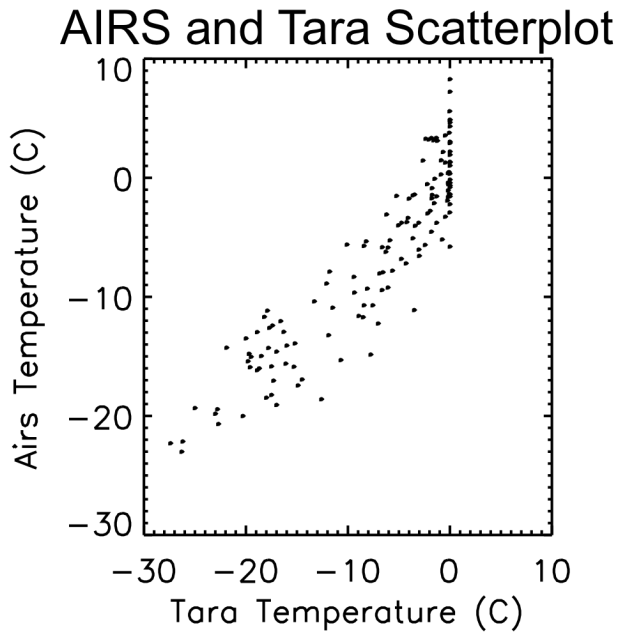

Figure 31. AIRS surface temperature and Tara surface temperature scatter plot from April 1, 2007 until September 20, 2007.

In order for our estimate of the 2m specific humidity to be accurate, the 1000 hPa relative humidity from AIRS must be accurately observed and our updated Monin-Obukhov similarity theory must be valid when applied to a level higher than 2m. This validation is done using 2m specific humidity observations from the Tara drifting station [*Vihma et al.,* 2008], which drifted in the central Arctic (location 7, figure 29). The 1000 hPa relative humidity from AIRS was taken for each 625 km^2 pixel that corresponded to the daily latitude and longitude of the Tara drifting station from April 1, 2007 until September 20, 2007 (see Figure 32). Since the 1000 hPa geopotential heights during this period range from -101 m to 243 m, the relative humidity is used to calculate the specific

humidity and is then integrated to the standard 2m height using the Monin-Obukhov theory. This is what is done in all of our moisture flux calculations.

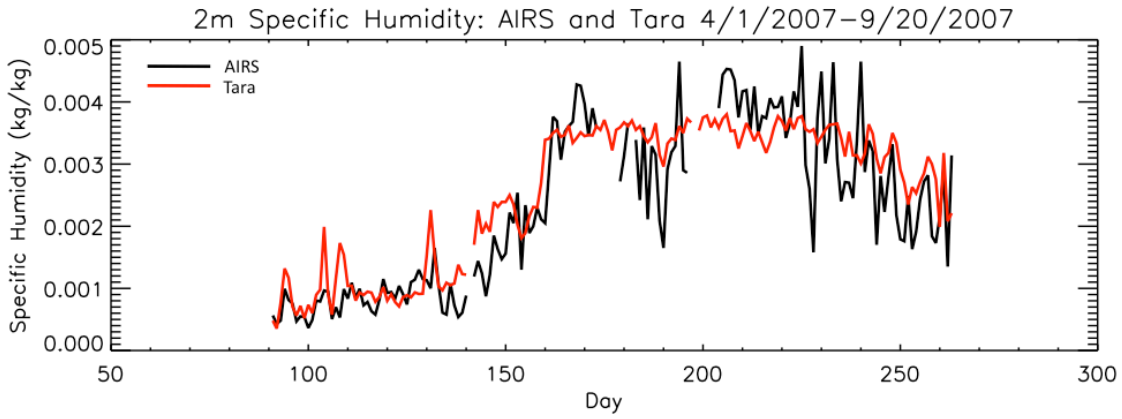

Figure 32. The 2m specific humidity (kg kg^{-1}) from AIRS (black line) and Tara drifting station (red line) from April 1 until September 20, 2007.

The RMS error for the AIRS 2m specific humidity was 4.57 x 10^{-4} g kg^{-1}, equating to a 20% error from the Tara 2m specific humidity. The 2m AIRS and Tara specific humidity were also highly correlated, having an R-value of 0.86. This is very encouraging for two reasons: a) the point measurements at Tara are compared against the 625km^2 pixel values of AIRS and still the errors are small and b) the average daily specific humidity from Tara was used to compare to AIRS. Since Aqua only passes over the exact location a few times a day, a more detailed validation could be done comparing the observations at exactly matching times, but this is out of the scope of this study. Our result is similar to the 20% error that *Tobin et al.* [2006] found using version 4 water vapor profiles from AIRS when comparing them to observations from Barrow, Alaska.

We also compared the specific humidity at the surface using the surface temperature from AIRS and the Tara drifting station during the same time period in order

to determine the error from AIRS between the surface and 2m specific humidity. This yielded a 16% error from the in situ observations at Tara, and we used this in our error estimation of the moisture flux.

6.3 Error estimates for the entire Arctic

Errors in the moisture flux calculations arise from uncertainties in the input parameters, specifically the surface and air specific humidity, wind speed, air density and the water vapor transfer coefficient. A 16% error was taken for the AIRS specific humidity, which we described in the previous section. An error of 0.8 m s^{-1} was chosen for the ERA Interim wind speed following *Jakobson et al.* [2012]. The accuracy of the water vapor transfer coefficient over the open sea is probably no better than ± 20% [*Cronin et al.,* 2006]. The error of the air density was estimated from the errors in the surface temperature from AIRS (2.70K) and the SSTs (0.58K) following *Wentz and Meissner* [2000]. Average values of the calculated sensitivities, estimated uncertainties, and the final uncertainties for the entire Arctic from 2003-2011 are shown in Table 9. We assumed that the variables are uncorrelated, and this has allowed for us to make an error estimate by using (45).

Using this method and the uncertainties, the average error of the moisture flux in the Arctic was found to be 2.90 x 10^{-3} g m^{-2} s^{-1}, which corresponds to about an 20.3% error overall. This is a small error when compared to the range of moisture fluxes in the Arctic

during the 2003-2011 time period and we assume that our moisture flux estimates are valid.

Table 9. Sensitivity of the ocean-atmosphere moisture flux in the Arctic to different input uncertainties.

Variable (x)	**dE/dx**	**Σ_x**	**σ_x dE/dx**
ρ (kg m^{-3})	3.22×10^{-3}	0.83	2.67×10^{-3}
C_E	2.70	3.20×10^{-4}	8.64×10^{-4}
U (m s^{-1})	6.48×10^{-4}	0.80	5.18×10^{-4}
$q_s - q_a$ (g kg^{-1})	1.43×10^{-2}	4.80×10^{-2}	6.86×10^{-4}
σ_E (g m^{-2} s^{-1})	2.90×10^{-3}		
<E> (g m^{-2} s^{-1})	1.43×10^{-2}		

6.4 Results

In Figure 33 we present the moisture flux per month integrated over the entire Arctic for 2003-2011 (the results from (33) are multiplied by the number of seconds in a month, by the pixel area of 625 km^2, and by the number of pixels. The area around the North Pole, where no data are available, is excluded). Figure 33 also shows separately the integrated moisture flux from the open ocean (0-15% ice concentration) and from the sea ice zone (15-100% ice concentration). The total moisture flux (black line) and the moisture flux from the ocean (red line) follow an annual cycle, but the moisture flux over the ice (blue line) does not. It is interesting to note that in the summer of 2007 when the sea ice concentration was the lowest on record that the moisture flux from the sea ice zone was much higher than normal. The amount of moisture exchanged between the surface and atmosphere is lowest in July because this is the time of the year when the air

temperature and specific humidity are often close in magnitude, the average temperature and specific humidity differences being 3.9K and 0.013 kg/kg, respectively. When this occurs there is little exchange of moisture. The amount of moisture exchanged in July is on average only 17.2% of what is exchanged in October.

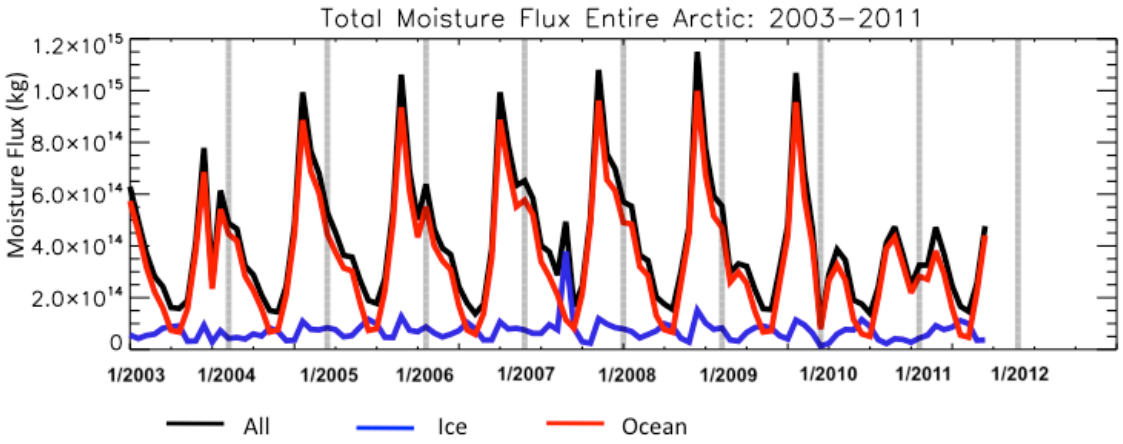

Figure 33. The total moisture flux for the entire Arctic for January, 2003 until September, 2011. The blue line is the moisture flux from the solid sea ice pack (15-100% ice concentration), the red line is the moisture flux from the ocean (0-15% ice concentration) and the black line is the moisture from both the sea ice pack and the ocean. Grey vertical lines separate the different years.

The total moisture fluxes are highest in October, with the majority of the moisture coming from the areas of open water (Figure 33). The reason for this is that in October there is still a large area of open water, specifically in the Chukchi/Beaufort and Laptev/E. Siberian Seas, which is warmer than the surface of the solid ice pack. In October the air temperatures begin to rapidly decrease, whereas the SSTs drop off much more slowly due to the large heat capacity of the ocean, creating temperature and specific humidity differences between the sea surface and air of around 7 K and 0.080 kg/kg and substantial moisture fluxes. But this trend is starting to shift towards warmer air temperatures

extending into October, possibly due to larger areas of open water in the summer and warmer SSTs creating warmer air temperatures. In 2010, the air temperatures were larger than the surface values in an area extending from the E. Siberian Sea to the north coast of Greenland (Figure 34).

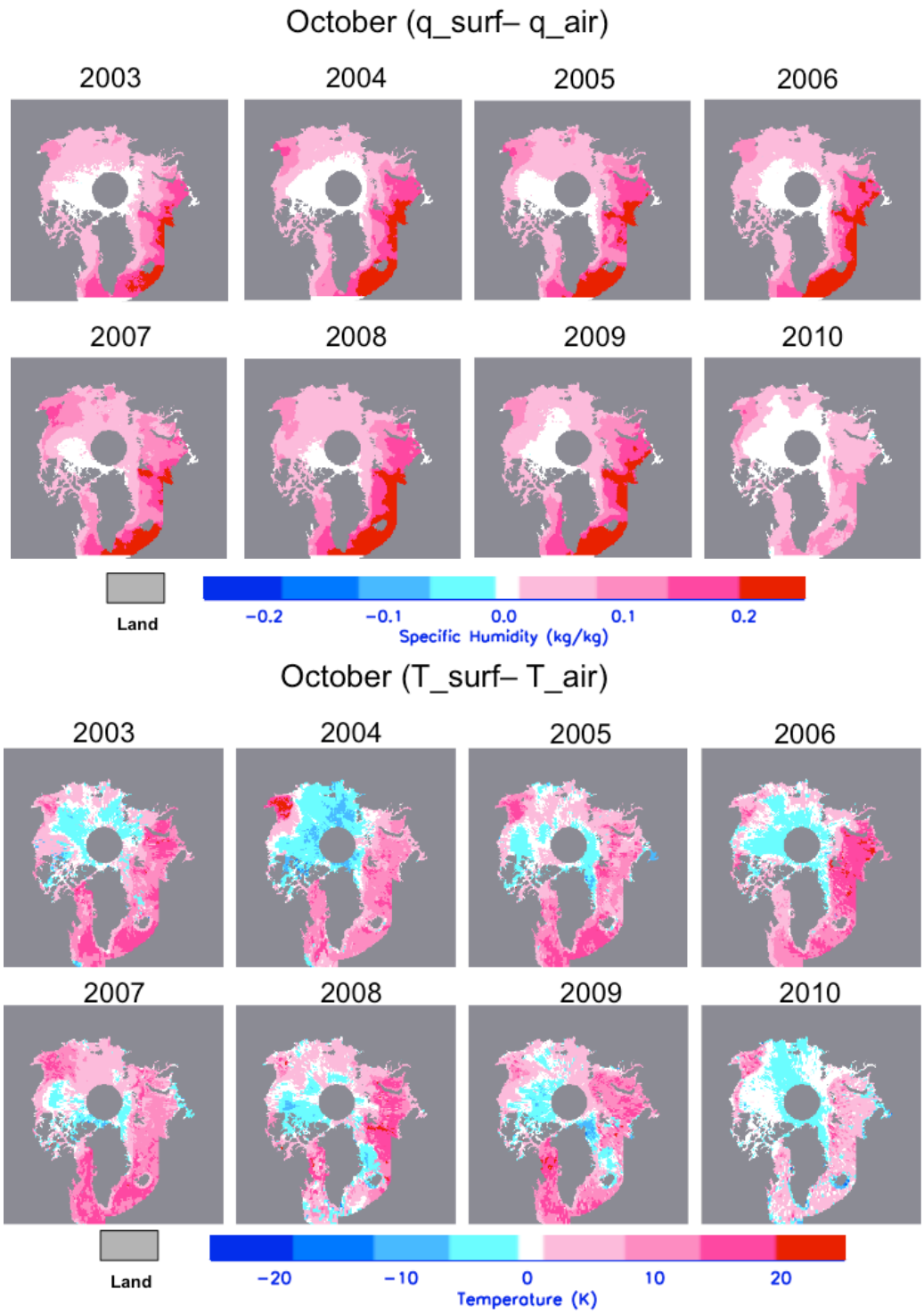

Figure 34. (Top) The 2m specific humidity and surface specific humidity (kg/kg) differences for the month of October for each year 2003-2010 for the entire Arctic. (Bottom) The 2m air temperature and surface temperature (K) differences for the month October for each year 2003-2010 for the entire Arctic. The grey is either the land or no data in both images.

These moisture fluxes remain elevated in the winter months because of the vertical differences in specific humidity that arise due to areas of leads and polynyas and larger areas of open water. They drop off rapidly in the spring and are the lowest in the summer months when the air is warmer than the surface and the air specific humidity is only slightly lower than that of the surface.

The amount of moisture put into the lower atmosphere in the Entire Arctic each year is decreasing 1.9 %/yr between 2003-2010, but it is not statistically significant (Figure 35). There are changes seen on a regional level, for instance in the Chukchi/Beaufort, Laptev/E. Siberian Seas, Canadian Archipelago and the Central Arctic there has been 35.97 kg/m^2, 20.6 kg/m^2, 19.15 kg/m^2 and 30.31 kg/m^2 of excess water added to the lower atmosphere between 2003-2010, respectively. Conversely, regions like the Kara/Barents Seas, East Greenland Sea and Baffin Bay are not releasing moisture as much as in the previous years, losing 20.6 kg/m^2, 2.8 kg/m^2 and 0.5 kg/m^2, respectively, between 2003-2010. Figure 30 shows the anomalies of yearly moisture flux, integrated over pixels 625 km^2 large, for 2003-2010. This figure shows that in years 2003, 2004, 2009, and 2010 the moisture flux anomalies were negative over most of the Arctic, whereas in years 2005, 2006, 2007 and 2008 they were positive. Since 2007, the regions of Baffin Bay, E. Greenland and Kara/Barents Seas have changed from a positive to a negative anomaly. Reasons behind these changes are discussed in the following section.

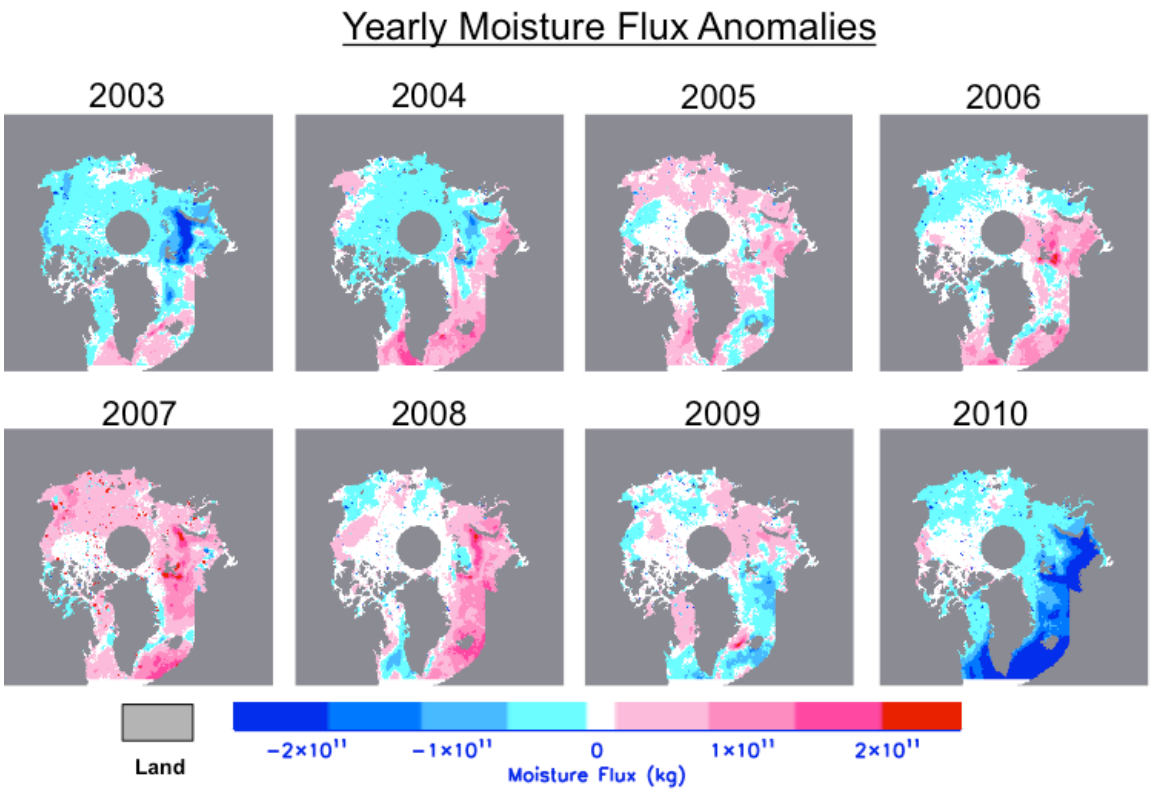

Figure 35. The difference between the yearly moisture flux and the average moisture flux from 2003-2010. Positive anomalies are shown in pinks, negative in blues. The grey is either the land or no data.

6.4.1 Monthly Trends

Looking at how the aerially integrated monthly moisture flux changes on a yearly basis, one sees a slightly different story. A linear regression was applied to the monthly total moisture flux and average ice concentration (15-100% ice) for each month from 2003-2011. For October – December the data records are only for 2003-2010. A statistical t-test was then performed on each linear regression to determine whether or not the trend seen in the data was due to actual changes in the variables as opposed to just random chance. Table 10 shows the moisture flux trends for each month. The total moisture flux,

summed over the ocean and sea ice, has decreased at the 95% confidence level in January (by 8.1%/yr), February (5.5%/yr) and December (7.1%/yr). During these months, the moisture flux is driven by areas where there is open water specifically the Kara/Barents Seas, E. Greenland Sea and Baffin Bay regions. In these regions, the 2m-air temperature has increased by 6.0 K and the specific humidity difference between the surface and the air has decreased by 0.055 kg/kg between 2003-2011, whereas the SSTs have increased less, only 1.3 K (Figure 36).

Table 10. Trends in monthly moisture flux from the entire Arctic during 2003-2011. Numbers highlighted in bold are statistically significant in the 95% confidence level.

Month	Trend (kg/yr) (All)	Trend (kg/yr) (Ice)	Trend (kg/yr) (Ocean)
January	**-4.04×10^{13}**	-2.46×10^{12}	**-3.79×10^{13}**
February	**-2.40×10^{13}**	-1.53×10^{12}	**-2.25×10^{13}**
March	8.31×10^{12}	2.88×10^{12}	5.44×10^{12}
April	7.08×10^{12}	2.37×10^{12}	4.71×10^{12}
May	-2.57×10^{12}	1.32×10^{12}	-3.91×10^{12}
June	4.82×10^{11}	2.23×10^{12}	-1.74×10^{12}
July	-1.59×10^{12}	1.12×10^{12}	**-2.71×10^{12}**
August	7.40×10^{12}	7.47×10^{11}	6.65×10^{12}
September	4.43×10^{11}	-7.32×10^{11}	1.18×10^{12}
October	-1.68×10^{13}	-3.04×10^{12}	-1.37×10^{13}
November	6.58×10^{12}	3.11×10^{12}	3.97×10^{12}
December	**-3.94×10^{13}**	-4.11×10^{12}	**-3.53×10^{13}**

Figure 36 shows many interesting anomalies between the 2m air and surface temperatures and specific humidities, which warrant more discussion. On average, in

summer the air is much warmer than the sea surface, but the surface specific humidity is still larger than the air specific humidity in the Kara/Barents Seas, E. Greenland Sea and Baffin Bay regions (black line), whereas in the fall and winter months the open sea surface is much warmer than the air and the specific humidity at the surface is much larger than at 2m. However, there has been a major anomaly during this study period in the winter of 2010-2011, when the temperature differences in these regions were very small. In the other regions of the Arctic (red line), the surface and air temperatures are close to each other in summer, because both are close to the freezing point. In winter, when regions 7-10 are covered by sea ice, the surface is often much colder than the air above, due to the negative radiation balance and generation of a surface-based temperature inversion [e.g., *Serreze et al.,* 1992]. Recently, however, there have been large inter-annual variations. These might be related to changes in the heat advection, cloud cover, and ice concentration [e.g., *Stroeve et al*., 2012] but these are out of the scope of our paper.

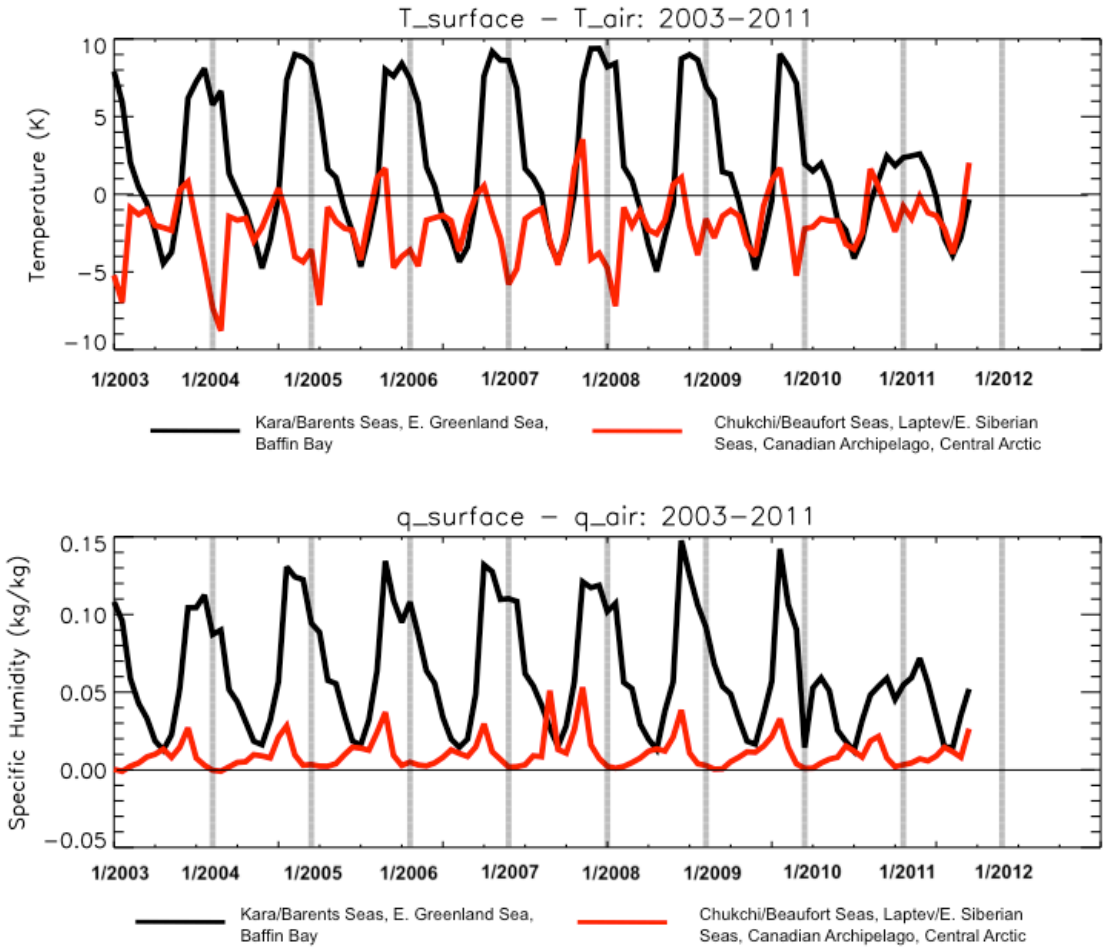

Figure 36. Top: Average temperature differences for the surface and 2m, monthly from January 2003 until September 2011. Bottom: Average specific humidity differences for the surface and 2, monthly from January 2003 until September 2011. The black line is the average difference for regions 4,5, & 6 in Figure 1. The red line is the average difference for regions 7, 8, 9, & 10 in Figure 1. The grey lines differentiate between years.

The large increase in air temperature has been accompanied by a decrease in the specific humidity difference between the surface and air in January (Figure 37), which drastically decreases the moisture flux. The temperature and specific humidity differences in the winter over the ice pack have also decreased over the time period, and in 2010 and 2011 they were on average -2.0K and 0.002 kg/kg. Since the monthly mean air specific humidity is practically the same as the ice surface specific humidity, there is very little

exchange of moisture occurring. The positive moisture flux anomalies increased from 2003 until 2007 and these positive anomalies changed to more negative anomalies from 2007-2011. The same was seen in February and December, but only January data are shown here (Figure 37).

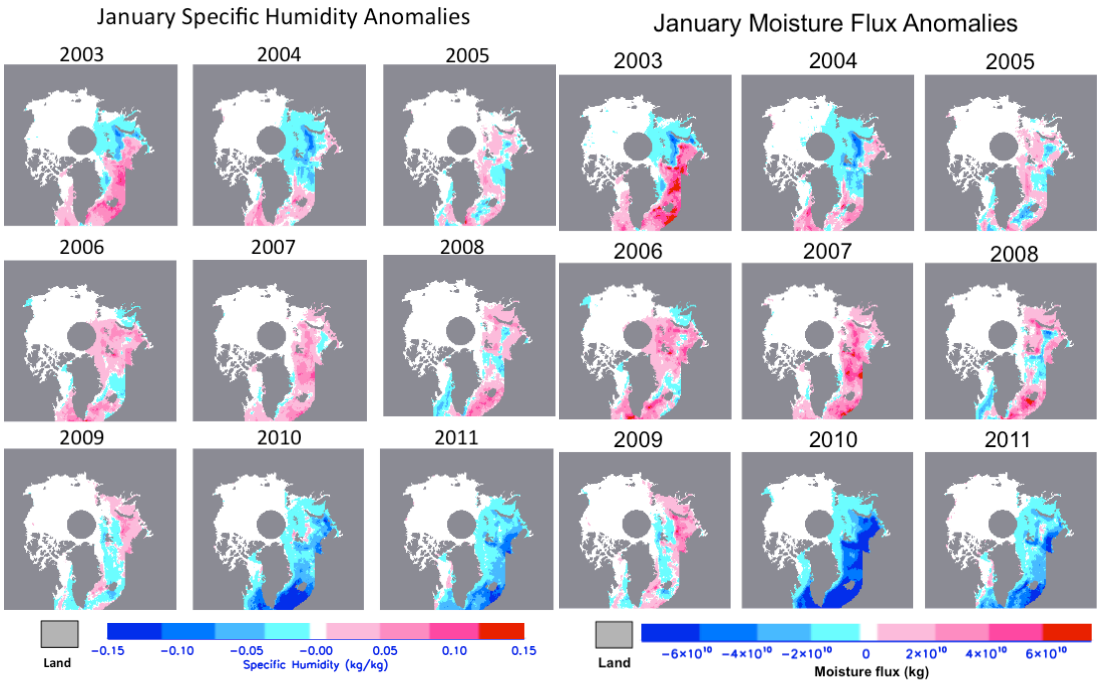

Figure 37. Left: Specific humidity (kg/kg) differences between the surface and 2m for January for 2003-2011. Right: Moisture flux anomalies (yearly minus the average moisture flux) from 2003-2011. Pinks are positive anomalies and blues are negative anomalies. Grey is either land or no data.

A decrease in the moisture flux, like that seen in 2010 over the North Atlantic regions (regions 4-6 in Figure 1), can be explained by either one or a combination of these three factors: 1) anomalously low SSTs, 2) anomalously high air specific humidity, and 3) anomalously low winds.

SST anomalies from AMSR-E in the East Greenland Sea (region 5 in Figure 29) are shown in Figure 38. From this figure it is clear that SSTs are much colder in 2010 and

2011 than in previous years. The largest negative anomalies occur in the winter months and are around -1°C. This figure strongly supports factor 1. and can explain why moisture fluxes in 2010 and 2011 are much lower than in previous years because of low SSTs in the North Atlantic regions of the Arctic.

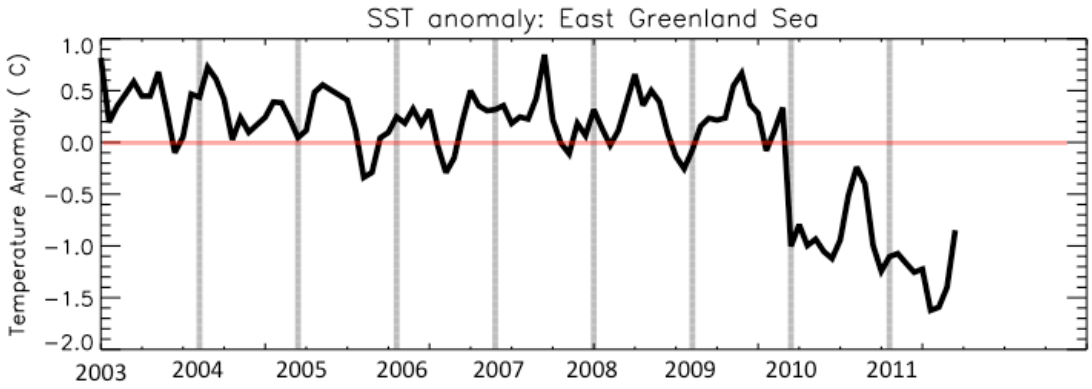

Figure 38. Average monthly SST anomalies for the East Greenland Sea from January, 2003 until September, 2011. Black line is the SST anomaly from AMSR-E SST product. Grey lines delineate between years.

Figure 39 shows 1000 hPa specific humidity anomalies for January 2010, October 2010 and January-December 2010 from the 1981-2010 climatology as well as the evaporation rate anomalies. All of these images were produced from ERA-Interim reanalysis data using the Web-based Reanalysis Intercomparison Tools (WRIT) maps (https://reanalyses.org/atmosphere/web-based-reanalysis-intercomparison-tools-writ). There are positive 1000 hPa specific humidity anomalies in both January and October 2010 (Figure 39 c,d) around the southern tip of Greenland and into Baffin Bay. Positive anomalies are also seen in the Kara/Barents Seas. There are also 5°C 2m temperature anomalies seen in these same regions (not shown). Looking at the 1000 hPa specific humidty anomalies for the entire year in 2010, again ERA-Interim produces large negative

anomalies in East Greenland Sea and Baffin Bay (Figure 39 f), which again supports smaller moisture fluxes. Figure 39a shows the evaporation rate anomaly produced by ERA-interim for January 2010. Here we see negative evaporation rates in the East Greenland Sea, which corresponds with our data. This is also seen for the entire year evaporation rates (Figure 39c).

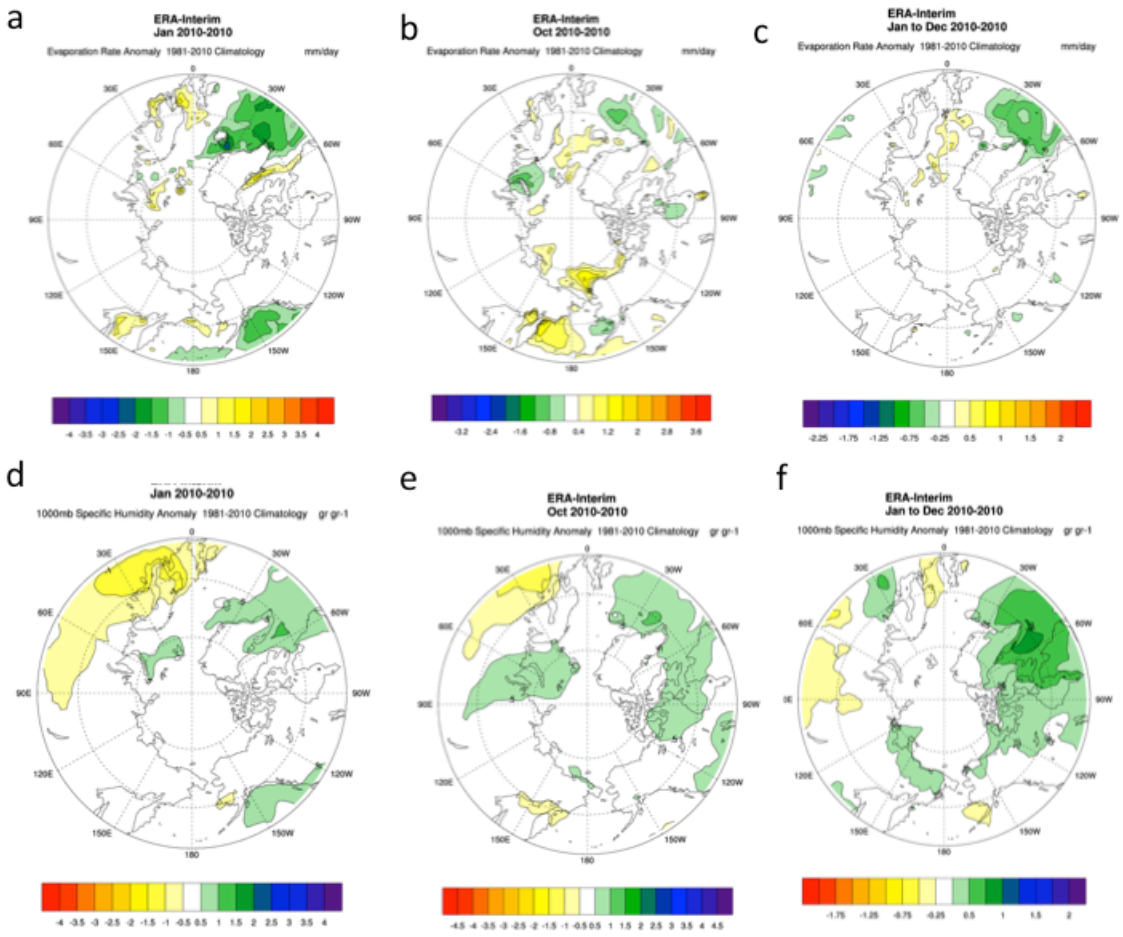

Figure 39. a) ERA-Interim January 2010 evaporation rate (mm/day) anomaly for the northern hemisphere, b) ERA-Interim October 2010 evaporation rate (mm/day) anomaly for the northern hemisphere, c) ERA-Interim January-October 2010 evaporation rate (mm/day) for the northern hemisphere, d) ERA-Interim January 2010 1000mb specific humidity (g/g) anomaly for the northern hemisphere, e) ERA-Interim October 2010 1000mb specific humidity (g/g) anomaly for the northern hemisphere, f) ERA-Interim January-December 2010 1000mb specific humidity (g/g) anomaly for the northern

hemisphere. All of these images were produced using WRIT at https://reanalyses.org/atmosphere/web-based-reanalysis-intercomparison-tools-writ.

We also looked into the observed differences between the sea surface and 2 m air specific humidity in 2003-2011. Monthly mean 2 m specific humidities were calculated from air temperature and relative humidity observations at weather stations in Longyear airport, Svalbard (http://eklima.met.no) and Keflavik airport, Iceland (http://en.vedur.is), and the sea surface saturation specific humidities were calculated from AMSR-E SST data from the sea pixels nearest to the weather stations. At the Svalbard station (Figure 40a) it is evident that the specific humidity differences in 2010-2011 are smaller than in previous years creating a decrease in the moisture flux during these times. Figure 40b shows the same for Iceland, although this decrease is not as evident. It is important to keep in mind that the atmospheric observations were taken from coastal weather stations, as opposed to our AIRS-based estimates being made over the ocean where specific humidities could be different.

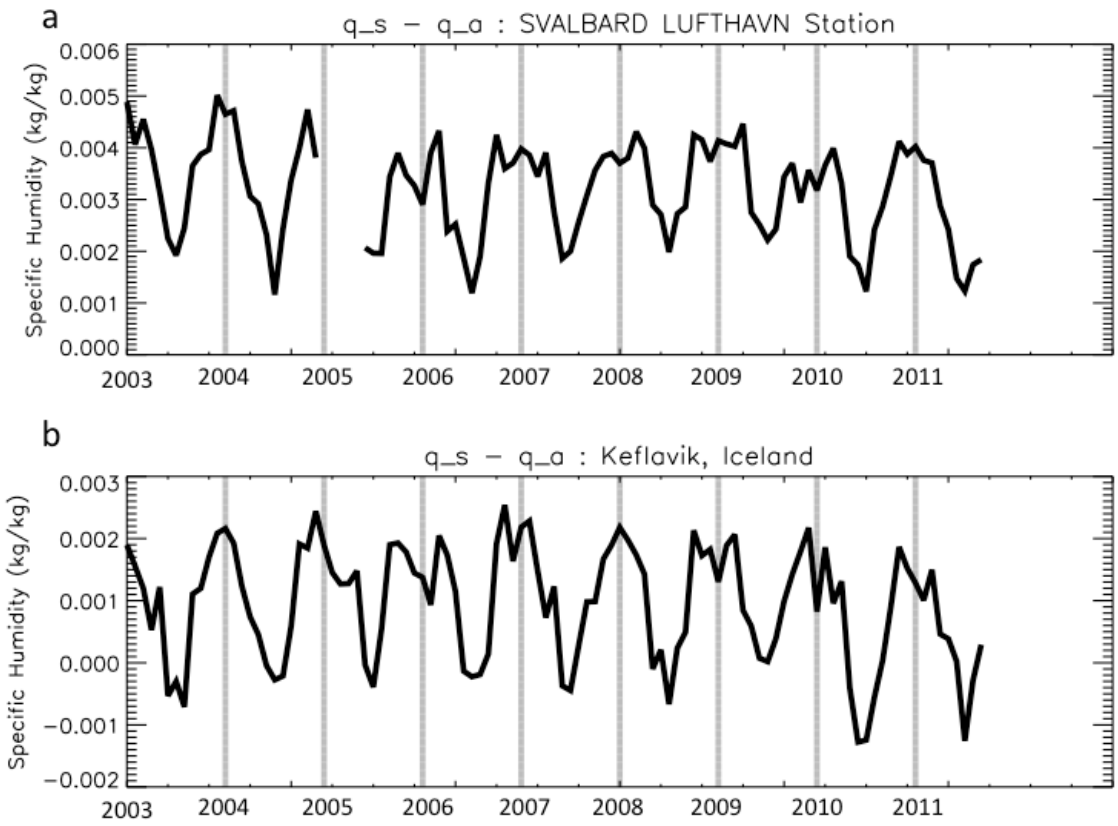

Figure 40. Monthly mean specific humidity differences between the sea surface and air at 2 m height at (a) Longyear airport, Svalbard and (b) Keflavik airport, Iceland. Grey lines delineate between years.

Finally we looked at wind speeds over the East Greenland Sea using ERA-Interim wind speed data and the Keflavik station data to see if there have been any significant changes in their magnitudes. The average monthly wind speeds in both the East Greenland Sea and Iceland follow annual cycles with the strongest winds in the winter months, but their magnitudes show no change in 2010 or 2011 from the earlier years (not shown).

By looking at these three factors that could affect the magnitude of the moisture flux in more detail we were able to determine that in 2010 the SSTs were much cooler than normal, the 1000 hPa specific humidity was higher than normal, and there were no

changes in the wind speed. The lower SSTs in this year as well as higher specific humidities created smaller specific humidity differences between the surface and the air than seen in previous years. These two changes worked together to decrease the magnitude of the moisture flux in 2010, supporting our findings based on AIRS data.

The moisture flux is increasing in March – September, although none of these increases are statistically significant. On average, the total moisture flux during these months is small, accounting for 32% of the total moisture flux in October. In these spring and summer months, the ice concentration is also decreasing at the 95% confidence level. In spring (April, May and June), the ice pack is losing 0.4% ice concentration per year, meaning that the ice pack is beginning to break up earlier exposing some of the ocean to the atmosphere. When this occurs the SSTs are very close to the freezing point of seawater and in the spring this is much warmer than the overlying air. This is enough to cause the moisture flux to increase because the moisture flux over the solid ice pack is so small. However, the increasing trends in the March – September moisture flux are not significant, demonstrating that inter-annual variability in the moisture flux does not only rely on changes in the sea ice pack; changes in humidity, wind speed and air temperatures are other essential factors.

In the summer months (July, August and September), the area of the open ocean has been increasing and this has allowed for warmer surface temperatures in September because the ocean has a lower albedo than the ice and absorbs more heat. Ocean area has increased 4.8% and the ice cover has become 6.9% less concentrated between 2003-2011 (Figure 41). Surface temperatures over the Chukchi/Beaufort, Laptev/E. Siberian Seas, Canadian Archipelago and Central Arctic have increased 1.53 K between 2003-2011.

Although the 2m air specific humidity has increased a small amount, the larger increases in area of the open-ocean and surface temperatures are the main cause of the changes in the moisture fluxes in the summer.

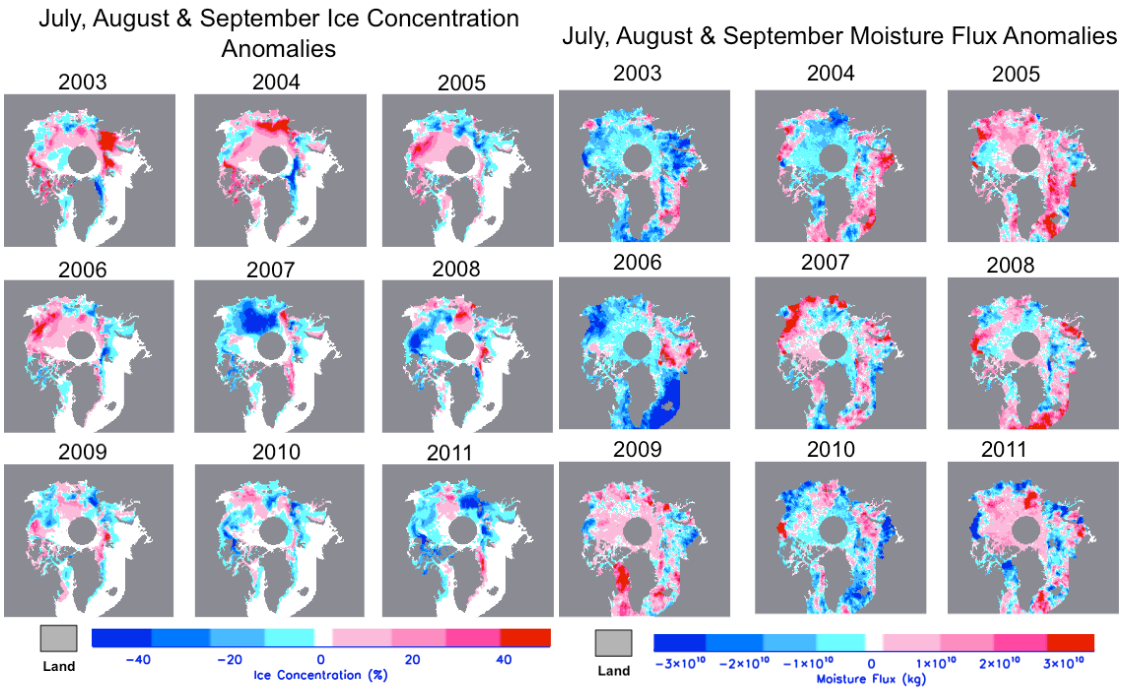

Figure 41. Left: July, August & September ice concentration anomaly with respect to the average of 2003-2011. Right: July, August and September moisture flux anomaly with respect to the average of 2003-2011. Positive anomalies are in pinks and negative anomalies are in blues. Grey is either land or no data.

The moisture flux in October from 2003-2010 on a whole is decreasing 1.8%/year. The main reason behind this is that the air specific humidity is increasing (together with air temperature), which creates smaller specific humidity differences (see Figure 36). The air temperature normally drops off rapidly in this month, but in recent years this has not happened so fast. Air temperatures remaining warmer in October could be due to excessive sensible heat fluxes from the ocean surface, related to the reduced and less

compact ice cover, that warm up the lower atmosphere, and also due to the increased cloud cover, which traps the outgoing longwave radiation [*Overland and Wang,* 2010].

6.4.2 Moisture Flux and Ice Concentration

One important factor to determine is whether or not the concentration of the sea ice pack affects the moisture flux. The sea ice pack, defined as the zone where the ice concentration is at least 15%, is becoming less concentrated during each month and each year over the 2003-2011 period (Table 11), and each trend is statistically significant at the 95% confidence level. For each month we calculated the percentage of the total moisture flux that is supplied by the ice pack (ice concentrations between 15-100%) in order to determine the effect that an ice pack with a lower concentration has on the amount of moisture evaporated (or sublimated) (Table 11). From 2003-2010 the moisture flux from the ice pack was increasing because the concentration of the ice was decreasing. Over the 2003-2010 time period, the ice has become 4.8% less concentrated and the percentage of the total moisture flux contributed by the sea ice pack has increased by 3.0%. Also, during this time period, except in 2010, in areas where the ice is less concentrated than average, the moisture flux has increased and vice versa (Figure 42). When there is no ice, or the ice pack is less concentrated, then the surface is subsequently warmer than the air.

Table 11. Monthly and yearly trends and means in sea ice concentration and the percentage of moisture supplied from the sea ice pack. Numbers highlighted in bold are statistically significant in the 95% confidence level.

	Trend of moisture from sea ice pack (%/yr)	Average % of moisture from sea ice pack	Trend of ice concentration (%/yr)	Average ice concentration (%)
January	**0.55**	12.81	**-0.59**	90.66
February	0.29	12.15	**-0.44**	92.35
March	0.35	13.88	**-0.33**	92.88
April	0.24	19.82	**-0.27**	92.59
May	**1.03**	32.63	**-0.30**	91.08
June	1.18	61.35	**-0.61**	85.04
July	**1.40**	56.76	**-0.80**	74.89
August	-0.21	15.79	**-0.80**	71.41
September	-0.18	7.28	**-0.70**	76.68
October	-0.25	11.13	**-0.69**	84.45
November	0.32	11.51	**-0.72**	90.60
December	0.07	12.43	**-0.55**	91.47
Yearly	**0.38**	34.77	**-0.60**	84.05

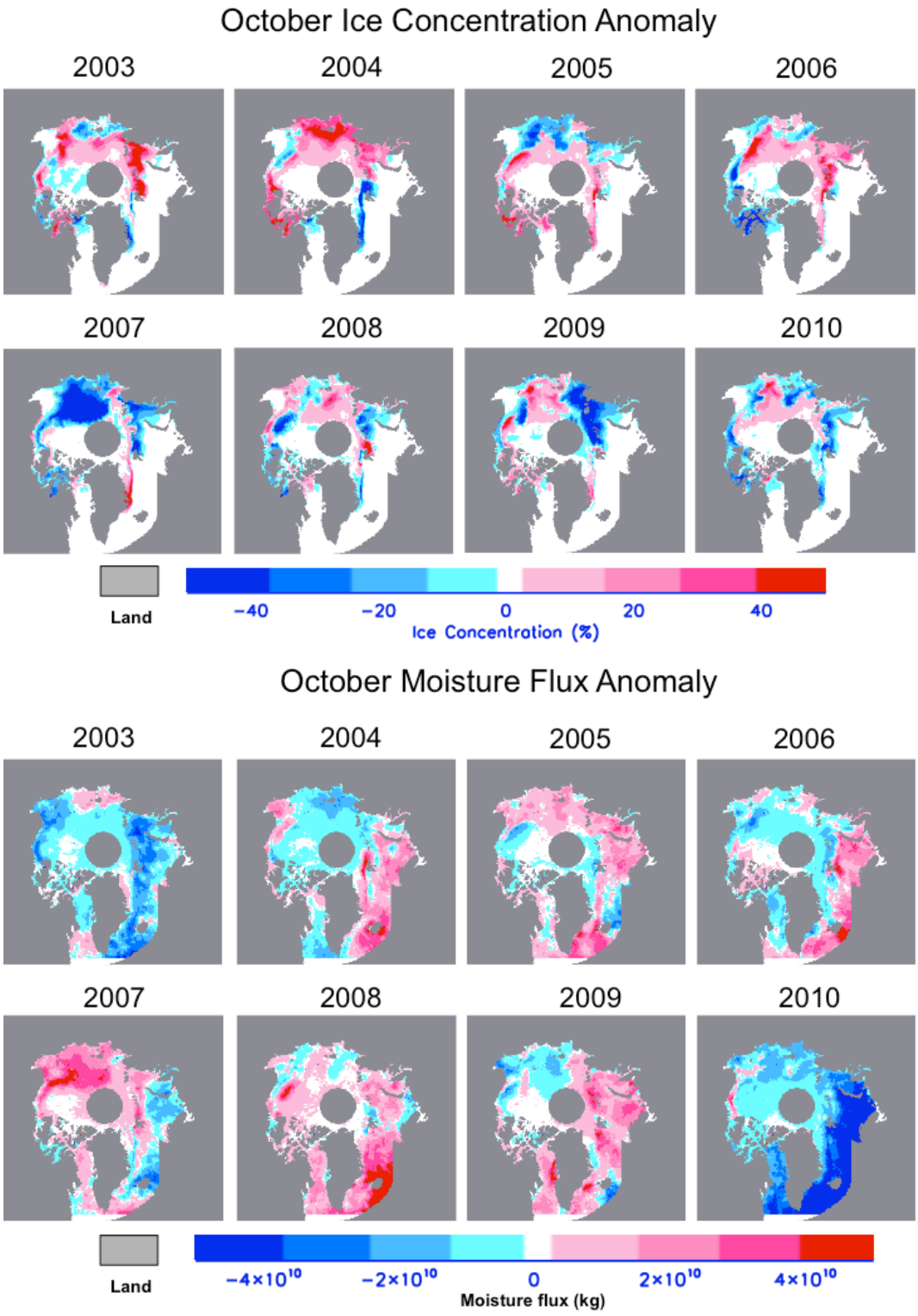

Figure 42. Top: October ice concentration anomaly with respect to the average of 2003-2010. Bottom: October moisture flux anomaly with respect to the average of 2003-2010. Positive anomalies are in pinks and negative anomalies are in blues. Grey is either land or no data.

In the winter months (November-February), although the solid ice pack only contributes on average 12.2% of the total moisture flux, this percentage has increased 2.6% and 0.6% in November and December between 2003-2010, and 5.0% and 2.6% in January and February between 2003-2011, respectively. During these cold months when the ice concentration is lower, there are more areas of open water that are exposed. The SSTs are near the freezing point, but the air temperatures are much colder, creating large temperature differences and excessive evaporation. This is essentially what happens when a lead or polynya opens. The amount of these increases would be even larger if 2m-air temperature and specific humidity during these months were not increasing.

In June and July the contribution of the moisture flux from the ice pack to the total moisture flux is also increasing. This is because the concentration of the ice pack is becoming much less, creating a warmer surface and decreasing the specific humidity differences between the surface and the air. The 2m-air temperatures during June and July are on average warmer than the surface, especially the open ocean, which is near the freezing point of sea water, whereas the snow/ice surface temperatures are close to 0°C. The amount that the ice pack is contributing to the total moisture flux is decreasing in August-October. This is because air temperatures are remaining warmer, decreasing the magnitude of the temperature and specific humidity differences (see Figure 36). Even though the percentage of moisture coming from the ice pack is increasing during June and July, it is important to keep in mind that the exchange of moisture during these months is only 20% of what it is in the fall and winter months.

6.5 Summary

Using geophysical data sets from multiple sensors on a single satellite like NASA's EOS Aqua have allowed estimates of daily surface moisture flux to be produced from 2003-2011. Evaluating this nine-year dataset has given us a clearer picture of how moisture is being exchanged between the ocean and atmosphere in the Arctic. Moisture fluxes are also available from atmospheric reanalyses. Although the fluxes have not been extensively validated in the Arctic, the air moisture includes large errors in reanalyses [*Cullather et al.,* 2000; *Jakobson and Vihma,* 2010; *Lüpkes et al.,* 2010; *Jakobson et al*., 2012], and validation results from the Antarctic sea ice zone show large errors in the reanalyses moisture flux itself [*Tastula et al.,* 2013]. We do not claim that our results are free of errors, but our approach of calculating the moisture fluxes has a strong benefit for a study on inter-annual variations. In our method, the air moisture is always based on the same sensors onboard the NASA's EOS Aqua satellite: AMSR-E and AIRS. Hence, the errors are expected to be systematic rather than varying from year to year. Instead, the amount of observations assimilated into reanalyses varies from year to year, depending on the availability of various in-situ and remote sensing data.

The flux of moisture from the surface to the lower atmosphere in the Arctic follows an annual cycle, with the largest fluxes in the fall and winter months and the smallest ones in the spring and summer months. Instead of an increase in the moisture flux due to a declining sea ice pack, there has actually been a 15% decrease between 2003-2010 as an average over the area shown in Figure 17. This decrease is mostly due to an

increase in the 2m air specific humidity over the Arctic, in particular over the Baffin Bay, E. Greenland Sea, and Kara/Barents Seas. The decrease in sea ice concentration tends to increase the moisture flux, i.e., to oppose the effect of increasing air specific humidity (except during the melting season of sea ice when the snow/ice surface is often warmer than the open ocean). This effect was not significant over areas defined as the open ocean, with sea ice concentration less than 15%. Hence, the zone where the sea ice concentration has decreased, but is still more than 15%, is contributing increasingly more to the total moisture flux from the Arctic. The locations and magnitudes of the positive moisture anomalies are changing based on changes seen in the sea ice pack and air humidity, but the total moisture flux in the entire Arctic (defined as in Figure 29) is becoming less.

On a regional scale the Chukchi/Beaufort Seas, Laptev/E. Siberian Seas, Canadian Archipelago and Central Arctic are seeing a slight increase, between 2.1 and 4.8 %/yr, in the amount of moisture flux each year. In these regions the changes in the moisture flux are due mostly to the changes in the ice concentration, which allows for the surface temperatures to increase substantially in the fall and winter months when the amount of moisture exchanged is the largest. On a regional scale, the Kara/Barents Seas, E. Greenland Sea and Baffin Bay are seeing a decrease, between 0.53 and 9.2 %/yr in the amount of moisture each year. The regions have areas of open water year round and their exchanges of moisture are due mostly to smaller differences in surface and 2 m specific humidities.

Comparison of our results to previous studies is sensitive to the exact region and time period addressed. *Screen and Simmonds* [2010b] looked at the change in the latent heat flux for January-October over the Arctic from 1989-2009 using ERA Interim

reanalysis data and in situ observations. They found increasing decadal trends in the Chukchi/Beaufort and Laptev/E. Siberian Seas regions, similar to our increases, as well as decreasing trends in the E. Greenland Sea region. In this study they did not include the Barents Sea or the months of November and December, which in our study are locations and times of significant fluxes of moisture. Because of this they concluded increases over the Arctic, whereas we have seen decreases. On the basis of ERA-40 reanalysis, *Jakobson and Vihma* [2010] concluded that evaporation in the circumpolar Arctic north of 70°N has not had any significant trend in the period 1979-2001, although the sea ice extent decreased a lot already during this period.

Recent studies by *Palm et al.* [2010], *Eastman and Warren* [2010], and *Kay and Gettelman* [2009] have looked into the changing sea ice extent and thickness and how this has affected the amount of clouds over the Arctic. They found that there were increases in clouds in all months with the largest increases in the fall. This is when large differences in temperatures between the ocean surface and atmosphere enhanced the turbulent fluxes, which help to produce low-level clouds [*Klein et al.,* 2009]. Further studies are needed to better understand the relationships between sea ice concentration, surface fluxes and large-scale advection of heat and moisture, as well as cloud cover in the Arctic.

Chapter 7: Practical application: Prediction of ice accretion for shipping

7.1 Background

As the sea ice extent in the summer months continues to decrease, increased shipping through the Arctic Ocean could become a reality. Shipping could also occur in other months of the year as long as the Northwest Passage or other shipping routes were ice-free. Shipping or fishing can also occur near the sea ice edge throughout the year. There are many hazards to shipping through the Arctic, one of these being ice accretion. Ice accretion is the build up of ice on the ships as they travel in areas where certain meteorological conditions allow for this build up to occur (Figure 43). This build up of ice can cause ships to sink or capsize depending on the severity or the location of the ice build-up [*Jessup,* 1985].

Figure 43. An example of ice accretion (the build up of ice) on a ship. Image from www.marinetraffic.com.

Ice accretion occurs most commonly via freezing spray (wind on the water or ships on the waves), when advection fog (warm air overlying a cold surface) is present or when sea smoke (cold air overlying a warm surface) occurs, although this is the least common [*Overland et al.,* 1986]. Ice accretion on ships depends on many meteorological factors, such as subfreezing air temperatures, strong winds and SSTs that are less than 6°C [*Vasilyeva,* 1971]. It also depends on whether the ships are heading into the wind, their size and shape [*Stallabrass*, 1980].

Since the Arctic sea ice is undergoing changes in concentration, extent and changes in air and sea surface temperatures, it is important to study how the potential for

ice accretion on ships is changing in order to get an idea of where and when this will affect shipping in the future.

7.2 Methods

In order to study ice accretion potential and changes in the Arctic we adopted the algorithm from *Overland et al.* [1986], which uses the wind speed, near surface air temperature and SST and classifies the severity of the ice accretion. These levels are classified in Table 12. *Overland et al.* [1986] developed this algorithm using 195 recorded icing incidents on ships that occurred between 1979-1983 in Alaskan waters.

Table 12. Ice accretion levels from *Overland et al.* [1986].

Ice Accretion Level	Icing Rate (I)
Light	$I \leq 0.7$ cm hr^{-1}
Moderate	$0.7 < I \leq 2.0$ cm hr^{-1}
Heavy	$I > 2.0$ cm hr^{-1}

This algorithm is a statistical polynomial model with its coefficients determined from the ship observations.

$$I = AP + BP^2 + CP^3 \tag{46}$$

where I is the icing rate (cm hr^{-1}), A = 2.73 x 10^{-2}, B = 2.91 x 10^{-4}, and C = 1.84 x 10^{-6}.

$$P = \frac{V_a(T_f - T_a)}{[1 + 0.4(T_w - T_f)]} \tag{47}$$

where V_a is the wind speed (m s^{-1}), T_f is the freezing point of seawater (-1.8°C), T_a is the near surface air temperature (°C), and T_w is the sea surface temperature (°C).

The potential for ice accretion is calculated daily from January 1, 2003 until September 30, 2011. We utilized ECMWF Era-Interim 10 m wind speeds, surface air temperatures from AIRS, and SSTs from AMSR-E in order to calculate the potential icing rate.

7.3 Results

Figure 44 shows the ice accretion monthly climatology for 2003-2011. The potential for moderate to heavy ice accretion occurs mostly in the spring and winter months when both the air temperature and SSTs are close to or below freezing. The potential ice accretion is also higher during these months close to the sea ice edge. In the summer months, traveling through the Arctic by Russia, ice accretion will most likely not be an issue because there is little potential for heavy ice accretion. But there could be some problems traveling through the Northwest Passage and in the Canadian Archipelago in early autumn (Figure 45).

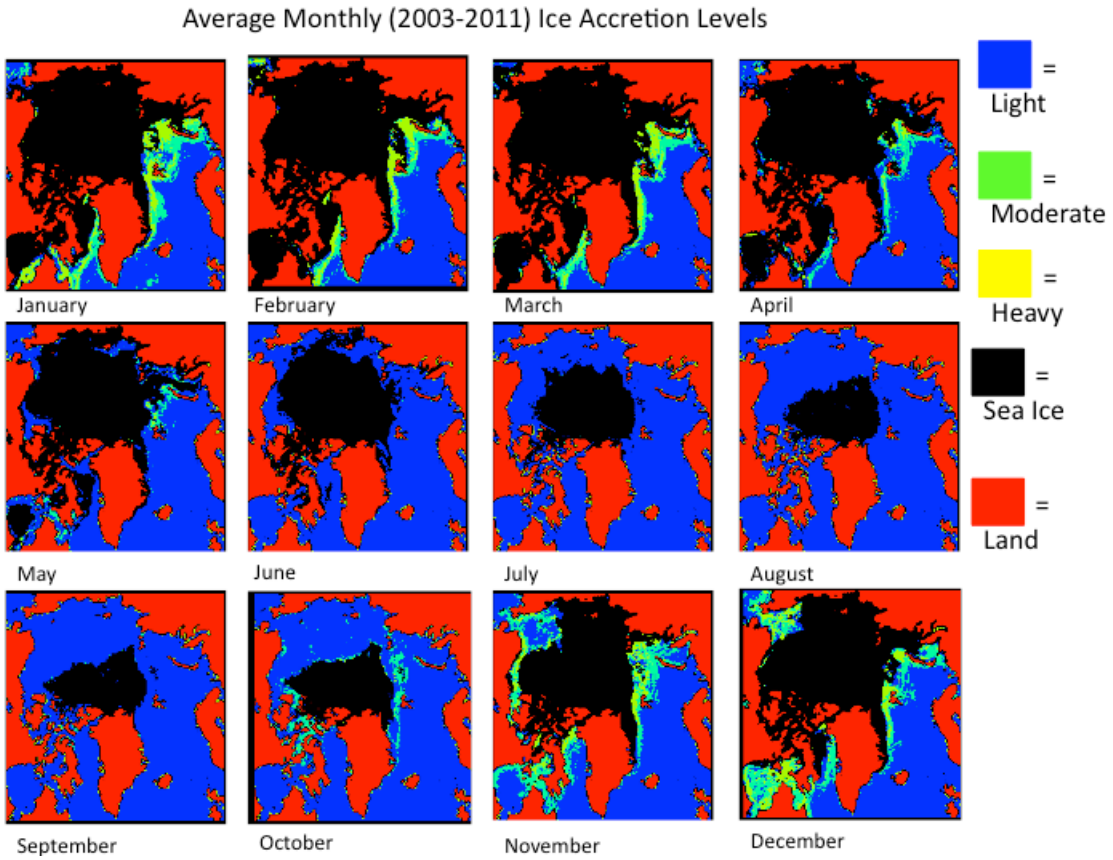

Figure 44. The average monthly climatology of the ice accretion levels (light, moderate and heavy; see Table 12) for the entire Arctic for the years 2003-2011.

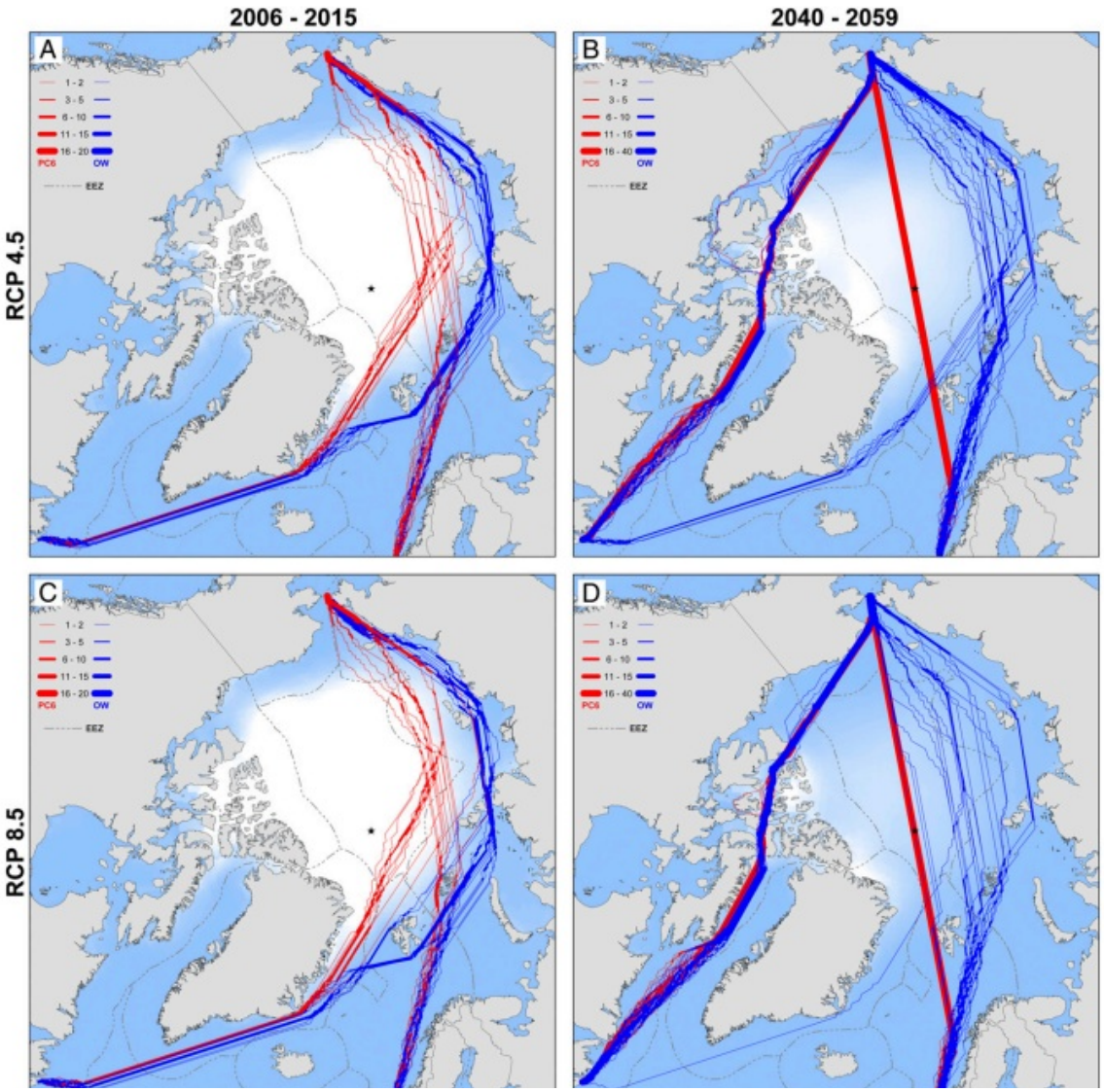

Figure 45. ATAM-derived optimal September navigation routes for hypothetical ships seeking to cross the Arctic Ocean between the North Atlantic (Rotterdam, The Netherlands and St. John's, Newfoundland) and the Pacific (Bering Straight) during consecutive years 2006-2015 (A and C) and 2040-2059 (B and D) as driven by ensemble-average GCM projections of sea ice concentration and thickness assuming RCPs 4.5 (A and B; medium-low radiation forcing) and 8.5 (C and D; high radiative forcing) climate change scenarios. Red lines indicate fastest available trans-Arctic routes for PC6 ships; blue lines indicate fastest available transits for common OW ships. Where overlap occurs, line weights indicate the number of successful transits using the same navigation route. Dashed lines indicate national 200-nm EEZ boundaries; white backdrops indicate period-average sea ice concentrations in 2006-2015 (A and C) and 2040-2059 (B and D). Figure from *Smith and Stephenson,* 2013.

There have also been changes to the frequency of the potential for low, moderate and heavy icing rates over the 9-year record due to changes occurring in the Arctic. Table 13 shows these trends.

Table 13. Monthly potential ice accretion frequency trends for the entire Arctic for low, moderate, and heavy ice accretion levels. Each number is a percentage (%/year).

Month	Low	Moderate	Heavy
January	-1.08	-0.04	0.12
February	-0.44	0.01	0.13
March	-0.33	0.09	0.16
April	-0.30	0.08	0.04
May	0.10	0.06	0.06
June	-0.99	0	0.06
July	-0.59	-0.03	0.09
August	-0.88	-0.03	0.11
September	-0.38	-0.06	0.06
October	-0.42	0.10	0.10
November	-0.35	0.10	0.15
December	0	-0.16	0.04

The potential for the low ice accretion frequency has been decreasing in all months except for a slight increase in May. On the other hand, the potential for heavy ice accretion is increasing in all months of the year, with smallest changes in the summer and largest in the winter months. The frequency of the potential for light ice accretion can occur about 50-70% of the time, whereas the potential for moderate and heavy only occurs 5% of the time. On a yearly basis the potential light ice accretion is decreasing 4.44% per year, the potential for moderate ice accretion is decreasing 0.2% per year, and the potential for heavy ice accretion is increasing 0.51% per year (Figure 46). The moderate and heavy ice accretion frequencies follow annual cycles similar to that of the moisture flux for the

Arctic. The smallest frequencies of these occur during the summer months and the largest occur over the winter months. The frequencies of the light ice accretion show no annual cycle.

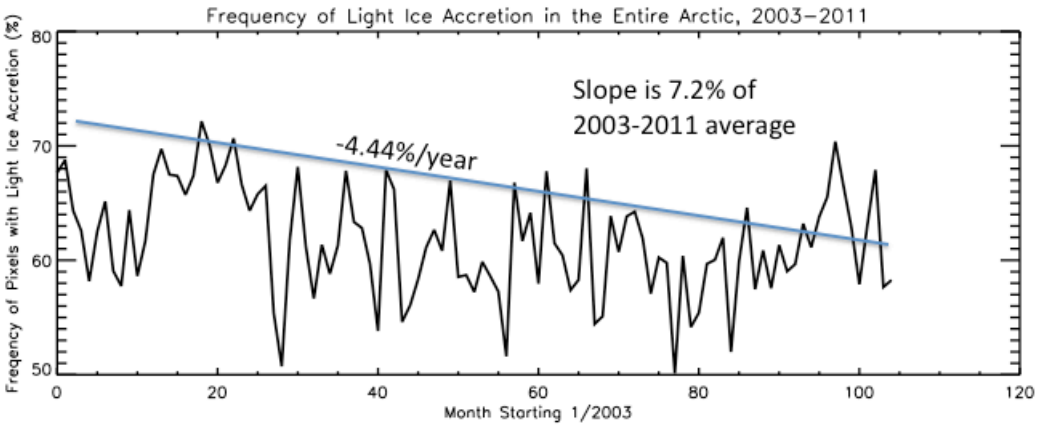

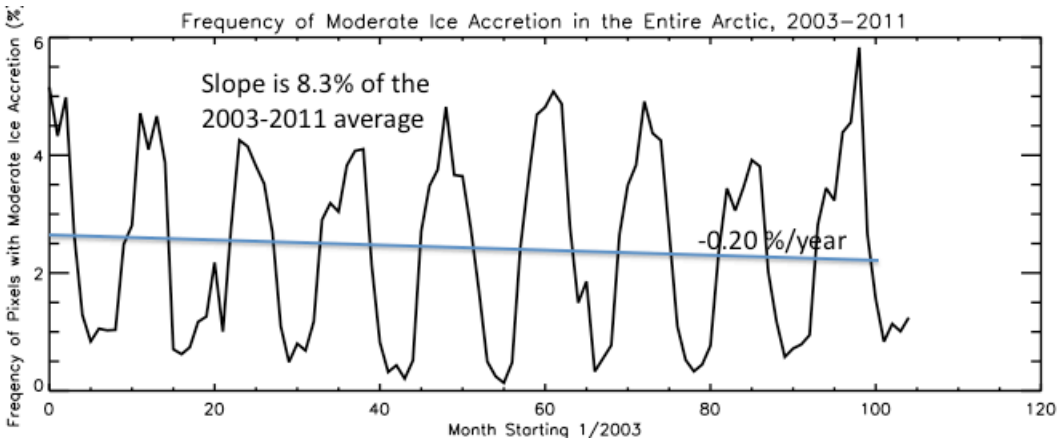

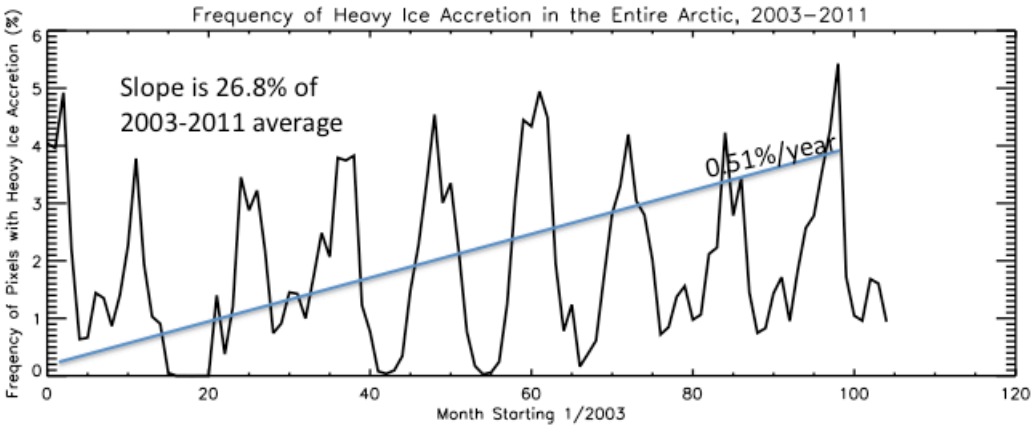

Figure 46. The monthly frequency for the potential for light (top), moderate (middle) and heavy (bottom) ice accretion from 2003-2011 for the entire Arctic. Slope is XX % of the 2003-2011 average corresponds either to the average light, moderate or heavy ice accretion, not the total ice accretion.

These changes are due to larger increases in the near surface air temperature in the winter months which create larger differences with the freezing point of seawater. These larger differences increase the icing rate so there is less potential for light accretion and a higher potential for heavy accretion. Thus, we expect to see a larger occurrence of heavy ice accretion events in the future, particularly in spring and winter months, as the sea ice extent continues to decrease and the near surface air temperature and SSTs continue to increase.

Chapter 8: Conclusions

This chapter provides a summary of the three main research aspects of this thesis. To begin we summarize the study of the Arctic SSTs and how they are changing between the years 1982-1999 and 2000-2009 after large reductions in sea ice extent. Next the moisture flux estimates of the North Water polynya, and error estimates, are summarized. To conclude we discuss moisture flux estimates over the entire Arctic, then interannual variability, and the impact of changes in sea ice concentration.

Sea surface temperatures (SSTs) from NOAA Optimum Interpolation ¼ Degree Sea Surface Temperature Analysis are analyzed over the entire Arctic between 1982-2009. SSTs during this record are increasing 0.03 °C/year in JJASO, however since 2000 this increase is accelerating at 2.4 times the rate between 1982-1999 and is driving the increases in SSTs over the 28-year record. Reasons for these large increases in SSTs between 2000-2009 are due to a shift in the Arctic oscillation to its positive phase and the Arctic dipole to its negative phase, which took place in the late 1990's and early 2000's. This shift in the winds forced the sea ice away from the Russian coast and out through the Fram Strait causing a reduction of sea ice cover to become less than 50% of the total area in JJASO. Larger areas of open water allow for more solar heat absorption, producing higher SSTs. Warmer SSTs delayed the freeze onset of the sea ice in autumn by 14.1 days/decade in 2000-2009 compared to 1.7 days/decade in 1982-1999.

The Arctic sea ice acts as a barrier between the ocean and lower atmosphere, reducing the exchange of heat and moisture. In recent years the ice pack has undergone

many changes, in particular a rapid reduction in sea ice extent and concentration in summer and autumn. Based on these observations, along with modeling studies, one would expect an increasing moisture flux. We estimate the daily moisture flux from 2003-2011 using geophysical data from multiple sensors onboard NASA's Aqua satellite, taking advantage of observations being collected at the same time and along the same track.

The fluxes were calculated using bulk aerodynamic formulas with the stability effects according to the Monin-Obukhov similarity theory. Input parameters were taken from three sources: air relative humidity, air temperature, and surface temperature from the Atmospheric Infrared Sounder (AIRS) on board NASA's Earth Observing System (EOS) Aqua satellite, sea ice concentration from the Advanced Microwave Scanning Radiometer for EOS (AMSR-E, also on board Aqua), and wind speed from the European Centre for Medium-Range Weather Forecasts ERA-Interim reanalysis. To test and evaluate the approach, we calculated the moisture fluxes from the North Water polynya during a series of events spanning 2003-2009. Our results show the progression of the moisture fluxes from the polynya during each event, as well as their atmospheric effects as the polynya refreezes. These results were compared to results from studies on other polynyas and the satellite data fall within one standard deviation of the moisture flux estimates from these independent studies. Although the estimated moisture fluxes over the entire study region from AIRS are smaller in magnitude than those from ERA-Interim, they are more accurate owing to improved temperature and relative humidity profiles and ice concentration estimates over the polynya. Average error estimates were calculated to be 5.56×10^{-3} g m^{-2} s^{-1}, only 25% of the average total moisture flux, thus suggesting that AIRS and AMSR-E can be used with confidence to study smaller-scale features in the

Arctic sea ice pack and can capture their atmospheric effects. These findings give confidence that satellite data may be used to study large-scale moisture flux variability over the entire Arctic Basin.

Our findings show the moisture flux, averaged over the entire Arctic, has had large interannual variations, with smallest fluxes in 2010, 2003 and 2004, and largest ones in 2007, 2008 and 2005 due to changes in sea ice concentrations and specific humidity differences over the record. Increases in air specific humidity tend to reduce the moisture flux, whereas the decrease in sea ice cover tends to increase the flux. Statistically significant seasonal decreasing trends are seen in December, January and February because of the dominating effect of increase in 2m air specific humidity increasing, reducing the surface-air specific humidity difference by -0.0547 kg/kg in the Kara/Barents Seas, E. Greenland Sea and Baffin Bay regions where there is some open water year round. Our results also show that the contribution of the sea ice zone to the total moisture flux (from the open ocean and sea ice zone) has increased by 3.6% because the amount of open water within the sea ice zone has increased by 4.3%. While the year-round open ocean areas (i.e. E. Greenland Sea and the Kara/Barents Seas) are seeing a decrease in the moisture flux, the less concentrated sea ice pack is seeing an increase. As the concentration of the sea ice continues to decrease, the moisture flux will increase and become a more dominant player in the total moisture flux.

Using Tara drifting station data we were able to re-evaluate our error estimates for the entire Arctic. We found an average error of 20.3%, which is an improvement from NCEP model analysis data, having an error of 26% [*Renfrew et al.,* 2002a] and ARCMIP regional scale models showing larger biases than the observed SHEBA observations

[*Tjernstrom et al.,* 2004]. Thus showing that our updated algorithm and Aqua data are an improved alternative to estimating the moisture flux in the Arctic.

Chapter 9: Future Work

In this chapter potential future research is described that utilizes the moisture flux data set created and validated in this thesis, as well further validation studies of other geophysical parameters from AIRS in the Arctic.

Accurate humidity data for the Arctic is vital for improved moisture flux estimates and as input to climate models. While we have shown that AIRS relative humidity improves the accuracy of moisture flux estimates, it is not free of errors. However the errors are lower than those from reanalysis studies, and therefore it is a more viable option than other reanalysis air humidity datasets and could improve climate models. AIRS humidity data over the open ocean, including polynyas, if large enough to be resolved by the model grid, have been assimilated only in ERA-Interim since April 2003, and only under clear-sky conditions [*Dee et al*., 2011]. However, the effect on the reanalysis data is small. The down-weighting of AIRS data is coupled with the fact that the ERA-Interim humidity analysis is highly constrained by other satellite observing systems [*McNally et al.,* 2006]. Doing further validations with AIRS against other reanalyses data and showing that AIRS is more accurate than these other data sets would be a strong argument to more extensively utilize AIRS data in model assimilations. Future work will include an analysis of other variables produced by AIRS such as surface temperature, 2m air temperature, etc.

In situ observations need to be used to demonstrate the improved accuracy of AIRS compared to other reanalysis data. These in situ observations need to be over both

the Arctic sea ice as well as over the Arctic Ocean to show that AIRS has better estimates over both of these surface types. Between 2003 and March, 2013 there were several aircraft campaigns collecting measurements of the relative humidity in the Arctic over both the sea ice and ocean. These low-level flights originate from the Svalbard region of the Arctic and are organized by the Alfred Wegener Institute in Bremerhaven, Germany. In addition to aircraft data, other alternatives include observations from the drifting ice station Tara from April – September 2007, although these are only over the sea ice. This was part of the DAMOCLES (Developing Arctic Modeling and Observation Capabilities for Long-Term Environmental Studies) project.

The Arctic sea ice concentration is decreasing and becoming thinner and is thus ice drift is increasing due to wind and ocean currents forcing. Since the North Water polynya is created from winds in the Smith Sound and ocean currents in Baffin Bay, the polynya could be affected by thinner, less concentrated ice. By looking at the occurrence, and size of the North Water polynya between 1979-present in the winter months, using SMMR and SSM/I ice concentration data, we will be able to determine if the polynya is becoming larger and more prevalent with the changing sea ice. More frequent and larger polynya events could cause larger moisture fluxes in the winter months, which alter the surface energy budget and local cloud formation, which in turn could warm the lower atmosphere near the polynya.

Understanding clouds and their interaction with the Arctic ice-ocean system is needed to improve climate models and to better model and understand cloud processes.

Determining if changes in the moisture flux in the Arctic are responsible for the creation of low, middle or high clouds will need to be done. One way to link these two processes would be to use a compositing technique described by *Schweiger et al.* [2008] using our moisture flux data set, cloud fraction data from MODIS and possibly low, middle and high cloud cover from ERA Interim for 2003-2011.

However, choosing a cloud data set has shown to provide multiple different outcomes of cloud cover trends in the Arctic. *Schweiger et al.* [2008], which used TOVS Polar Pathfinder data, found a decrease in low clouds and an increase in middle clouds in autumn, whereas *Kay and Gettelman* [2009], which used CloudSat and CALIOP data, found an increase in low-level cloud. *Schweiger et al.* [2008] assume that this middle cloud increase is caused by a deepening of the atmospheric boundary layer in the absence of sea ice. A verification of this could be done using our moisture flux data sets and boundary layer heights from ERA-Interim.

Since Arctic low-level clouds form in unstable boundary layers when cool air overlies a warm surface [*Key and Gettelman*, 2009], we expect to find that changes in the moisture flux occur with similar changes in low-level cloud amounts. Since the areal and temporal extent of the open water in the Arctic was found to have a large control on low-level clouds and the moisture flux [*Key and Gettelman*, 2009]. This is because the longer the sea surface is exposed, the larger the potential for the SSTs to increase. Higher SSTs create large temperature differences between the surface and air, which allows for increased moisture fluxes and hence more low clouds. Comparisons of our moisture flux estimates with yearly changes in low cloud data from Callipso may help to improve our knowledge of the affect that the moisture flux has on clouds in the Arctic.

Chapter 6.4.2 explained how the concentration of the sea ice zone (15-100% ice concentration) was causing changes to the moisture flux on a monthly and yearly basis. However, the study of the interaction between the moisture flux and the sea ice could be further enhanced by focusing on other aspects of the sea ice. One example would be to determine if the exchange of moisture has changed with the thinning of the sea ice pack. The thinner ice could have higher 2m specific humidity than the thicker ice, allowing for larger exchanges of moisture. The same could also be done for first-year and multi-year ice. Another important factor would be the change in melt and freeze onset and the subsequent melt season length of the sea ice and how this changes the magnitude of the moisture flux. An earlier melt onset and break up of the sea ice would allow for a longer period of time and also larger magnitudes of the moisture flux and the same is true for the freeze-up in the autumn. Looking at how an earlier melt onset and or later freeze onset affects the moisture flux is also necessary to better understand the ice-ocean system.

Chapter 10: References

AAgaard, K., and E. C. Carmack (1989), The role of sea ice and other fresh water in the Arctic Circulation, *J. Geophys. Res., 94,* C10, 14,485-14,498.

ACIA (2005), Arctic Climate Impact Assessment, Cambridge University Press, 1042p.

Alley, R. B. (1985), Resolved: The Arctic controls global climate change, In: Smith, W. O., and Grebmeier, J. M. (Eds), Arctic Oceanography: Marginal ice zones and continental shelves, *American Geophysical Union*, Washington, DC.

Andreas, E. L., C. A. Paulson, R. M. Williams, R. W. Lindsay, and J. A. Businger (1979), The turbulent heat flux from Arctic leads, *Boundary-Layer Meteorology,* 17, 57–91.

Andreas, E.L, and S. F. Ackley (1982), On the Differences in Ablation Seasons of Arctic and Antarctic Sea Ice, *Journal of Atmospheric Sciences*, 39, 440-447.

Andreas, E. L., and B. Murphy (1986), Bulk transfer coefficients for heat and momentum over leads and polynyas, *Q.J.R. Meteorological Society*, 105, 1,053-1,070.

Andreas, E. L. (1987), A theory for the scalar roughness and the scalar transfer coefficients over snow and ice, *Bound.-Layer Meteor.*, 38, 159-184.

Andreas, E. L., and B. A. Cash (1999), Convective heat transfer over wintertime leads and polynyas, *J. Geophys. Res*., 104(C11), 25,721 – 25,734.

Andreas, E. L. (2002), Parameterizing Scale Transfer over Snow and Ice: A Review, *J. Hydrometeorology,* 3, 417-432.

Andreas, E. L., R. E. Jordan, and A. P. Makhtas (2005), Parameterizing Turbulent Exchange Over Sea Ice: The Ice Station Weddell Results, *Boundary Layer Meteorology*, 114: 439-460.

Andreas, E. L., T. W. Horst, A. A. Grachev, P. O. G. Persson, C. W. Fairall, P. S. Guest, and R. E. Jordan (2010a), Parameterizating turbulent exhange over summer sea ice and the marginal ice zone, *Q. J. R. Meteorol. Soc.,* 136, 927-943, doi:10.1002/qj.618.

Andreas, E. L., P. O. G. Persson, R. E. Jordan, T. W. Horst, P. S. Guest, A. A. Grachev, and C. W. Fairall (2010b), Parameterizing Turbulent Exchange over Sea Ice in Winter, *J. Hydrometeorology,* 11, 87-104.

Andreas, E. L. (2011), A relationship between the aerodynamic and physical roughness of winter sea ice, *Q. J. R. Meteorol. Soc.,* 137, 1581-1588, doi:10.1002/qj.842.

Arbetter, T. E., A. H. Lynch, and D. A. Bailey (2004), Relationship between synoptic forcing and polynya formation in the Cosmonaut Sea: 1. Polynya climatology, *J. Geophys. Res*., 109, C04022, doi:10.1029/2003JC001837.

Aumann, H. H, M. T. Chahine, C. Gautier, M. D. Goldbery, E. Kalnay, L. M. McMillin, H. Revercomb, P. W. Rosenkranz, W. L. Smith, D. H. Staelin, L. L. Strow, and J. Susskind (2003), AIRS/AMSU/HSB on the Aqua Mission: Design, Science Objectives, Data Products, and Processing Systems, *IEEE Transactions on Geoscience and Remote Sensing,* 41, 253-264.

Badgely, F. J. (1966), Heat budget at the surface of the Arctic Ocean, in *Proceedings of the Symposium on the Arctic Heat Budget and atmospheric circulation*, J. O. Fletcher (ed.), Rand Corporation (RM – 5233 – NSF), 267-277.

Barber, D. G., R. Marsden, P. Minnett, G. Ingram, and J. Piwowar (2001a), Physical processes within the North Water (NOW) polynya, *Atmos. Ocean,* 39, 163-166.

Barber, D. G., J. M. Hanesiak, W. Chan, and J. Piwowar (2001b), Sea-ice and meteorological conditions in northern Baffin Bay and the North Water polynya between 1979 and 1996, *Atmosphere-Ocean,* 39, 343–359.

Beljaars, A. C. M., and A. A. M. Holtslag (1991), Flux parameterization over land surfaces for the atmospheric models, *J. Appl. Meteorol.,* 30, 327-341.

Boisvert, L. N., T. Markus, C. L. Parkinson, and T. Vihma (2012), Moisture fluxes derived from EOS Aqua satellite data for the North Water polynya over 2003-2009, *J. Geophys. Res.,* 117, D06119, doi:10.1029/2001JD016949.

Boisvert, L. N., T. Markus, and T. Vihma (2013), Moisture flux changes and trends for the entire Arctic in 2003-2011 derived from EOS Aqua data, *J. Geophys. Res.,* accepted.

Bromwich, D. H., and S.-H. Wang (2005), Evaluation of the NCEP-NCAR and ECMWF 15- and 40-Yr Reanalyses Using Rawinsonde Data from Two Independent Arctic Field Experiments, *Mon. Wea. Rev.,* 133, 3562-3578.

Businger, J. A., J. C. Wyngaard, Y. Izumi, and E. F. Bradley (1971), Flux-profile relationships, *J. Atmos. Sci.,* 28, 181-189.

Cavalieri, D. J., C. L. Parkinson, P. Gloersen, J. C> Comiso, and H. J. Zwally (1999), Deriving long-term time series of sea ice cover from satellite passive-microwave multisensor data sets, *J. Geophys. Res.,* 104, 15,803 – 15,814.

Cavalieri, D. J., and C. L. Parkinson, (2012), Arctic sea ice variability and trends, 1979-2010, *The Cryosphere*, 6, 881-889.

Cheng, Y., and W. Brutsaert (2005), Flux-profile relationships for wind speed and temperature in the stable atmospheric boundary layer, *Bound.-Layer Meteor.,* 114, 519-538.

Chepurin, G. A., and J. A. Carton (2012), Subarctic and Arctic sea surface temperature and its relation to ocean heat content 1982-2010, *J. Geophys. Res.,* 117(C6), doi:10.1029/2011JC007770.

Comiso, J. (2010), Polar Oceans from Space, Lawrence, A. M, and Hamilton, K. (Eds), Atmospheric and Oceanic Sciences Library, Vol. 41, Springer, NY.

Cronin M.F., C. W. Fairall, and M. J. McPhaden (2006), An assessment of buoy derived and numerical weather prediction surface heat fluxes in the tropical Pacific, *J. Geophys. Res.,* 111, C06038, doi:10.1029/2005JC003324.

Cullather R.I., D. H. Bromwich, M. C. Serreze (2000), The atmospheric hydrologic cycle over the Arctic basin from reanalyses. Part I: comparison with observations and previous studies, *Journal of Climate,* **13**: 923–937.

Curry, J. A., and E. E. Ebert (1992), Annual cycle of radiative fluxes over the Arctic ocean: Sensitivity to cloud optical properties, *J. Climate*, 5, 1267-1280.

Dare, R. A., and B. W. Atkinson (1999), Numerical modeling of atmospheric response to polynyas in the Southern Ocean sea ice zone, *J. Geophys. Res.,* 104, 16,691-16,708.

Dee D.P., S. M. Uppala, A. J. Simmons, P. Berrisford, P. Poli, S. Kobayashi, U. Andrae, M. A. Balmaseda, G. Balsamo, P. Bauer, P. Bechtold, A. C. M. Beljaars, L. van de Berg, J. Bidlot, N. Bormann, C. Delsol, R. Dragani, M. Fuentes M, A. J. Geer,

L. Haimberger, S. B. Healy, H. Hersbach, E. V. Hölm, L. Isaksen, P. Kåallberg, M. Köhler , M. Matricardi, A. P. McNally, B. M. Monge-Sanz, J.-J. Morcrette, B.-K. Park, C. Peubey, P. de Rosnay, C. Tavolato, J.-N. Thepaut, and F. Vitart (2011), The ERA-Interim reanalysis: configuration and performance of the data assimilation system, *Q. J. R. Meteorol. Soc.,* 137, 553–597, doi:10.1002/qj.828.

Dessler, A. E., Z. Zhang, and P. Yang (2008), Water-vapor climate feedback inferred from climate fluctuations, 2003-2008, *Geophys. Res. Lett.,* 35, L20704, doi:10.1029/2008GL035333.

Dethleff, D. (1994), Polynyas as a possible source for enigmatic Bennett Island atmospheric plumes, Johannessen, O.M., Muench, R.D., Overland, J.E. (Eds.), In: Polar Oceans and their Role in Shaping the Global Environment. American Geophysical Union, Washington, DC, pp. 475–483.

Dethloff, K., C. Abegg, A. Rinke, I. Hebestadt and V. F. Romanov (2001), Sensitivity of Arctic climate simulations to different boundary-layer parameterizations in a regional climate model, *Tellus,* 53A:1-26.

Dey, B., H. Moore, and A. Gregory (1979), Monitoring and mapping sea ice breakup and freeze-up of Arctic Alaska from satellite data, *Arctic and Alpine Research*, 11, 229-242.

Dyer A. J. and B. B. Hicks (1970), Flux-gradient relationships in the constant flux layer, *Quart. J. Roy. Meteorol. Soc.,* 96, 715-721.

Dyer, A. J. (1974), A review of flux-profile relationships, *Bound.-Layer Meteor.,* 7, 363-372.

Dyer, A. J. and E. F. Bradley (1982), An alternative analysis of flux-gradient

relationships at the 1976 ITCE, *Bound.-Layer Meteor.,* 22, 3-19.

Eastman, R., and S. G. Warren (2010), Interannual Variations of Arctic Cloud Types in Relation to Sea Ice, *J. Climate*, 23, 4216-4232.

Fairall, C. W, E. F. Bradley, D. P. Rogers, J. B. Edson, and G. S. Young (1996), Bulk parameterization of air-sea fluxes for Tropical Ocean-Global Atmosphere Coupled-Ocean Atmosphere Response Experiment, *J. Geophys. Res.,* 101, 3747-3764.

Fishbein, E., S-Y. Lee, E. Manning, E. Maddy, and W.W. McMillan (2011), AIRS/AMSU/HSB Version 5 Level 2 Product Levels, Layers and Trapezoids, E. T. Olsen (*Eds.),* Jet Propulsion Laboratory, Pasadena, California, USA.

Forrer, J., and M. W. Rotach (1997), On the turbulence structure in the stable boundary layer over the Greenland ice sheet, *Bound.-Layer Meteor.,* 85, 111-136.

Francis, J. A. (2002), Validation of reanalysis upper-level winds in the Arctic with i ndependent rawinsonde data, *Geophys. Res. Lett.,* 29, 1315, doi:10.1029/2001GL014578.

Fujitani, T. (1981), Direct measurement of turbulent fluxes over the sea during AMTEX, *Papers in Meteorol. and Geoph.,* 32, 119-134.

Garratt, J. R. (1992), The Atmopsheric Boundary Layer, Cambridge University Press, 316pp.

Gates, W. L. (1992), AMIP: The Atmospheric Model Intercomparison Project, *Bull. Amer. Meteor. Soc.,* 73, 1962-1970.

Gettelman, A., W. D. Collins, E. J. Fetzer, A. Eldering, F. W. Irion, P. B. Duffy, and G.

Bala (2006), Climatology of Upper-Tropospheric Relative Humidity from the Atmospheric Infrared Sounder and Implications for Climate, *J. Climate*, 19, 6,104-6,121.

Gloersen, P., W. J. Campbell, D. J. Cavalieri, J. C. Comiso, C. L. Parkinson, and H. J. Zwally (1992), Arctic and Antarctic sea ice, 1978-1987: Satellite passive-microwave observations and analysis. *NASA Special Publications*, SP-511, 290 pp.

Grachev, A. A., E. L. Andreas, C. W. Fairall, P. S. Guest, and P. O. G. Persson (2007), SHEBA flux-profile relationships in the stable atmospheric boundary layer, *Bound-Layer Meteor*., 124, 315-333.

Grotefendt, K., K. Logemann, D. Quadfasel, and S. Ronski (1998), Is the Arctic Ocean warming?, *J. Geophys. Res.*, 103(C12), 27679-27687, doi:10.1029/98JC02097.

Gultepe, I., G. A. Isaac, A. Williams, D. Marcotte, and K. B. Strawbridge (2003), Turbulent heat fluxes over leads and polynyas, and their effects on Arctic clouds during FIRE.ACE: Aircraft observations for April 1998, *Atmos. Ocean*, 41, 15 – 34.

den Hartog, G., R. J. Smith, D. R. Anderson, D. R. Topham, and R. G. Perkin (1983), An investigation of a polynya in the Canadian Archipelago, 3, Surface heat flux, *J. Geophys. Res.*, 88, 2911-2916.

Heinrichs, J. F., D. J. Cavalieri, and T. Markus (2006), Assessment of AMSR-E Sea Ice Concentration Product at the Ice Edge Using RADARSAT-1 and MODIS Imagery, *IEEE Transactions of Geoscience and Remote Sensing*, 44, 11, 3070-3080.

Högström, U. (1988), Non-dimensional wind and temperature profiles in the atmospheric surface layer: A re-evaluation, *Bound.-Layer Meteorol*., 42, 55–78.

Holtslag, A. A. M., and H. A. R. de Bruin (1988), Applied modeling of the nighttime surface energy balance over land, *J. Appl. Meteorol*., 37, 689– 704.

Intrieri, J., C. W. Fairall, M. D. Shupe, P. O. G. Persson, E. L. Andreas, P. S. Guest, and R. E. Moritz (2002), Annual Cycle of Arctic Surface Cloud Forcing at SHEBA, *J. Geophys. Res*. 107, 8039, doi: 10.1029/2000JC000439.

IPCC (2001), Climate Change 2001: The Scientific Basis, Contribution of Working Group I to the Second Assessment Report of the Intergovernmental Panel on Climate Change. J. T. Houghton, Y. Ding, D. J. Griggs, M. Noguer, P. J. van der Linden, X. Dai, K. Kaskell and C. A. Johnson (eds.), Intergovernmental Panel on Climate Change, *Cambridge University Press,* 881 pp.

Ito, H., and F. Muller (1977), Horizontal movement of fast ice in the North Water area, *J. Glaciology*, 19, 547-554.

Ito, H. (1982), Wind through a channel: Surface wind measurements in Smith Sound and Jones Sound in northern Baffin Bay, *J. Applied Meteorology*, 21, 1,053-1,062.

Ito, H. (1985), Decay of the sea ice in the North Water area: Observation of ice cover in Landsat imagery, *J. Geophys. Res*., 90, 8,102-8,110.

Jakobson, E. and T. Vihma (2010), Atmospheric moisture budget over the Arctic on the basis of the ERA-40 reanalysis. *Int. J. Climatol.*, **30**: 2175–2194, DOI: 10.1002/joc.2039.

Jakobson, E., T. Vihma, T. Palo, L. Jakobson, H. Keernik, and J. Jaagus (2012), Validation of atmospheric reanalyses over the central Arctic Ocean, Geophys. Res. Lett., 39, L10802, doi:10.1029/2012GL051591.

Jessup, R. G. (1985), Forecasting techniques for ice accretion on different types of

marine structures, including ships, platforms and coastal facilities, *Marine Meteorology and Related Oceanography Activities,* Rep. 15, WMO, Canada.

Kay, J. E., T. L'Ecuyer, A. Gettelman, G. Stephens, and C. O'Dell (2008), The contribution of cloud and radiation anomalies to the 2007 Arctic sea ice extent minimum, *Geophys. Res. Lett., 35,* L08503, doi: 10.1029/2008GL033451.

Kay, J. E., and A. Gettelman (2009), Cloud influence on and response to seasonal Arctic sea ice loss, *J. Geophys. Res.,* 114, D18204, doi:10.1029/2009JD011773.

Kay, J. E., M. M. Holland, C. M. Bitz, E. Blanchard-Wrigglesworth, A. Gettelman, A. Conley, and D. Bailey (2012), Influences of the local feedbacks and northward heat transport on the equilibrium Arctic climate response to increased greenhouse gas forcing, *J. Climate,* 25, doi:10.1175/JCLI-D-11-00622.1.

Klein, S. A., et al. (2009), Intercomparision of model simulations of mixed-phase clouds observed during the ARM Mixed-Phase Cloud Experiment: Part I. Single-layer cloud, *Q. J. R. Meteorol. Soc.,* 641, 979-1002, doi:10.1002/qj.416.

Klipp, C. L., and L. Mahrt (2004), Flux-gradient relationship, self-correlation and intermittency in the stable boundary layer, *Quart. J. Roy. Meteorol. Soc.,* 130, 2087-2103.

Kurtz, D. D. and D. H. Bromwich (1985), A recurring, atmospherically forced polynya in Terra Nova Bay. *In* Jacobs, S. S., *ed., Oceanology of the Antarctic continental shelf,* Washington, DC, American Geophysical Union, 177-201. (Antarctic Research Series 43.)

Kurtz, N. T., T. Markus, D. J. Cavalieri, L. C. Sparling, W. B. Krabill, A. J. Gasiewski,

and J. G. Sonntag (2009), Estimation of sea ice thickness distributions through the combination of show depth and satellite laser altimetry data, *J. Geophys. Res.,* 114, C10007, doi:10.1029/2009JC005292.

Kurtz, N. T., T. Markus, S. L. Farrell, D. L. Worthen, and L. N. Boisvert (2011), Observations of recent Arctic sea ice volume loss and its impact on ocean-atmosphere energy exchange and ice production, *J. Geophys. Res.,* 116, C04015, doi:10.1029/2010JC006235.

Kwok, R., H. J. Zwally and D. Yi (2004), ICESat observations of Arctic sea ice: A first look, *Geophys. Res. Lett.,* 31, L16401, doi:10.1029/2004Gl020309.

Kwok, R., and D. A. Rothrock (2009), Decline in Arctic sea ice thickness from submarine and ICESat records: 1958-2008, *Geophys. Res. Lett.,* 36, L15501, doi:10.1029/2009GL039035.

Large, W. G. and S. Pond (1980), Open ocean momentum flux measurements in moderate to strong winds, *J. Phys. Oceanogr.,* 11, 324-336.

Launiainen, J. (1983), Parameterization of the water vapour flux over a water surface by the bulk aerodynamic method, *Annales Geophysicae*, 1, 481-492.

Launiainen, J., and T. Vihma (1990), Derivation of turbulent surface fluxes – An iterative flux-profile method allowing arbitrary observing heights, *Environmental Software*, 5, 113-124.

Launiainen, J., and T. Vihma (1994), On the surface heat fluxes in the Weddell Sea, *The Polar Oceans and Their Role in Shaping the Global Environment*, Nansen Centennial Volume, Geophysical Monogram Series, 85, edited by O.M.

Johannessen, R. Muench, and J.E. Overland, pp., 399-419, AGU, Washington, D.C.

Laxon, S. W., K. A. Giles, A. L. Ridout, D. J. Wingham, R. Willatt, R. Cullen, R. Kwok, A. Schweiger, J. Zhang, C. Haas, S. Hendricks, R. Krishfield, N. Kurtz, S. Farrell, and M. Davidson (2013), CryoSat-2 estimates of Arctic sea ice thickness and volume, *Geophys. Res. Lett., 40,* doi:10.1002/grl.50193.

Lupkes, C., T. Vihma, E. Jakobson, G. Konig-Langlo, and A. Tetzlaff (2010), Meteorological observations from ship cruises during summer to the central Arctic: A comparison with reanalysis data, *Geophys. Res. Lett.,* 37, L09810, doi:10.1029/2010GL042724.

Lüpkes, C., V.M. Gryanik, J. Hartmann, and E.L Andreas (2012), A parametrization, based on sea ice morphology, of the neutral atmospheric drag coefficients for weather prediction and climate models, J. Geophys. Res., 117, D13112, doi:10.1029/2012JD017630.

Mailhot, J., A. Tremblay, S. Bélair, I. Gultepe, and G. A. Isaac (2002), Mesoscale simulation of surface fluxes and boundary layer clouds associated with a Beaufort Sea polynya, *J. Geophys. Res.,* 107, doi:10.1029/2000JC000429.

Markus, T., and B.A. Burns (1995), A method to estimate subpixel-scale coastal polynyas with satellite passive microwave data, *J. Geophys. Res.,* 100, 4,473–4,487.

Markus, T., C. Kottmeier, and E. Fahrbach (1998), Ice Formation in Coastal Polynyas in the Weddell Sea and their impact on oceanic salinity, Jeffries, M.O. (Ed.), In: Antarctic sea ice: Physical processes, interactions, and variability. Antarctic Research Series, AGU, Washington DC, 74, 273-292.

Markus, T., and D. J. Cavalieri (2000), An enhancement of the NASA Team sea ice algorithm. *IEEE Transactions on Geoscience and Remote Sensing,* 38, 1,387-1,398.

Markus, T., J. C. Stroeve, and J. Miller (2009), Recent changes in Arctic sea ice melt onset, freezeup, and melt season length, *J. Geophys. Res.,* 114, C12024, doi:10.1029/2009JC005436.

Martin, S., and D. J. Cavalieri (1989), Contributions of the Siberian Shelf polynyas to the Arctic Ocean intermediate and deep water, *J. Geophys. Res.,* 94, 12,725-12,738.

Massom, R.A., R. T. Harris, K. J. Michael, and M. J. Potter (1998), The distribution and formative processes of latent-heat polynyas in East Antarctica, *Annals of Glaciology*, 27, 420–426.

Maykut, G. A. (1978), Energy exchange over young sea ice in the Central Arctic, *J. Geophys. Res.,* 83, 3646–3658.

Maykut, G. A. (1982), Large-Scale Heat Exchange and Ice Production in the Central Arctic, *J. Geophys. Res.,* 87(C10), 7971-7984, doi:10.1029/JC087iC10p07971.

McNally A. P., P.D. Watts, J. A. Smith, R. Engelen, G. A. Kelly, J. N. Thepaut and M. Matricardi (2006), The assimilation of AIRS radiance data at ECMWF, *Q. J. R. Meteorl. Soc.*, 132: 935-957.

Minnett, P. J., and E. L. Key (2007), Meteorology and atmosphere – Surface coupling in and around polynyas, Smith, W.O.J., Barber, D.G. (Eds.), In: *Polynyas: Windows to the World*, Elsevier, Amsterdam.

Monin, A. S. and A. M. Obukhov (1954), Dimensionless characteristics of turbulence in the surface layer, *Trudy Geofiz. Inst. Akad. Nauk.,* 24, 163-187.

Morales Maqueda, M. A., A. J. Willmott and N. R. T. Biggs (2004), Polynya Dynamics: A review of observations and modeling, *Rev. Geophys., 42*, RG1004, doi:10.1029/2002RG000116.

Nghiem, S. V., I. G. Rigor, D. K. Perovich, P. Clemente-Colon, J. W. Weatherly, and G. Neumann (2007), Rapid reduction of Arctic perennial sea ice, *Geophys. Res. Lett.,* 34, L19504, doi:10.1029/2007GL031138.

Obukhov, A. M. (1971), Turbulence in an atmosphere with a non-uniform temperature (English Translation), *Bound.-Layer Meteor.,* 2, 7-29.

Olsen, E. T. (Ed.) (2011), AIRS/AMSU/HSB version 5 level 2 product levels, layers and trapezoids, report, Jet Propul. Lab., Pasadena, Calif.

Overland, J. E., C. H. Pease, R. W. Preisendorfer, and A. L. Comiskey (1986), Prediction of Vessel Icing, *J. Climate and Applied Meteor.,* 25, 1,793-1,806.

Overland, J., and M. Wang (2010), Large scale atmospheric circulation changes are associated with the recent loss of Arctic sea ice, Tellus, Ser. A, 62, 1–9.

Palm, S. P., S. T. Strey, J. Sphinhirne, and T. Markus (2010), Influence of Arctic sea ice extent on polar cloud fraction and vertical structure and implications for regional climate, *J. Geophys. Res.,* 115, D21209, doi:10.1029/2010JD013900.

Parkinson, C. L, D. J Cavalieri, P. Gloersen, H. J. Zwally, and J. C. Comiso (1999), Arctic sea ice extents, areas, and trends, 1978-1996, *J. Geophys. Res.,* 104, C9, 20,837 – 20,856.

Parkinson, C. L. (2003), Aqua: An Earth-observing satellite mission to examine water and other climate variables, *IEEE Transactions on Geoscience and Remote Sensing,* 41(2), 173-183.

Parkinson, C. L., and D. J. Cavalieri (2008), Arctic sea ice variability and trends, 1979-2006, *J. Geophys. Res.,* 113, C07003, doi:10.1029/2007JC004558.

Paulson, C. A. (1970), The mathematical representation of wind speed and temperature profiles in the unstable atmospheric surface layer, *J. Appl. Meteor.,* 9, 857-861.

Pease, C. H. (1987), The size of wind-driven coastal polynyas, *J.Geophys. Res*., 92, 7,049–7,059.

Perovich, D. K., B. Light, H. Eicken, K. F. Jones, K. Runciman, and S. V. Nghiem (2007), Increasing solar heating of the Arctic Ocean and adjacent seas, 1979-2005: Attribution and role in the ice-albedo feedback, *Geophys. Res. Lett.,* 34, L19505, doi:10.1029/2007GL031480.

Perovich, D. K., J. A. Richter-Menge, K. F. Jones and B. Light (2008), Sunlight, water and ice: Extreme Arctic sea ice melt during the summer of 2007, *Geophys. Res. Lett., 35,* L11501, doi:10.1029/2008GL034007.

Pinto, J.O., J. A. Curry, and K. L. McInnes (1995), Atmospheric convective plumes emanating from leads 1. Thermodynamic structure, *J. Geophys. Res.,* 100, 4,621-4,631.

Pinto, J. O., and J. A. Curry (1995), Atmospheric convective plumes emanating from leads 2. Microphysical and radiative processes, *J. Geophys. Res.,* 100, 4,633–4,642.

Pinto, J. O., J. A. Curry, A. H. Lynch, and P. O. G.Persson (1999), Modeling clouds and radiation for the November 1997 period of SHEBA using a column climate model, *J. Geophys. Res.,* 104, 6,661 – 6,678.

Pinto, J. O., A. Alam, J. A. Maslanik, J. A. Curry, and R. S. Stone (2003), Surface

characteristics and atmospheric footpring of springtime Arctic leads at SHEBA, *J. Geophys. Res.,* 108, doi:10.1029/2000JC000473.

Polyakov, I. V., J. E. Walsh and R. Kwok (2012), Recent changes of Arctic multiyear sea ice coverage and likely causes, *Bull. American Meteor. Soc., 93,* doi:10.1075/BAMS-D-11-00070.1.

Poulos, G. S. and S. P. Burns (2003), An evalulation of bulk Ri-based surface layer flux formulas for stable and very stable conditions with intermittent turbulence, *J. Atmos. Sci.,* 60, 2523-2537.

Raddatz, R. L., M. G. Asplin, L. Candlish, and D. G. Barber (2010), General Characteristics of the Atmospheric Boundary Layer Over a Flaw Lead Polynya Region in Winter and Spring, *Boundary-Layer Meteorol.,* 138, 321-335, doi:10.1107/s10546-010-9557-1.

Randall, D., J. Curry, D. Battisti, G. Flato, R. Grumbine, S. Hakkinen, D. Martinson, R. Preller, J. Walsh and J. Weatherly (1997), Status of and Outlook for Large-Scale Modeling of Atmosphere-Ice-Ocean Interactions in the Arctic, *Bull. Amer. Meteor. Soc.,* 197-219.

Renfrew, I. A., J. C. King, and T. Markus (2002), Coastal polynyas in the southern Weddell Sea: Variability of the surface energy budget, *J. Geophys. Res*., 107, doi:10.1029/2000JC000720.

Renfrew, I. A., G. W. K. Moore, P. S. Guest, and K. Bumke (2002a), A comparison of the surface layer and surface turbulent flux observations over the Labrador Sea with ECMWF Analyses and NCEP reanalyses, *J. Phys. Oceanogr.,* 32, 383-400, doi: http://dx.doi.org/10.1175/1520-0485(2002)032<0383:ACOSLA>2.0.CO;2.

Reynolds, R. W., T. M. Smith, C. Liu, D. B. Chelton, K. S. Casey and M. G. Schlax (2007), Daily High-Resolution-Blended Analyses for Sea Surface Temperature, *J. Climate, 20,* doi: 10.1175/2007JCLI1824.1.

Rigor, I. G., J. M. Wallace, and R. L. Colony (2002), Response of sea ice to the Arctic Oscillation, *J. Climate*, 15, 2,648-2,663.

Rinke, A., C. Melsheimer, K. Dethloff, and G. Heygster (2009), Arctic total water vapor: Comparison of regional climate simulations with observations, and simulated decadal trends, *J. Hydrometeorol.*, 10, 113–129, doi:10.1175/2008JHM970.1.

Roberts, A., I. Allison, and V. I. Lytle (2001), Sensible- and latent-heat-flux estimates over the Mertz Glacier polynya, East Antarctica, from in-flight measurements, *Annals of Glaciology,* 33, 377-384.

Serreze, M. C., J. D. Kahl, and R. C. Schnell (1992), Low‐level temperature inversions of the Eurasian Arctic and comparisons with Soviet drifting station data, J. Clim., 5, 615–629.

Serreze, M. C., A. P. Barrett, A. G. Slater, M. Steele, J. Zhang, and K. E. Trenberth (2007), The large-scale energy budget of the Arctic, *J. Geophys. Res.,* 112, D11122, doi:10.1029/2006JD008230.

Serreze, M. C., A. P. Barrett, and J. Stroeve (2012), Recent changes in tropospheric water vapor over the Arctic as assessed from radiosondes and atmospheric reanalyses, J. Geophys. Res., 117, D10104, doi:10.1029/2011JD017421.

Schmitt, K. F., C. A. Friehe, and C. H. Gibson (1979), Structure of marine surface layer turbulence, *J. Atmos. Sci.,* 36, 602-618.

Schneider, W., and G. Budeus (1995), On the generation of the Northeast Water polynya,

J. Geophys. Res., 100, 4,269-4,286.

Schnell, R. C., R. G. Barry, M. W. Miles, E. L. Andreas, L. F. Radke, C. A. Brock, M. P. McCormick, and J. L. Moore (1989), Lidar detection of leads in Arctic sea ice, *Letters to Nature*, 339, 530 – 532.

Screen, J. A., and I. Simmonds (2010a), Erroneous Arctic Temperature Trends in the ERA-40 Reanalysis: A closer look, *J. Climate,* 24, 2620-2627.

Screen, J. A., and I. Simmonds (2010b), The central role of diminishing sea ice in recent Arctic temperature amplification, *Nature*, 464, 1334–1337, doi:10.1038/nature09051.

Screen, J. A., and I. Simmonds (2010c), Increasing fall-winter energy loss from the Arctic Ocean and its role in Arctic temperature amplification, *Geophys. Res. Lett*., 37, L16707, doi:10.1029/2010GL044136.

Smith, L. C., and S. R. Stephenson (2013), New Trans-Arctic shipping routes navigable by midcentury, *Proceedings of the National Academy of Sciences of the United States of America,* www.pnas.org/doi/10.1073/pnas.1214212110.

Smith, S. D., R. J. Anderson, G. den Hartog, D. R. Topham, and R. G. Perkin (1983), An investigation of a polynya in the Canadian Archipelago, 2, Structure of turbulence and sensible heat flux, *J. Geophys. Res.,* 88, 2,900-2,910.

Smith, S. D., R. D. Muench, and C. H. Pease (1990), Polynyas and leads: An overview of physical processes and environment, *J. Geophys. Res.,* 95, 9,461–9,479.

Stallabrass, J. R. (1980), Trawler icing: A complication of work done at N.R.C. Mech. Eng. Rep. MD-56, N.R.C. No. 19372, National Research Council, Ottawa, Canada.

Steele, M., W. Ermold, and J. Zhang (2008), Arctic Ocean surface warming trends over the past 100 years, *Geophys. Res. Lett.,* 35, L02614, doi:10.1029/2007GL031651.

Steele, M., J. Zhang and W. Ermold (2010), Mechanisms of summertime upper Arctic Ocean warming and the effect on sea ice melt, *J. Geophys. Res., 115,* C11004, doi:10.1029/2009JC005849.

Stirling, I. (1980), The biological importance of polynyas in the Canadian Arctic, *Arctic*, 33, 303-315.

Stouffer, R. J., J. Yin, J. M. Gregory, K. W. Dixon, M. J. Spelman, W. Hurlin, A. J. Weaver, M. Eby, G. M. Flato, H. Hasumi, A. Hu, J. H. Jungclaus, I. V. Kamenkovich, A. Levermann, A. Sokolov, G. Vettoretti, and S. L. Weber (2006), Investigating the causes of the response of the Thermohaline Circulation to past and future climate changes, *J. Climate, 19*, 1,365-1,387.

Stringer, W. J., and J. E. Groves (1991), Location and Areal Extent of Polynyas in the Bering and Chukchi Seas, *Arctic*, 44, 164-171.

Stroeve, J.C., M. M Holland, W. Meier, T. Scambos, and M. Serreze (2007), Arctic sea ice decline: Faster than forecast, *Geophys. Res. Lett.,* 34, L09501, doi:10.1029/2007GL029703.

Stroeve, J.C., M.C. Serreze, M.M. Holland, J.E. Kay, J. Maslanik, and A.P. Barrett (2012), The Arctic's rapidly shrinking sea ice cover: a research synthesis, *Climatic Change,* 110, 1005-1027, doi:10.1007/s10584-011-0101-1.

Susskind, J. and J. Blaisdell (2010), AIRS/AMSU/HSB Version 5 Level 2 Quality Control and Error Estimation, E. T. Olsen (Eds.), Jet Propulsion Laboratory, California, USA.

Tastula, E.-M., and T. Vihma (2011), WRF model experiments on the Antarctic atmosphere in winter, *Mon. Wea. Rev.,* 139, 1279-1291, doi:10.1175/2010MWR3478.1

Tastula, E.-M, T. Vihma, E. L. Andreas, and B. Galperin (2013). Validation of the diurnal cycles in atmospheric reanalyses over Antarctic sea ice. J. Geophys. Res., in press.

Tisler, P., T. Vihma, G. Müller, and B. Brümmer (2008), Modelling of warm-air advection over Arctic sea ice, *Tellus,* 60(4), 775-788.

Tjernström M., M. Zagar, G. Svensson, J. J. Cassano, S. Pfeifer, A. Rinke, K. Wyser, K. Dethloff, C. Jones, T. Semmler, and M. Shaw (2005), Modeling the Arctic boundary layer: an evaluation of six ARCMIP regional-scale models using data from the SHEBA project, *Bound.-Lay. Meteoro,* **117**: 337–381, doi: 10.1007/s10546-004-7954-z.

Tobin, D.C., H. E. Revercomb, R. O. Knuteson, B. M. Lesht, L. L. Strow, S. E. Hannon, W. F. Feltz, L. A. Moy, E. J. Fetzer, and T. S. Cress (2006), Atmospheric Radiation Measurement site atmospheric state best estimates for Atmospheric Infrared Sounder temperature and water vapor retrieval validation, *J. Geophys. Res., 111,* D09S14, doi:10.1029/2005JD006103.

Topham, D. R., R. G. Perkin, S. D. Smith, A. J. Anderson, and G. den Hartog (1983), An investigation of a polynya in the Canadian Archipelago, 1, Introduction and oceanography*, J. Geophys. Res.,* 88, 2,888-2,988.

Vasilyeva, G. V. (1971), Hydrometeorological conditions of the icing of sea-going ships, *Tr. Gidromettsentra SSR,* 87, 82-92.

Walsh, J. E. and W. L. Chapman (1998), Arctic cloud-radiation-temperature

associations in observational data and atmospheric reanalyses, *J. Climate*, 11, 3,030-3,045.

Walter, B. A. (1989), A study of the planetary boundary layer over the polynya downwind of St. Lawrence Island in the Bering Sea using aircraft data, *Boundary-Layer Meteorology,* 48, 255–282.

Wentz, F. and T. Meissner, (2000), AMSR Ocean Algorithm, Algorithm Theoretical Basis Document, Version 2, Santa Rosa, California USA: Remote Sensing Systems.

Willmott, A. J., M. A. Morales Maqueda, and M. S. Darby (1997), A model for the influence of wind and oceanic currents on the size of a steady-state latent heat coastal polynya. *J. Physical Oceanography*, 27, 2,256 – 2,275.

Curriculum Vitae

Name: Linette Nicole Boisvert

Permanent Address: 9914 Gable Ridge Terrace Apt. A, Rockville, MD 20850

Degree and date to be conferred: Ph.D., August 1, 2013.

Date of Birth: December 16, 1985

Place of Birth: Rockville, MD

Secondary Education: Watkins Mill High School, Gaithersburg, MD, 2004.

Education:

B.S. Environmental Science, Minor: Mathematics, University of Maryland Baltimore County, Baltimore, MD, 2008.

M.S. Atmospheric and Oceanic Sciences, University of Maryland, College Park, MD, 2012.

Ph.D. Atmospheric and Oceanic Sciences, University of Maryland, College Park, MD, 2013.

Professional Publications:

Kurtz, N. T., T. Markus, S. L. Farrell, D. L. Worthen, and L. N. Boisvert (2011), Observations of recent Arctic sea ice volume loss and its impact on ocean-atmosphere energy exchange and ice production, *J. Geophys. Res.,* 116, C04015, doi:10.1029/2010JC006235.

Boisvert, L. N., T. Markus, C. L. Parkinson, and T. Vihma (2012), Moisture fluxes derived from EOS Aqua satellite data for the North Water polynya over 2003-2009, *J. Geophys. Res.,* 117, D06119, doi:10.1029/2011JD016949.

Boisvert, L. N., T. Markus, and T. Vihma (2013), Moisture flux changes and trends for the entire Arctic in 2003-2011 derived from EOS Aqua data, *J. Geophys. Res.,* accepted.